

Rotational remanent magnetisation as a magnetic mineral diagnostic tool at low rotation rates

Mark W Hounslow^{1,2}, Chorong-Shern Horng³ & Vassil Karloukovski¹

¹. Lancaster Environment Centre, Lancaster University, Lancaster, UK.

(mark.w.hounslow@gmail.com, correspondence author), (v.karloukovski@lancaster.ac.uk)

². Earth, Ocean and Ecological Sciences, Univ. of Liverpool, Jane Herdman Building, Liverpool, UK.

³. Institute of Earth Sciences, Academia Sinica, PO Box 1-55, Nankang, Taipei 11529, Taiwan.
(cshorng@earth.sinica.edu.tw)

Summary

Prior work on rotational remanent magnetisation (RRM) and rotational anhysteretic remanent magnetisation (ARM_{ROT}) has demonstrated promise for magnetic mineral identification in earth materials. One challenge has been to calibrate the measurements to magnetic mineral types and microstructural controls, since previous studies have used differing spin rates, alternating field (AF) intensities and decay times, which hinders a comparison of datasets. Using a RAPID magnetometer we show that the range of usable practical rotation rates is 0.25 to 3 Hz [rps] which allows a wide range of RRM and ARM_{ROT} characteristics to be utilised (at 100 mT AF field, 100 μ T bias field). Sets of magnetic mineral extracts from sediments, and well characterised rock samples that contain the key magnetic minerals magnetite, pyrrhotite and greigite are used for a calibration of the RRM- ARM_{ROT} behaviour. Detrital pyrrhotite and pyrrhotite-bearing phyllites have largely small positive effective field (B_g) values, with differences in B_g and ARM_{ROT} ratios at 0.5 and 2.5 Hz [rps] allowing grain-size discrimination. The positive B_g values, and changes in RRM and ARM_{ROT} with rotation rates allow distinction of pyrrhotite from magnetite and diagenetic greigite. Diagenetic greigite has B_g values of -83 to -109 μ T (at 0.5 Hz [rps]) and unusual RRM variation at low rotation rates caused by anisotropy affects. In contrast to previous work, based on crushed and sized natural magnetite at high spin rates, B_g for single domain magnetite from intact bacterial magnetofossils from Upper Cretaceous Chalk has some of the lowest B_g (0 -1 μ T) and displays a steep decline in ARM_{ROT} with increasing rotation rates. A simple tool for particle size characterisation of magnetite may be the ratio of ARM_{ROT} at spin rates 2.5 and 0.5 Hz [rps]. Stability of RRM is better studied using RRM acquisition with increasing AF field intensity, since static demagnetisation imparts a nuisance gyroremanence along the field axis. Mineral microstructure, dislocations and particle interactions are likely additional effects on RRM behaviour that need more investigation.

Keywords: Magnetic properties, Environmental magnetism, Marine magnetism and palaeomagnetism, Rock and mineral magnetism, Biogenic magnetic minerals, Magnetic mineralogy and petrology

1. Introduction

Rotational remanent magnetisation (RRM) is related to the mechanisms of gyroremanent magnetisation (GRM) acquisition when samples are rotated in a decreasing intensity alternating magnetic field. (Wilson & Lomax 1972; Stephenson 1980; Potter & Stephenson 1986; Madsen 2003). The RRM produced is either parallel or antiparallel to the rotation vector, and for magnetite may be preferentially acquired by single domain (SD) particles (Potter & Stephenson 1986). The fact that RRM is preferentially acquired in SD particles, or those with high magnetic stability makes it particularly attractive for investigating palaeomagnetic signal carriers, jointly with anhysteretic remanent magnetisation (ARM) properties.

It has been shown that for crushed magnetite, the intensity of RRM acquisition may also be related to particle size (Potter & Stephenson 1986), and for diagenetic greigite the magnitude of RRM is considerably enhanced compared to magnetite (Snowball 1997b; Stephenson & Snowball 2001). This difference provides a simple, diagnostic tool for identification of diagenetic greigite, but not necessarily bacterial magnetofossil-greigite (Snowball 1997a, 1997b; Reinholdsson et al. 2013; Chen 2014). RRM has not been detected in haematite (Wilson & Lomax 1972; Potter & Stephenson 1986) but appears to be acquired by pyrrhotite (Thomson 1990). Despite the apparent utility of RRM for mineral magnetic identification, it has been little used, which may be due to four reasons: 1) the lack of widespread 'off the shelf' equipment for RRM application, 2) the often-weak RRM generated in many earth materials, 3) in many prior studies high spin rates generating the RRM were not conducive to routine study of wet or poorly consolidated sediment sample, and 4) limited understanding of the various kinds of intrinsic and external controls on RRM and GRM production (Madsen 2003, 2004), especially at low rotation rates.

This work firstly addresses some of the practical issues with generating, measuring, and interpreting RRM at low rotation rates. We use measurements from the 2G Enterprises RAPID magnetometer (Kirschvink et al. 2008, hereafter called the RAPID), which has the ability for controllable sample rotation at low rotation rates, allowing routine automated RRM measurement on conventional samples. More than 20 RAPID magnetometers are currently installed worldwide, and therefore this could allow more widespread application of RRM behaviours for mineral magnetic identification. The RRM in many sediments is also weak, and the high sensitivity of SQUID magnetometers allow RRM to be measured in most samples. Prior commercial instrumentation (Stephenson & Molyneux, 1987) tackled the weak RRM intensity issue by rotation at large frequencies (i.e. ~ 100 Hz), which increases the RRM intensity, but is not conducive to studying wet, fragile or imperfectly-shaped samples.

Secondly, we explore the utility of routine mineral magnetic identification, by using RRM behaviours on natural samples of known magnetic composition. These measurements allow us to suggest possible ways to effectively identify magnetic mineralogy in samples of unknown composition.

2. Quantification of rotational remanent magnetisation

RRM magnetisations are acquired with an alternating magnetic field (AF) is applied normal to the rotation axis of a specimen (Fig. 1), since RRM's are a special type of the GRM acquisition process (Madsen 2004). To standardize the quantification of RRM, Stephenson (1980) and Potter and Stephenson (1986) suggested the following:

1) An RRM magnetisation that is produced parallel to the rotation vector is signed as positive, and when opposite to the rotation vector, is signed as a negative RRM. We follow this convention (Fig. 1). Some studies have followed the opposite convention (Wilson & Lomax 1972; Stephenson 1976; Noel 1988; Edwards 1982b) and when discussing these studies, we use a conversion to the convention of Stephenson (1980).

2) The magnitude of the RRM is related to the abundance of magnetic phases, and usefully Potter & Stephenson (1986) introduced the B_g parameter which normalises the RRM by the ARM acquired under the same AF field and rotation conditions as the RRM. This kind of ARM is here symbolised as ARM_{ROT} (Fig. 1). The DC bias field used to generate the ARM_{ROT} is parallel to the rotation axis, but the AF field generating the ARM is aligned 90° to the rotation axis and DC field axis (Fig. 1). More widely used conventional methods of generation of ARM use co-axial AF and DC field axes to produce ARM (here referred as ARM_z). For a few samples we also investigated the ARM acquired at zero rotation rate as a proxy for ARM_{ROT} (See SI section 3.1) as used in some prior studies (Snowball, 1997b).

Rotation rates are here expressed in revolutions per second (SI unit Hz) widely indicated as 'rps' in much prior work, and here symbolised as ω in Hz [rps] units.

B_g , the effective gyromagnetic field in micro-Tesla (Potter and Stephenson, 1986) is defined as:

$$B_g = B_a \times \text{RRM} / \text{ARM}_{\text{ROT}} \quad \text{Eq.1}$$

where B_a = DC field used in generating the ARM (usually around 50- 150 μT)

2.1 Key attributes of RRM

1) The magnitude of RRM is partly dependent on the rotation rate. When the rotation rate exceeds the frequency (in Hz) of the AF field (i.e., the *AF threshold*) most magnetic materials have a greatly enhanced RRM intensity. This issue has led in a strong focus on RRM studies at large rotation rates (Table 1). We refer to low spin rates, as below the AF-field threshold and high spin rates above this—hence the separation of existing RRM datasets into Tables 2 and 3.

2) Magnetite, maghemite and greigite have positive RRM above the AF threshold, and largely negative (but not entirely negative), and much reduced RRM below this threshold. Conversion of B_g values between high spin to low spin values is open to much uncertainty— Snowball (1997b) used a conversion factor of -0.08 for transforming a magnetite B_g from 108 to 5 Hz [rps]. The synthetic Mapico black magnetite (Potter & Stephenson, 1986; Edwards & Desta, 1989) has been used in both low and high spin studies suggesting an alternative conversion factor of ca. -0.027 between 108 Hz [rps] and 0.07 Hz [rps]. For diagenetic greigite a conversion factor for B_g of -0.14 ± 0.06 for rotation rates between 95 Hz [rps] to 2.5 Hz [rps] is possible with values in Tables 2, 3.

3) Multidomain (MD) magnetite and haematite have no or little appreciable RRM (Wilson & Lomax 1972; Potter & Stephenson 1986; Snowball 1997b). This is exemplified by basalt sample D264-2a (Tables 1, 3) studied by Edwards (1982a, b) and Edwards & Desta (1989). This behaviour of MD magnetite is a useful property of RRM, since it implies that SD grains can be studied in mixed SD-MD earth materials that would acquire appreciable MD-related magnetisations using other magnetic investigation methods.

4) B_g for maghemite ($\gamma\text{Fe}_2\text{O}_3$) may be in part concentration dependent, with larger B_g values in samples with larger concentrations of $\gamma\text{Fe}_2\text{O}_3$ (Madsen 2003). Synthetic $\gamma\text{Fe}_2\text{O}_3$ has some of the largest $|B_g|$ values for Fe-oxides at both low and high spin rates, but natural $\gamma\text{Fe}_2\text{O}_3$ has so far not been studied (Tables 2, 3).

5) CrO_2 recording tape particles have negative RRM above the AF threshold, and a largely positive RRM below the threshold (Madsen 2003), both in the opposite sense to that of magnetite (Table 2). Although Snowball (1997b) measured negative RRM at 5 Hz [rps] (Table 3), and Madsen (2003) negative RRM at 25 Hz [rps].

6) Heated pyrrhotite (either monoclinic or hexagonal) appears to display positive RRM both below and above the AF threshold (Tables 2,3), with rapid changes of RRM intensity close to the AF threshold. Unheated pyrrhotite studied by Thomson (1990) displayed negative RRM at 3 Hz [rps].

7) At AF frequencies below the AF threshold, the frequency of the field used may have little impact on the changes of RRM with rotation rate, or at least at rotation rates up to 0.1 Hz [rps] investigated by Edwards (1980a). However, the impact of differences in AF frequency at rotation rates further towards the AF threshold has not been investigated experimentally. However, some theory suggests the ratio of the rotation rate and AF frequency should in part control the strength of RRM acquisition (Stephenson, 1980, 1985)

8) At low rotation rates the time of decay of the AF field (T_D in seconds; Fig. 1) has a large impact on the changes of RRM with ω (Edwards 1982b), such that changes in RRM properties are best compared when expressed with respect to ωT_D (in revolutions) rather than using ω .

9) RRM acquisition is not an instantaneous process, some ca. 90° (or larger) of sample rotation at peak AF field is required for RRM to be fully acquired (Edwards, 1982b, Roperch & Taylor 1986). In much demagnetisation equipment this is impacted by the AF peak field hold time (T_H), which ideally should be long enough for this rotation 'initialisation' to be achieved.

10) An RRM induced by a particular AF field may require a larger static demagnetising AF field to fully demagnetise the induced RRM (Edwards, 1980b). This effect is likely related to the angular dependency of the switching field (Madsen, 2004). Like demagnetising ARM or IRM (Stephenson, 1983) the intensity-decay curve produced during demagnetisation may differ between static or tumbling demagnetisation methods.

Whilst some is understood about the general RRM behaviour of common magnetic material in earth materials, the range of rotation rates, AF and DC fields used in previous studies (Tables 2 and 3) and the hold and decay rates of the AF inducing field, hinders a general and detailed comparison of the mineral magnetic behaviours.

This work focusses on five aspects of RRM behaviour at rotation rates ≤ 3 Hz [rps]: 1) the variation of RRM, ARM_{ROT} and B_g with rotation rate, 2) the magnitude and sign of B_g and RRM, and 3) the stability of the RRM as measured by the median destructive field (MDF)– since MDF of the RRM has been shown to be a useful additional parameter in characterising particle size and mineralogy (Potter & Stephenson, 1986; Snowball, 1997b); 4) the impact of differences in peak AF hold times (T_H); 5) exploration of how RRM datasets could be used for magnetic mineral identification at $\omega T_D \leq 4.5$ revolutions.

3. Mineralogy of test samples

The sample sets used here comprise two types, magnetic concentrates (extracts) and natural rock samples of known magnetic mineralogy. These sample sets comprise:

1) Detrital monoclinic pyrrhotite from river sediment, collected in the upper reaches of the mountainous Zhoushui River (at 23.786836 N, 121.01097 E, Taiwan), which is sourced from the pyrrhotite-bearing metamorphic terranes in the Central Range (Horng and Huh, 2012). Pyrrhotite grains in sediments were extracted using a rare earth magnet and were purified magnetically several times. The purified sample was then subdivided into five micro-sized fractions (<5, 5-10, 10-20, 20-38 and 38-63 μm , samples PY1 to PY 5 respectively; Table 4; Fig. 2a) with sieves and membrane filters. XRD analyses determined their purities (Fig. S1). The larger detrital particle sizes show some minor evidence of oxidation to lepidocrocite and goethite (see supplementary information (SI) Fig. S1).

2) Magnetic extracts using the method of Hounslow & Maher (1996, 1999). The magnetic extracts broadly represent two groups, those from sediments with intact or near-intact magnetic oxide assemblage (e.g., like Franke et al. 2007), and a set with *residual* discrete Fe-oxide components (and Fe-oxides in silicates) after early sulphidic diagenesis or deep-burial diagenesis (e.g., Hounslow et al. 1995; Hounslow, 1996; Maher & Hallam, 2005; Table 4). The extracts are from: a) the late Triassic Lunde Formation (LU codes) from the North Sea, containing a residual suite of silt-sized magnetic minerals after extensive diagenetic dissolution, with in some cases minor discrete magnetic oxides, but abundant Fe-oxide inclusions in associated silicates (Hounslow et al. 1995). B) Quaternary and

Pliocene sediments from the Owen Ridge (OR sample codes) and Madingley Rise (codes MR; on the Mascarene Plateau) both in the Indian Ocean. The Indian Ocean samples have detrital sources exclusively of well mixed, far travelled aeolian origin (Table 4). Some of these extracts also represent residual magnetic assemblages (Table 4). Extract samples with codes LU, OR and MR1 to MR3 are generally poor in fine-grained magnetic particles and represent the magnetic detrital fraction mostly $>2 \mu\text{m}$ in size (i.e., the E_{MP} extract type of Hounslow & Maher, 1999). Samples MR4 to MR6 are E_{MPT} type extracts of Hounslow & Maher (1999) and contain largely detrital grains $<2 \mu\text{m}$ in size and in some cases contain accessory magnetite magnetofossils (i.e. MR4 and MR5). The E_{MPT} extracts may contain the bulk of the discrete-grain SD-sized particles. This is not to say that the E_{MP} extracts contain no SD-like magnetic grains, since these may be within the larger detrital grains. The E_{MP} extracts contain variable amounts of Fe-oxides as inclusions in silicates, reflected in the variable content of silicates in the extracts (see SI for details). Therefore, these extracts are representative of the key magnetic components often found in sediments of various ages, and those residual magnetic minerals elevated in relative abundance during diagenetic-related Fe-oxide dissolution (Roberts, 2015).

3) Monoclinic pyrrhotite bearing phyllites (samples PY6 to PY9) from Taiwan (Fig. 2B) with relatively coarse grain size. Hysteresis data indicate B_{cr}/B_c of 1.10 to 1.12 and M_{rs}/M_s of 0.66 to 0.72 for these samples (SI Table S1). These are typical values for metamorphic pyrrhotite and are not necessarily indicative of SD properties (Horng 2018).

4) Greigite samples from Plio-Pleistocene greigite-containing mudstones from the Lower Gutingeng Formation, SW Taiwan (Horng et al. 1998; Jiang et al. 2001; sample codes GR1 to GR4; Table 4). Hysteresis data indicate B_{cr}/B_c of 1.26 to 1.39 and M_{rs}/M_s of 0.54 to 0.63 for these samples (SI Table S1). Chen (2014) also measured the RRM in two samples from this location at high-spin rates (Table 2). The diagenetic greigite in these samples is very fine-grained and widely dispersed through the phyllosilicate matrix (Fig. 2C).

5) Whole rock samples of the Upper Cretaceous Chalk (CC code samples), from southern England. These are from the stratigraphic level of sample CW9b originally figured by Montgomery et al. (1998) which contains abundant chains of prismatic magnetofossils (Fig. 2D) in extracts. These are also figured in Hounslow & Maher (1999) and Kopp & Kirschvink (2008) (Table 4). The magnetofossil chains in the extracts seem to reflect in-situ preservation, since other extracts from the Chalk from elsewhere (unpublished data of Hounslow) do not show such high abundance of intact chains (Fig. 2D). These samples also contain an associated assemblage of Fe-oxides as inclusions in detrital quartz and feldspars but have very little detrital Fe-oxides outside silicate hosts (see SI for details).

6) Relatively unaltered fine-grained dolerites (SVD code) with a content of typical titanomagnetite, which has undergone high temperature alteration to ilmenite-magnetite intergrowths (Table 4), with margins altered to maghemite. Clots of magnetite and acicular rods of Fe-oxide occur in the groundmass (Gayer et al. 1966; Krumsiek et al. 1968; Halvorsen 1973). Some of the prior work using low rotation rate RRM was performed on similar basaltic rocks (Tables 1, 3).

7) Samples of siltstones and sandstone from the De Geerdalen Formation from several locations in Svalbard (Table 4), which have a rather similar detrital magnetite magnetic mineralogy throughout (Hounslow et al. 2007; 2022). The succession has been subjected to complex diagenetic changes (Mørk 2013; Haile et al. 2018), which will have removed much of the original discrete Fe-oxides.

Synthetic samples have been much used in previous RRM studies (Edwards 1980a; 1980b, Potter and Stephenson 1986; Snowball 1997b; Madsen 2003), but the intention here was to focus on naturally

derived materials, since synthetic samples can have unusual morphologies, microstructure and purity not seen in natural minerals.

To prepare samples of the magnetic extracts and detrital pyrrhotite to measure they were dispersed in a 5 ml droplet of PVA glue on an acetate sheet, which was allowed to dry at room temperature overnight. When dry this was peeled off, folded into a ball, and placed in a plastic pot (with cling-film padding) as the sample to measure. There was some inevitable clumping of magnetic particles during the drying process, an inevitable consequence of using granular magnetic materials, which will have resulted in some magnetic interaction (clumping observed in most) and anisotropy affects (Cisowski 1981). The pyrrhotite bearing phyllites were gently crushed and mounted in a plastic pot. Other samples were core-plugs or cubes with no encapsulation.

4. Experimental procedures and issues

Measurements used the Lancaster University RAPID magnetometer. This RAPID is housed in a large Helmholtz cage for field cancellation, which together with the Mu-metal shields cancels the earth's magnetic field to around 0.03-0.08 μT at the demagnetiser coil position. AF frequencies are 327 Hz on the transverse-axis coil (Fig. 1), and 360 Hz on the Z-axis coil. The Lancaster RAPID has a standard duration of peak AF field of 30 AF cycles giving hold times (T_H) of 92 ms and 83 ms for transverse and Z-axis coils respectively. T_H can be changed but is kept low to limit coil overheating. The ramp-up and ramp-down times are fixed at ca. 0.64 s and 1.53 s (i.e., T_D) respectively, irrespective of maximum field used (See SI section 4 for further details).

The RAPID vacuum system that holds samples onto the silica glass rod for insertion into the measurement space, is unable to routinely hold-onto rock samples at $\omega > 3$ Hz [rps], unless special precautions are taken to fix the sample onto the quartz-glass rod. This essentially limits the routine practical RRM measurements of usual-sized rock samples to rotation rates of ≤ 3 Hz [rps]. The software set 'rotation rate' is half that actually achieved (i.e., set values of 1, 2, 6 correspond to 0.5, 1 and 3 Hz [rps] respectively). This was calibrated at rotation rates 0.1, 0.15, 0.2 Hz [rps], which yielded a linear relationship with time, and extrapolated to rates up to 3 Hz [rps].

All weak magnetisation measurements were performed with a 'measurement blank' appropriate for each sample set (i.e., a blank subjected to all the same steps). This bypassed the 'standard holder-correction procedure' on the RAPID, which does not account for magnetisation and demagnetisation of holders and sample pots during measurements. The GM4Edit software does the blank-type corrections to the data (Hounslow 2019).

All samples were set into an initial standard state by AF demagnetisation, sequentially along magnetometer X, Y axes at 110 mT, followed by demagnetisation only along the Z-axis at 150 mT. A larger field along Z-axis was applied to reduce possible GRM's along the Z-axis from the X and Y AF applications, which can persist into higher coercivity fields than the applied field (Edwards 1982b, Madsen 2003). All RRM and ARM_{ROT} measurements were performed with a 100 mT peak AF field. Here the sign of ω indicates the sense of spin coded into the RAPID software. A $-\omega$ rotation rate has the rotation vector directed **down** (to +Z), and $+\omega$ rate the rotation vector directed **up** (to -Z; Fig. 1). The sign of ω therefore also indicates the down or up-sense of the rotation vector. Hence, positive RRM will be a larger magnetisation along the Z-axis with a $-\omega$ rotation rate (vice versa for a negative RRM; Fig. 1). It is implicitly assumed that at 1 Hz [rps] one rotation corresponds to 327 cycles of the transverse AF field.

RRM generation follows the procedure of Wilson & Lomax (1972) in which the sample was sequentially spun in opposite senses (first about the Z-axis with $-\omega$). The RRM is $\frac{1}{2}$ the difference

between the magnetisation measurements at $+\omega$ and $-\omega$ (Fig. 1). The sample spins throughout the AF ramp-up, hold and ramp-down interval. Other AF fields use the same hold and ramp-down times, but the AF ramp-down-rate (i.e. mT/sec) is adjusted to fit these times (inset in Fig. 1). For weak RRM's it is often advantageous to perform repeats, since the noise inherent in determining the RRM can be larger than the magnetisation measurement standard deviation (SD) along the Z-axis (See SI for noise details). This problem is amplified if there is residual undemagnetised remanence (e.g., from >150 mT coercivity remanence) along the Z-axis, since the SD of magnetisation measurements along any axis is strongly related to the moment along that axis (See SI Fig. S10). In a practical sense this dictates: 1) the lower limit of useful RRM measurement for those samples with a significant intrinsic remanence which cannot be AF demagnetised. That is, the presence of significant haematite or goethite- magnetisations limits the applicability of using RRM (as does very low abundances of magnetic minerals). 2) The RRM and ARM_{ROT} measurements should be performed prior to any other large field magnetisations.

The ARM_{ROT} is determined with a DC bias field of $100 \mu\text{T}$ along the Z-axis (AF of 100 mT along the Y-axis; Fig. 1), and by spins in opposite senses (spun about Z-axis with $-\omega$ first; Fig. 1). The ARM_{rot} is the average of the two magnetisation measurements. Theoretically, the difference between these two should also yield the RRM (Stephenson & Molyneux 1987, here symbolised as RRM_{100}), although in practice the additional large ARM_{rot} makes the determination of RRM_{100} noisier than without the DC field (See SI section 3.2). In addition, we used the same field settings and measured the ARM acquired at zero rotation rate (ARM_{trans}). This could be used as a proxy for ARM_{ROT} , if equipment was not available to rotate samples during ARM acquisition (this is examined in SI section 3.1). Rotational ARM can also be produced by rotating samples in orthogonal weak and strong and declining DC fields as an alternative (Stephenson, 1988). A conventional ARM was also determined along the Z-axis by applying a 100 mT AF and $100 \mu\text{T}$ DC coaxial along the Z-axis (called here ARM_z) allowing comparison to other standard ARM datasets. Measuring both ARM_{ROT} and ARM_z provides additional mineral-diagnostic values. Care was taken in determining the zero-level for all ARM measurements by measuring residual magnetisation after AF demagnetisation at 150 mT (along Z, ramp down time of 1.39 sec) before and after the ARM determinations (see SI for details).

For the magnetic extracts a blank comprising a dry PVA droplet + pot + quartz-silica rod has a mean RRM of $\sim -0.10 \pm 0.2 \times 10^{-10} \text{ Am}^2$ (at 0.5 Hz [rps]), ARM_{rot} of $\sim 1.7 \pm 0.5 \times 10^{-10} \text{ Am}^2$ (at 0.5 Hz [rps]), and 150 mT demagnetised Z-axis moment of $\sim 0.4 \pm 0.3 \times 10^{-10} \text{ Am}^2$ (uncertainties are 1σ). The RAPID quartz-silica rod used has a mean Z-moment of $\sim 0.15 \pm 0.4 \times 10^{-10} \text{ Am}^2$ (1σ , after 150 mT demagnetisation). The average uncertainty (1σ) of a single magnetisation measurement (average of four in total on the Z-axis) for the quartz-silica rod is $\sim 0.01 \times 10^{-10} \text{ Am}^2$.

The median destructive field (MDF) of the RRM was determined in two ways: 1) after RRM acquisition from the $+\omega$ rotation state (followed by static AF demagnetisation along the Z-axis in 10 mT increments, up to 90 mT, followed by one at 150 mT), and 2) for both $+\omega$ and then $-\omega$ rotation states (both with static AF demagnetisation on Z-axis, in 10 mT increments to 150 mT).

In method-1 the zero-'base line' of the RRM decay was judged using the flat-tail of the RRM decay curve and the 150 mT step. In method-2, by subtracting the $+\omega$ and $-\omega$ RRM demagnetisation curves, and estimating the zero-'base line'tail of the resulting RRM decay (see SI for details). In each case a linear regression trend using a few data points either side of the MDF was fit to the normalised moment to field intensity changes, from which the median point was estimated in Excel. The MDF of the ARM_z was similarly determined but using the two points straddling the median point. An alternative simpler proxy for the ARM stability is the proportion of ARM remaining after 40 mT

demagnetisation (Peters & Thompson, 1989), which is here symbolised at $d.ARM_{Z_{40mT}}$. Comparison of MDF and $d.ARM_{Z_{40mT}}$ between different methods of demagnetisation can be problematic, since MDF's produced by static, single axis methods can be some 1.3-1.5 times those produced by tumbling demagnetisation (Stephenson, 1983). For example, the seminal work of Dunlop (1983) on basalts seems to have used single axis demagnetisation (West & Dunlop, 1971) and that of Potter and Stephenson (1986) used tumbling. The RAPID protocol `rmg-template` files which run these procedures are in the Supplementary information.

5. Results

Since RRM and ARM_{ROT} vary greatly in magnitude the RRM and ARM_{ROT} are normalised by the absolute value at 0.5 Hz [rps]. This allows an inter-sample comparison of changes with rotation rates, removing the effect of differences in magnetic mineral abundance. The reasons for using this somewhat arbitrary value for normalisation are outlined in section 5.3.

5.1 Changes of RRM, ARM_{rot} and B_g with rotation rate for magnetite.

Like Edwards' (1982b) we find the RRM has predominantly negative values throughout the rotation rate range (Figs. 3a, 4a, 5a). This is except for sample SVD2 at $\omega > 1.3$ Hz [rps] which has a positive RRM (Fig. 4a). The 3 Hz [rps] step for CC2 (Fig. 4a) is probably subject to a small flux jump on the RAPID, hence its erroneously large, normalised value. One of Edwards' (1982b) samples F37B-1a shows a similar behaviour to SVD2, although a sister specimen measured by Wilson & Lomax (1972)-F37B-2 did not. Most of the samples display a minimum in RRM between 0.3-0.4 Hz [rps]. Minimums have typically also been found in other magnetite bearing rocks at low, but differing rotation rates (Potter & Stephenson 1986; Stephenson & Snowball 2001). This general pattern is consistent except for sample MR2 (rather noisier data), which has a rather flatter RRM- ω curve (Fig. 3a), like specimens E23a-1 and L-S1-2 of Wilson & Lomax (1972).

The normalised ARM_{rot} have mostly rather flattish curves with a small decline in ARM_{rot} at $\omega > 0.3$ Hz [rps] for the magnetic extracts and the dolerite samples (Fig. 3b, 4b). Contrastingly rather steeply declining ARM_{rot} for larger ω occur for the Chalk and De Geerdalen sandstone/siltstone samples (Figs. 4b, 5b). Significantly, ARM_{rot} changes with ω have not been investigated much previously, although changes observed have been inferred as an interaction between the RRM and the ARM_{rot} (Stephenson & Snowball 2001). The transverse ARM produced without rotation (ARM_{TRAN}) is most often slightly lower than that produced at $\omega = 0.05$ Hz [rps] (Figs. 3b, 4b, 5b).

Normalised B_g values largely mirror the changes in normalised RRM for many samples especially those with a negative peak in B_g less than $-3 \mu T$ (Figs. 3c, 4c, 5c). The two Chalk samples (CC1, CC2) show the flattest curves and lowest B_g values between 0 and $-1 \mu T$ throughout the rotation rate range (Fig. 4c). The changes in B_g with ω are rather noisy due to weak RRM's for MR2 and OR3 (Fig. 3c) and are perhaps closer to B_g behaviours shown by SVD1, DF2, DF5, DF6 which have stronger RRM's (Figs. 4c, 5c).

The lower B_g values for the magnetite magnetofossils in the Chalk samples compared to the silt-sized magnetic extracts are opposite to the negative relationship with magnetic grain size noted by Potter & Stephenson (1986) for crushed and sized-magnetite. Chen (2014) also noted the ca.10 to 100 times smaller B_g values for several sets of magnetite magnetosome samples compared to the samples measured by others at high spin rates (Table 2). The measurements here therefore concur with those of Chen (2014), although ability to directly compare B_g values between low and high spin datasets is hindered. The sample Pajep8 of Snowball (1997b) containing magnetite magnetofossils

and MD magnetite with a B_g of $-0.14 \mu\text{T}$ at 5 Hz [rps] (Table 3) is also consistent with these observations.

The B_g values and changes with ω for samples from the De Geerdalen Formation are rather like the magnetic extracts (Fig. 3c, 5c), a feature which might be expected considering initial sulphidic diagenesis typically removes much of the finer grained discrete magnetite content in sediments (Roberts 2015). Compared to the other samples, dolerite SVD1 has a much larger B_g value ($-26 \mu\text{T}$ at 0.5 Hz [rps]). Edwards & Desta (1989) have measured similar values in synthetic $\gamma\text{Fe}_2\text{O}_3$ ($-30 \mu\text{T}$, $-37 \mu\text{T}$; Table 3) and Roperch & Taylor (1986) in a Miocene basalt sample ($-25 \mu\text{T}$) at low ω .

5.2 Changes of RRM, ARM_{ROT} and B_g with rotation rate for pyrrhotite and greigite.

Greigite produces normalised RRM changes with ω like that of magnetite, but with a minimum (negative) RRM at 0.5 Hz [rps], and some larger fluctuations at lower ω values (Fig. 6a). Pyrrhotite samples do not display RRM behaviour like magnetite and greigite, having positive RRM for part or all the range of ω investigated (Figs. 7a, 8a). Generally, all the pyrrhotite samples had RRM which was challenging to measure (i.e., producing noisy data), since they contained a strong residual remanence remaining after 150 mT demagnetisation, so much of the sample data is from averaging of duplicate measurements. The detrital pyrrhotite $>20 \mu\text{m}$ in size (PY4, PY5) produces a peak in positive RRM at 0.3-0.4 Hz [rps], and then declines towards near zero or negative RRM by 3 Hz [rps] (Fig. 7a). Detrital pyrrhotite $<20 \mu\text{m}$ (PY1-PY3) produces a trend towards increasingly more positive RRM through 0.5 -2.5 Hz [rps]. The $< 2 \mu\text{m}$ detrital pyrrhotite has the largest positive normalised RRM at $\omega >1$ Hz [rps] and has some possible step-like behaviour in RRM at $\omega <0.4$ Hz [rps], like greigite (Figs. 6a, 7a)- although this may be measurement noise in this quite weak sample. The pyrrhotite-bearing phyllite samples (PY6 to PY9) show RRM behaviour with ω rather like the coarser detrital pyrrhotite (Fig. 8a) suggesting these largely contain pyrrhotite $> 20 \mu\text{m}$ in size. Such large particle sizes are also seen in electron microscopy (Fig. 2B). A positive RRM was detected by Thomson (1990) in samples heated to 228-315°C but generally much smaller negative RRM's in unheated or those heated to below 228°C (at 3 Hz [rps]). Thomson (1990) attributed these temperature-related changes to creation of hexagonal pyrrhotite during the heating. The RRM produced by Thomson (1990) was weakly if at all dependent on rotation rates at $\omega <10$ Hz [rps].

Changes in ARM_{ROT} with ω for the sulphides are rather similar and flattish at > 0.4 Hz [rps] with all showing a progressive increase in normalised ARM_{ROT} at $\omega > 0.5$ Hz [rps] (Figs. 6B, & 7B, 8B), and like magnetite have ARM_{TRAN} values rather similar or lower than the value at 0.05 Hz [rps].

Changes in B_g largely reflect the changes in normalised RRM, since any changes in ARM_{ROT} are rather suppressed compared to RRM changes with ω (Fig. 7C). The pyrrhotite samples show mostly positive B_g at $\omega \geq 0.5$ Hz [rps]. Slotznick et al. (2016) has apparently detected a range of both positive and negative B_g values in pyrrhotite bearing rocks (at $\omega \geq 1$ Hz [rps]), although the methodology used is unclear, since their ' B_{eff} values' seem to exist for both $-\omega$ and $+\omega$.

5.3 Impact of changing AF field hold times on RRM and ARM_{ROT}

Edwards (1982b) demonstrated that for magnetite the AF field ramp down time (T_D , in seconds) controlled the position of the peak of the negative RRM in magnetite-bearing samples, such that ωT_D (in revolutions) was a more fundamental expression of the RRM changes than the rotation rate. For the magnetite-bearing samples of Edwards (1982b) the peak in negative RRM was at 0.40 ± 0.02 rev. The apparent peak in our magnetite-bearing samples is at $\omega T_D = 0.4$ to 0.75 rev (Figs. 3,4,5), generally somewhat larger than Edwards observed. However, our RRM initialisation is different to that used by Edwards, since our hold time, T_H (92 ms) is insufficient to produce the 90° of rotation

initialisation used by Edwards. For three samples we measured RRM and ARM_{ROT} with rotation rate for T_H at 0.917 s and 9.17 s (300 and 3000 cycles setting on RAPID; Fig. 9). A T_H of 0.917 s produces the required 90° (or larger) of initialisation rotation at $\omega \geq 0.27$ Hz [rps], ($\omega T_D = 0.42$ revolutions or larger using $T_D = 1.53$ s) and the later exceeds the 90° threshold at all rotation rates used (Fig. 9A,C,E). Both these larger T_H produce a peak in RRM close to $\omega T_D = 0.4$ rev for pyrrhotite and greigite (Fig. 9C,E), as does dolerite sample SVD2 (SI Fig. S19D), but the magnetite sample MR1 has its RRM peak at 0.6 rev (0.4 Hz [rps]; Fig. 9A). These data broadly concur with Edwards (1982a) experimental data but do suggest that perhaps there may be additional mineralogical control on the precise position of the RRM peak in ωT_D units.

Broadly the RRM using $T_H = 92$ ms are a little smaller than that acquired over longer hold times at rotation rates 0.5 to 3 Hz [rps], and diverge more at rates < 0.5 Hz [rps] (Fig. 9,A,C, E). For the magnetite (MR1) and pyrrhotite (PY5) samples at $\omega = 0.3$ -3 Hz [rps], the RRM at 92 ms hold time is some $96 \pm 1.6\%$ and $105 \pm 13\%$ (1σ values) of that for the average of RRM at the longer hold times. Greigite (sample GR1) in contrast, has RRM some $88 \pm 3\%$ of the RRM for $T_H = 9.17$ s, over the 0.5- 3 Hz [rps] range (Fig. 9E), but substantial deviations at rates < 0.5 Hz [rps] (Fig. 9E). The greigite RRM is more consistent between the 0.917 s and 9.17 s hold times at $\omega \geq 0.3$ Hz [rps] above the 90° initialisation threshold (Fig. 9E).

For magnetite (MR1) and pyrrhotite (PY5) the ARM_{ROT} (for $T_H = 92$ ms), is on average marginally larger than both the longer hold times (Fig. 9B,D), with the average percentage comparison being $102 \pm 1.4\%$, $104 \pm 1.2\%$ for $T_H = 0.917$ s, and $102 \pm 1.4\%$, $102 \pm 1.1\%$ for $T_H = 9.17$ s respectively (for $\omega = 0.1$ to 3 Hz [rps]). In contrast, greigite displays lower ARM_{ROT} at $T_H = 92$ ms with the average comparison being $93 \pm 2.0\%$ and $89 \pm 2.9\%$ for the 0.917 s and 9.17 hold times (at $\omega \geq 0.5$ Hz [rps]). The greigite (GR1) behaviour at $\omega < 0.5$ Hz [rps] is quite different to the other samples and indicates a complexity in ARM_{ROT} acquisition not seen in other test samples. The impact of T_H differences on Bg are like those percentage comparisons seen in RRM for magnetite (MR1) and pyrrhotite (see SI Fig. S19). For greigite sample GR1, the peak in Bg is also larger at ~ 102 μ T and displaced to ~ 0.2 to 0.3 Hz [rps], compared to that in Fig. 6c.

The complexity in the RRM and ARM_{ROT} behaviour at $\omega < 0.5$ Hz [rps] (also having the AF hold time (T_H) shorter than the optimum for RRM initialisation), led us to choose a blanket normalisation for parameters at 0.5 Hz [rps], like is displayed in Figs. 3 to 8. Values at this rotation rate and higher generally show more consistent changes. Had we used a T_H of ~ 0.92 s a more optimum value to normalise the RRM, ARM_{ROT} and Bg values would have been that close to the peak in RRM at $\omega T_D \approx 0.4$ revolutions (i.e., about 0.26 Hz [rps]). Hence, the optimum hold time on the 327 Hz RAPID demagnetiser is a T_H of 0.962 s (314 cycles) which would detect the maximum RRM at $\omega T_D \approx 0.4$ rev (0.26 Hz [rps] at $T_D = 1.53$ s). However, this has consequences for potential excess coil heating, and the increased refinement has only minor impact on magnetite and pyrrhotite parameters. However, this is a bigger issue for samples containing diagenetic greigite (i.e., Fig. 9E, F).

We suspect the RRM behaviour at $\omega < 0.5$ Hz [rps] of greigite sample GR1 (at $T_H = 92$ ms) is due to anisotropy and its impact on RRM and ARM_{ROT} acquisition (Potter, 2004) at values below the rotation initialisation threshold. Although we could not investigate the directional dependence of RRM and ARM_{ROT} on GR1, we performed a preliminary study on sample SVD2 which shows similar behaviour to GR1 when rotation was used about the other two axes of this cubic sample, to generate the RRM (See SI section 3.4). For SVD2 this impacts the RRM and ARM_{ROT} and Bg values, demonstrating that anisotropy is an additional source of changes in Bg with ω . However the pattern of changes in Bg,

ARM_{ROT} and RRM are similar with respect to ω , if above the rotation initialisation threshold (SI Fig. S19).

In a practical sense these issues suggest the reliable range of ω for routine use on the RAPID is 0.26 and 3 Hz [rps], if using an AF hold time sufficient to reach rotation initialisation. Samples with significant ferrimagnetic anisotropy will have RRM-data most-impacted if there is inadequate rotation initialisation. However, for many samples with weak anisotropy the AF hold-time may have a limited impact especially at $\omega \geq 0.5$ Hz [rps].

5.4 Demagnetisation of the RRM

Demagnetising of the RRM using method 1, produces an additional ‘nuisance’ magnetisation created in most samples, since the ‘background’ 150 mT demagnetisation on the Z-axis and the mean of the two RRM magnetisation measurements (in opposite rotation directions) were not similar. This is demonstrated well by the greigite sample GR1, measured using method 2, which shows this effect very strongly (Fig. 10a), in which coincident with the RRM demagnetisation, an additional magnetisation (referred to here as GRMz) is generated during demagnetisation along the Z-axis. This seems to be a GRM since in the X-Y plane the GRM begins to increase around the start of the GRMz increase (Fig. 10a, 10d). Overall, the GRMz generated are mostly negative (up-directed) magnetisations (Figs. 10b,10c,10d), although sometimes are positive like the demagnetisation of the 0.5 Hz [rps] RRM for sample GR1 (Fig. 10a). Co-axial demagnetisation axis and GRM’s have been observed previously in greigite (Hu et al. 1989; 2002) and magnetite (Stephenson 1981; Roperch & Taylor 1986), and these are thought to be more generally produced using static demagnetisation, due to the angular dependence (with respect to grain anisotropy) of the switching field (Madsen 2003; Finn & Coe 2020). Normalising GRMz by ARM_{ROT} in the same way as for the RRM (equation 1), produces the effective field B_{gZ} in μT for this remanence (in this case $B_{gZ} = 100 \mu T \times GRMz / ARM_{ROT}$). B_{gZ} values are similar but rather smaller than B_g for RRM induction (Fig. 11a). This is not an ARM from the residual DC field inside the demagnetiser shield, since GRMz is both positive and negative and is variable with respect to ARM_z (Fig. 11b). The DC field inside the shield should produce an ARM of less than $\sim 0.1\%$ of the ARM_z , which is much smaller than the observed GRMz (Fig. 11b). It is also possible that this nuisance remanence may be generated by asymmetry in the AF field, generating an ARM, since small $\sim 0.03\%$ asymmetry could produce an ARM of this order or larger (Hailwood & Molyneux 1974). However, the variable magnitude with the respect to the ARM_z and ARM_{ROT} and the change to opposite direction for some samples, suggests this is less likely than a coaxial GRM.

Therefore, for effective determination of RRM stability (median destructive field, MDF etc) of the RRM the most effective way is to demagnetise both the $+\omega$ and $-\omega$ produced RRM, up to maximum fields well beyond the AF inducing field used for the RRM. This allows separation of any coaxial magnetisation produce along the demagnetisation axis, such as GRM’s or spurious ARM’s produced along that axis. An added advantage is that RRM’s can be quite weak in many earth materials, and the resulting RRM demagnetisation curve has both duplicate data and is double the magnitude of a single demagnetisation curve, resulting in a more robust dataset to work with.

This improved RRM demagnetisation (i.e., method-2) was tested on a few samples, which showed a different range of MDF of RRM compared to the MDF of ARM_z (Fig. 12a). This is expected since these magnetisations activate different grain populations, with the RRM probably activating those

with the higher or the same stability, if the coercivities have a limited range to higher values (Stephenson 1976; Edwards 1984; Potter & Stephenson 1986).

There is a large range in MDF of ARMz from relatively soft MD-type magnetite's with over half the remanence removed at <15 mT (cf. Dunlop, 1983), to many with SD-like stability with MDF of 35- 40 mT (Dunlop 1983), to the greigite sample GR1 with the largest MDF in which half the ARMz remains at 64 mT (Fig. 12a). The differing rotation rates produce rather different MDF of RRM for the same sample (Fig. 12a), with no consistent difference- approximately half (6/13) of the test samples having MDF at 0.5 Hz [rps] lower than that at 2.5 Hz [rps], and half (7 out of 13) the opposite behaviour. A subset of the De Geerdalen Fm samples (circled sample in Fig. 12a) have slightly lower MDF of RRM than MDF of ARMz, which may in part relate to the rather larger uncertainty (order of ca. ± 3 mT) in estimating stability of RRM than that of ARMz (< 1 mT uncertainty). Hence, the magnetite-bearing samples (except the MD-like SVD2) fall into two sets, firstly a lower stability set in which the RRM and ARMz stability are similar (those with MDF of RRM < ca. 42mT; Fig. 12a) with mostly Bg from 0 to -5 μ T (circled samples in Fig. 12); and secondly a set with MDF of RRM larger than the MDF of ARMz and a wide range of Bg (Fig. 12b). The two magnetite bearing samples containing common magnetofossils –CC1b and MR5 (a <2 μ m extract), have the largest MDF of RRM for the magnetite-bearing sets (Fig. 12a), although very different Bg values (Fig. 12b). The differences between CC1b-MR5 perhaps relates to the abundant magnetofossil chains in CC1b.

The greigite sample GR1 has an MDF of RRM of 65-69 mT which is at the lowest end of the range measured for greigite by Snowball (1997b). Nevertheless, the large negative Bg in combination with the high MDF of RRM is a very distinctive feature of greigite (Fig. 12b), confirming the observations of Snowball (1997b). The large-sized pyrrhotites, PY5, PY7 (with MDF of ARMz < 15 mT; Fig.12a) have distinctive positive Bg, and large MDF of RRM comparable to those samples with the smallest magnetite particles (e.g., MR5, CC1b; Fig. 12b).

6. Discussion

6.1 Comparison with other datasets using low rotation rate

Comparison to other datasets that used low ω (less than the AF frequency) is more problematic, since AF hold and ramp-down times have been less clearly described. Potter & Stephenson (1986) used hold and decay times of 5 s and 10 s, and for various sized magnetite's, finding peaks in negative RRM at around 8-10 Hz [rps] ($\omega T_D \approx 80$ -100 revolutions), considerably larger ωT_D than seen here and in Edwards data. Peaks in negative RRM for greigite have not been recognised previously, with existing data from Stephenson & Snowball (2001) showing increasingly more negative RRM from low rotation rates until the AF-frequency threshold.

In Edwards (1982b) magnetite-based data, the negative RRM peak is followed by a trend towards more positive RRM values (both negative and positive RRM) which plateau at around $\omega T_D \approx 20$ -30 revolutions. These approximately concur with largely negative, but some positive RRM values (in basalts) measured by Roperch & Taylor (1986) for ωT_D of ≈ 30 rev (Table 3). Contrastingly, Potter & Stephenson (1986) recognised a positive peak in RRM at ≈ 20 Hz [rps] ($\omega T_D \approx 200$ rev) for crushed magnetite. Hence, it is probable that the RRM peaks and troughs seen in our dataset and those of Edwards (1982b) and Wilson & Lomax (1972), between $\omega T_D = 0.4$ - 30 revolutions, may be hidden in the smallest rotation rates produced by the instrument of Stephenson & Molyneux (1987) at $\omega < 3$ Hz [rps].

6.2 Mineral magnetic identification using RRM

Whilst the comparison of different B_g values at fixed Hz [rps] (or ωT_D) could be useful for simple mineral magnetic discrimination, the changes in B_g and ARM_{ROT} with ω potentially indicate a more powerful means of mineral magnetic discrimination.

There are two broad approaches that could be used for magnetic mineral discrimination using low rotation rates. The first is to use the normalised changes in RRM, ARM_{ROT} and B_g with respect to ωT_D , to build up families of curves for mineral types, granulometry and switching-field behaviours. The data in Figures 3 to 9 are a step in this direction. The second is to parameterise some of the key changes at $\omega T_D \geq 0.4$ rev by looking at ratios of RRM, ARM_{ROT} and B_g at say 0.5 and 2.5 Hz [rps] (ωT_D units of 0.77, 3.83 revolutions), as expression of the changes with ω . We here explore this later approach, since it potentially expresses the between-sample variability better, allowing exploration of larger datasets, and so is more easily used in palaeomagnetic studies focussed on other aims.

Our somewhat limited data on RRM stability (i.e., MDF) also suggests that this may differ between rotation rates (compare test sample 0.5 Hz [rps] and 2.5 Hz [rps] values in Fig. 12). Although MDF of RRM is time consuming to measure, this may perhaps hold some additional information for magnetic mineral discrimination in magnetically stronger samples (e.g., Fig. 12). Although not explored here, the stability of RRM is more usefully utilised in RRM build-up with increasing AF field (see SI Figs. S15-S17, and Potter and Stephenson, 1986, fig.7)- rather than demagnetisation. Median acquisition is free from issues with co-axial GRM's. Alternatively, single step acquisition (say at 40 mT), as a proxy for stability, is also easy to implement and easy to use on samples displaying weak RRM that may need duplicate RRM measurements to improve accuracy.

6.2.1 Magnetic sulphides

Pyrrhotite is recognised by positive B_g at 0.5 or 2.5 Hz [rps] (Figs. 13a, 7c, 8c). The B_g ratios at the rotation rates of 2.5 Hz [rps] divided by 0.3 Hz [rps] (ratios at differing ω hereafter symbolised like $\omega\{2.5/0.3\}$) can also usefully distinguish large pyrrhotite from pyrrhotite $< 20 \mu\text{m}$ in size (Figs. 13a); an expression of the flattish shapes of the RRM- ω curves (Figs. 7c, 8c). An alternative parametrisation is to use the ARM_{ROT} at 2.5 Hz [rps] normalised by ARM_z , which clearly separates the >1.3 values for pyrrhotite from magnetite and greigite behaviours (Fig. 14a, b). Pyrrhotite is particularly challenging to identify using conventional coercivity behaviour, since it strongly overlaps the coercivity range of magnetite, and the useful normalisation by magnetic susceptibility (Peters & Thompson, 1998) is hampered in many sediments by paramagnetic contributions to susceptibility.

Single domain diagenetic greigite has the most distinctive signature in RRM behaviour with large negative B_g , high MDF of RRM and ARM_z (Figs. 12a, 14b, d). These are features also indicated by Snowball (1997b) and Peters & Thompson (1998) for ARM_z . The unusually large B_g and RRM stability probably stem from the magnetic nano-scale composites that make up natural diagenetic greigite crystals (Lesniak et al. 2021). The change of ARM_{ROT} with ω may also be a useful feature, like also seen in the $< 20 \mu\text{m}$ pyrrhotite, both of which increase through $\omega = 0.5$ to 3 Hz [rps] (Fig. 6b, 7b). The ratio of ARM_{ROT} at $\omega\{2.5/0.5\}$ may also be a useful and simple discriminator (Figs. 13b,c,d, 14d).

In contrast, biogenic greigite present in magnetosomes measured by Chen (2014), appears to have low B_g values (at 95 Hz [rps]; Table 2) not much larger than for magnetite magnetosomes. However, Reinholdsson et al. (2013) implicated positive B_g values of 0- 1 μT for greigite magnetofossils at 5 Hz [rps]. A means of using RRM to distinguish these two largely non-interacting SD grain types require more work. Perhaps the change of ARM_{ROT} with ω may be a useful signature, since magnetofossils from the Chalk show particularly dramatic declines in ARM_{ROT} with increasing ω (Fig. 4b), something

that is not seen in our greigite or pyrrhotite samples. Ratios of ARM_{ROT} at $\omega\{2.5/0.5\}$ clearly discriminate the Chalk magnetite magnetofossils from other magnetite samples (Figs. 13c, d; 14d). It remains to be seen if similar behaviour is also shown by greigite magnetofossils.

6.2.2 Magnetite bearing samples

It is interesting that the SD-sized magnetite in the Chalk sample set has consistently the smallest negative B_g values, opposite to the behaviour indicated by the crushed magnetite sample set used by Potter & Stephenson (1986). The small B_g values for the magnetofossils in the Chalk-samples are consistent with the work on magnetite magnetosomes by Chen (2014) at high spin rates. An explanation for the low RRM acquisition in intact magnetofossils/magnetosomes may be related to the model of magnetisation in elongate particles (i.e., equivalent to magnetosome strings) proposed by Potter & Stephenson (2006).

It is challenging to compare the B_g values at high ω with those at low ω . Two ways to approximately cross calibrate these, are to use the B_g for synthetic Mapico magnetite and γFe_2O_3 which have been measured at both low and high spin rates (Tables 2, 3). Using either the Mapico magnetite or mean of Mapico+ γFe_2O_3 gives two possible conversion factors which allows the B_g to grain size data of Potter & Stephenson (1986) to be mapped into the low spin rate data here (scales in top Fig. 13a). It is feasible, that excluding the Chalk samples, the remaining magnetite-bearing samples show differing B_g values corresponding to the particles size changes suggested by Potter & Stephenson (1986), since samples MR5, MR4 have the larger contribution from the finest particle sizes (i.e. SD magnetofossils largely not in chains) in the magnetic extracts (Fig. 13a). Perhaps the particle size, d (in μm) dependency of $d \approx 100/B_g$ (Potter & Stephenson 1986) has compressed much of the apparent grain-size variation in our sample set into a range in B_g of ca. 0-10 μT at 0.5 Hz [rps] (Fig. 13a). An alternative possibility is that the larger B_g values for the crushed samples of Potter & Stephenson (1986) are related to stress, which can impact coercivity, something clearly expressed in hysteresis data, which strongly modifies the coercivity relationship to grain size (Tauxe et al. 2002). Like hysteresis datasets, we speculate that the presence of dislocations allows additional pinning of domain wall motions and so may enhance the irreversible flip-mechanism which is responsible for RRM acquisition. It seems reasonable that during crushing, dislocation density may increase in smaller particles, so increasing B_g . Alternatively, the likely particle interactions present in both our magnetic extract samples, and those of Potter & Stephenson (1986) may modify this behaviour- the RRM response to magnetic interactions needs further work to evaluate this.

Excluding the Chalk samples, magnetite-bearing samples show broadly similar declines in B_g at ω from 0.3 to 2.5 Hz [rps], which can be expressed as the B_g ratio at $\omega\{2.5/0.3\}$ – with samples clustered in the numerical range ca. 0 to 0.7 for this B_g ratio (Fig. 13a, b). The ratio of the ARM_{ROT} for $\omega\{2.5/0.5\}$ shows a better discrimination of these samples (Figs. 13c, d; 14d), which expresses the decline in ARM_{ROT} with ω . The two dolerite samples (SVD1 and SVD2) show very different RRM behaviour, which is rooted in the differing stability of the natural remanence of the Spitsbergen dolerites which varies much, with some showing MDF of NRM < 10 mT, with others up to 40 mT (Halvorsen, 1973). This is reflected in the ARM_z stability of SVD1 and SVD2 which are 42mT and 16 mT respectively, with SVD2 showing behaviour closer to MD-like titanomagnetite with small B_g values and low ARM_z stability and low MDF of RRM at 0.5 Hz [rps] (Figs. 12a; 14c,d). This variability is rooted in the variable oxidation of titanomagnetite in igneous rocks, which impacts ARM_z stability (Dunlop 1983; Figs. 14b, c). The larger ARM_z stability in SVD1 is probably from nanoscale subdivision of the titanomagnetite due to exsolution (cf. Harrison et al. 2002) and titanomagnetite oxidation. This is probably responsible for the large B_g value (-26 μT) for SVD1 at 0.5 Hz [rps] (Fig. 13a). Sample SVD2 shows similar changes in RRM with ω , to basalt sample F37B-1a studied by Edwards (1982b)

derived from R. L. Wilson's samples. All these share a transition into positive RRM values at $\omega T_D > 3$ revolutions (Figs. 4c). Edward's sample F37B-1a had a Bc of 18 mT and Mrs/Ms of 0.13 (Edwards 1982a), which places F37B-1a close to the MD-magnetite field using the squareness versus Bc plot of Tauxe et al. (2002). Perhaps this positive RRM at larger ωT_D represents the RRM response at the border towards truly MD magnetite, but with a small contribution from SD-like material. Truly MD-behaviour (with zero Bg) is shown by Edwards basalt sample D264-26 (Table 3). Hence, increases in ARM_{ROT} for $\omega\{2.5/0.5\}$ and ARM_{ROT}/ARM_z seem to express change towards a more MD state for magnetite-samples, from non-interacting SD-state in the Chalk samples (arrows in Figs. 14b, d). Overall, comparing our dataset to those of basic igneous rocks, not surprisingly shows that the extracts and sediment sample sets fall into regions corresponding to the most oxidized and most stable SD-like behaviour seen in basic igneous rocks (top scale in Fig. 14b, arrows in Fig. 14c). Our data do not therefore provide much in the way of characterisation of the RRM behaviour of low to mid oxidation status basic igneous rocks as characterised by Dunlop (1983)— other than sample SVD2.

Those magnetic extracts corresponding to residual Fe-oxide assemblages, broadly fall into similar intervals as other extracts (Fig. 14a-c). This broadly corresponds with observations of silicate hosted inclusions which have similar chemistry and microstructural characteristics to discrete Fe-oxides (Feinburg et al. 2005; 2006). This is also displayed in the Fe-oxide inclusion-only ARM data of Hounslow & Morton (2004) from UK basement complexes which show a similar range in $d.ARM_{40mT}$ to the samples here (arrows at top in Fig. 14d). The De Geerdalen Formation samples are remarkably well clustered considering the range of locations and lithology types that occur in these samples (Figs. 13, 14). In addition their properties do not overlap those of the magnetic extracts (Figs. 14a, c, d), but do overlap with the range of $d.ARM_{40mT}$ seen in silicate hosted inclusions. Hence, presumably these contain more SD-like magnetite which is intermediate towards the Chalk samples, with a larger MDF of ARM_z (Fig. 14c). Although magnetic extracts have not been performed on these samples, it seems highly unlikely they contain magnetofossils, due to the rather extensive silicate and carbonate diagenesis (Mørk, 2013), but magnetite inclusions in silicates likely make significant contributions.

7. Conclusions

Using rotation rates of 0.26 to 3 Hz [rps] there is the possibility for routine magnetic mineral characterisation using RRM and rotational anhysteretic magnetisation (ARM_{ROT}). Characterisation is best done using either: 1) normalised ω —RRM curve characteristics (or ω —Bg, ω — ARM_{ROT} curves), This approach allows more effective characterisation of the mineralogical behaviour, rather than relying on single spin rate-derived values of Bg, RRM or ARM_{ROT} ; or 2) parametrisation of the variations using values at selected rotation rates (or better at fixed ωT_D values). The later approach is likely more widely accessible if rotation rates cannot be continuously varied in equipment available. Optimisation of the AF field hold time to achieve full rotational initialisation of RRM will improve consistency, especially so for investigating greigite (and other strongly anisotropic samples), which shows large changes in RRM and ARM_{ROT} at rotation angles below the initialisation threshold caused by anisotropy.

Static AF demagnetisation of the RRM, for stability tests, is best achieved by demagnetisation of both $+\omega$ and $-\omega$ RRM's which allows removal of gyroremanence acquired along the axis of demagnetisation. A simpler approach free from this problem is to characterise stability using RRM acquisition with increasing AF field- this is probably best standardized at $\omega T_D = 0.4$ revolutions, since

RRM stability varies with rotation rate, and RRM is maximised at $\omega T_D = 0.4$. This allows RRM stability to be parameterized even in samples acquiring a weak RRM.

The sized pyrrhotite and pyrrhotite bearing phyllite samples show largely positive RRM, in contrast to negative RRM largely acquired by test samples of magnetite and greigite. This and the smaller variation of RRM and ARM_{ROT} with rotation rate are a simple effective tool for detecting pyrrhotite. The median destructive field of RRM produced by pyrrhotite (including large grains) is comparable to greigite and larger than most test samples of magnetite. Samples of diagenetic greigite display large negative B_g values and a stronger variation of RRM and ARM_{ROT} with spin rate. The large B_g values carried by diagenetic greigite are a simple and easy way to identify it, but additionally diagnostic are the ratio of ARM_{ROT} at $\omega\{2.5/0.5\}$ and MDF of a conventional static ARM. RRM distinction of greigite magnetofossils from magnetite magnetofossils needs more evaluation, but utilising ω - ARM_{ROT} changes or ARM_{ROT} stability may be diagnostic.

The set of natural magnetite-bearing test samples shows that B_g is not simply related to grain size as thought previously, but non-interacting SD magnetite in magnetofossils have very small B_g and little variation with ω . A small B_g value concurs with studies by Chen (2014) measured at high spin rates on magnetite magnetosomes. The ratio of ARM_{ROT} at $\omega\{2.5/0.5\}$ may be a better tool for particle size characterisation of magnetite. For magnetite, the B_g parameter may also be strongly impacted by presence of dislocations, or perhaps interaction-related controls— features that need further study. The prior extensive study of RRM on sized and crushed magnetite by Potter & Stephenson (1986), may have been impacted by particle size related dislocation density in the magnetite samples, which may have enhanced the B_g variation with grain size. The great advantage of using rotational remanent magnetisation (RRM) characteristics for magnetic mineral identification is the RRM properties are carried by the hardest coercivity grains most relevant to understanding stable palaeomagnetic signals.

Acknowledgements

Paul Montgomery helped collect the Chalk samples, and Gareth Lord some of the Svalbard samples. Isaac Hilburn helped unravelling some complexities of the RAPID software.

Author contribution statement: MWH, VK, C-S.H processed the data. MWH analysed the magnetic results. All contributed to writing of the paper.

Sample Data Availability Statement: All data are incorporated into the article and its online supplementary material.

References

- Chen, A.P., 2014. *Rock magnetic properties of uncultivated magnetotactic bacteria and paleo-redox changes across the Paleocene-Eocene boundary, New Jersey Coastal Plain*. Unpubl. PhD Macquarie Univ.
- Cisowski, S., 1981. Interacting vs. non-interacting single domain behavior in natural and synthetic samples. *Physics of the Earth and Planetary Interiors*, **26**, 56-62.
- Dunlop, D.J., 1983. Determination of domain structure in igneous rocks by alternating field and other methods. *Earth and Planetary Science Letters*, **63**, 353-367.
- Edwards, J., 1980a. An experiment relating to rotational remanent magnetization and frequency of demagnetizing field. *Geophysical Journal International*, **60**, 283-288.

- Edwards, J., 1980b. Comparisons between the generation and properties of rotational remanent magnetization and anhysteretic remanent magnetization. *Geophysical Journal International*, **62**, 379-392.
- Edwards, J., 1982a. Gyroremanent magnetization produced by specimen rotation between successive alternating field treatments. *Geophysical Journal International*, **71**, 199-214.
- Edwards, J., 1982b. Studies of partial rotational remanent magnetization and rotational remanent magnetization at slow speeds of rotation. *Geophysical Journal International*, **68**, 609-624.
- Edwards, J., 1984. Partial anhysteretic remanent magnetizations produced in rotating samples, and comparisons with corresponding rotational remanent magnetizations. *Geophysical Journal International*, **77**, 619-637.
- Edwards, J. & Desta, M., 1989. Static alternating field demagnetizations of anhysteretic and rotational remanent magnetizations in rocks and synthesized samples. *Geophysical Journal International*, **99**, 739-748.
- Feinberg, J.M., Scott, G.R., Renne, P.R. & Wenk, H.R., 2005. Exsolved magnetite inclusions in silicates: Features determining their remanence behavior. *Geology*, **33**, 513-516.
- Feinberg, J.M., Harrison, R.J., Kasama, T., Dunin-Borkowski, R.E., Scott, G.R. & Renne, P.R., 2006. Effects of internal mineral structures on the magnetic remanence of silicate-hosted titanomagnetite inclusions: An electron holography study. *Journal of Geophysical Research: Solid Earth*, **111**, doi.org/10.1029/2006JB004498.
- Finn, D. & Coe, R., 2020. Consequences of switching field angular dependence for applications of anhysteretic remanent magnetization. *Physics of the Earth and Planetary Interiors*, **305**, doi.org/10.1016/j.pepi.2020.106507
- Franke, C., von Dobeneck, T., Drury, M.R., Meeldijk, J.D. & Dekkers, M.J., 2007. Magnetic petrology of equatorial Atlantic sediments: Electron microscopy results and their implications for environmental magnetic interpretation. *Paleoceanography and Paleoclimatology*, **22**, doi.org/10.1029/2007PA001442.
- Gayer, R.A., Gee, D.G., Harland, W.B., Miller, J.A., Spall, H.R., Wallis, R.H. and Winsnes, T.S., 1966. *Radiometric age determinations on rocks from Spitsbergen*. Norsk Polarinst. Skrifter 137, pp 39.
- Haile, B.G., Klausen, T.G., Czarniecka, U., Xi, K., Jahren, J. and Hellevang, H., 2018. How are diagenesis and reservoir quality linked to depositional facies? A deltaic succession, Edgeøya, Svalbard. *Marine and Petroleum Geology*, **92**, 519-546.
- Halvorsen, E., 1973. Demagnetization studies of the late Mesozoic dolerites from the Isfjorden area, Spitsbergen. *Norsk Polarinstitutt. Arbok for 1971*, 2-29.
- Hailwood, E.A. & Molyneux, L., 1974. Anhysteretic remanent magnetization due to asymmetrical alternating fields. *Geophysical Journal International*, **39**, 421-434.
- Harrison, R.J., Dunin-Borkowski, R.E. & Putnis, A., 2002. Direct imaging of nanoscale magnetic interactions in minerals. *Proceedings of the National Academy of Sciences*, **99**, 16556-16561.

- Hornig, C.S., 2018. Unusual magnetic properties of sedimentary pyrrhotite in methane seepage sediments: Comparison with metamorphic pyrrhotite and sedimentary greigite. *Journal of Geophysical Research: Solid Earth*, **123**, doi.org/10.1002/2017JB015262.
- Hornig, C.S. & Roberts, A.P., 2006. Authigenic or detrital origin of pyrrhotite in sediments?: Resolving a paleomagnetic conundrum. *Earth and Planetary Science Letters*, **241**, 750-762.
- Hornig, C.S., Huh, C.A., Chen, K.H., Lin, C.H., Shea, K.S. & Hsiung, K.H., 2012. Pyrrhotite as a tracer for denudation of the Taiwan orogen. *Geochemistry, Geophysics, Geosystems*, **13**, doi.org/10.1029/2012GC004195
- Hornig, C.S., Torii, M., Shea, K.S. and Kao, S.J., 1998. Inconsistent magnetic polarities between greigite-and pyrrhotite/magnetite-bearing marine sediments from the Tsailiao-chi section, southwestern Taiwan. *Earth and Planetary Science Letters*, **164**, 467-481.
- Hounslow, M.W., 1996. Ferrimagnetic Cr and Mn spinels in sediments: residual magnetic minerals after diagenetic dissolution. *Geophysical research letters*, **23**, 2823-2826.
- Hounslow, M.W. 2019. GM4Edit (v.5.6) - a windows program to manage, plot, export and manipulate palaeomagnetic magnetometer datasets. doi.org/10.13140/RG.2.2.31877.91361/1.
- Hounslow, M.W. & Maher, B.A., 1996. Quantitative extraction and analysis of carriers of magnetization in sediments. *Geophysical Journal International*, **124**, 57-74.
- Hounslow, M.W. & Maher, B.A., 1999. Laboratory procedures for quantitative extraction and analysis of magnetic minerals from sediments. In *Environmental Magnetism, A Practical Guide*. eds Oldfield, F., Smith, J.P. Quaternary Research Association, Technical Guide, 6, pp. 139-164.
- Hounslow, M.W. & Morton, A.C., 2004. Evaluation of sediment provenance using magnetic mineral inclusions in clastic silicates: comparison with heavy mineral analysis. *Sedimentary Geology*, **171**, 13-36.
- Hounslow, M.W. Samuel E. Harris, Karloukovski, V. & Mørk, A. 2022. Geomagnetic polarity and carbon isotopic stratigraphic assessment of the Carnian- Norian boundary on Hopen and Wilhelmøya (Svalbard). *Norwegian Journal of Geology*, **102**, 202204, <https://dx.doi.org/10.17850/njg102-1-4>.
- Hounslow, M.W., Hu, M., Mørk, A., Vigran, J.O., Weitschat, W. & Orchard, M.J., 2007. Magneto-biostratigraphy of the Middle to Upper Triassic transition, central Spitsbergen, arctic Norway. *Journal of the Geological Society*, **164**, 581-597.
- Hounslow, M.W., Maher, B.A. & Thistlewood, L., 1995. Magnetic mineralogy of sandstones from the Lunde Formation (late Triassic), northern North Sea, UK: origin of the palaeomagnetic signal. In *Palaeomagnetic Applications in Hydrocarbon Exploration and Production*, pp. 119-147, eds Turner, P & Turner, A. Geological Society, London, Special Publications, **98**.
- Hu, S., Appel, E., Hoffmann, V., Schmahl, W.W. & Wang, S., 1998. Gyromagnetic remanence acquired by greigite (Fe₃S₄) during static three-axis alternating field demagnetization. *Geophysical Journal International*, **134**, 831-842.

- Hu, S., Stephenson, A. & Appel, E., 2002. A study of gyroremanent magnetisation (GRM) and rotational remanent magnetisation (RRM) carried by greigite from lake sediments. *Geophysical Journal International*, **151**, 469-474.
- Jiang, W.T., Horng, C.S., Roberts, A.P. and Peacor, D.R., 2001. Contradictory magnetic polarities in sediments and variable timing of neoformation of authigenic greigite. *Earth and Planetary Science Letters*, **193**, 1-12.
- Kirschvink, J.L., Kopp, R.E., Raub, T.D., Baumgartner, C.T. & Holt, J.W., 2008. Rapid, precise, and high-sensitivity acquisition of paleomagnetic and rock-magnetic data: Development of a low-noise automatic sample changing system for superconducting rock magnetometers. *Geochemistry, Geophysics, Geosystems*, **9**, doi.org/10.1029/2007GC001856
- Kopp, R.E. & Kirschvink, J.L., 2008. The identification and biogeochemical interpretation of fossil magnetotactic bacteria. *Earth-Science Reviews*, **86**, 42-61.
- Krumsiek, K., Nagel, J. & Nairn, A.E.M., 1968. Record of palaeomagnetic measurements on some igneous rocks from the Isfjorden region, Spitsbergen. *Norsk Polarinstitutt Årbok 1966*, 76-83.
- Lesniak, B., Koulialias, D., Charilaou, M., Weidler, P.G., Rhodes, J.M., Macdonald, J.E. & Gehring, A.U., 2021. Polycrystalline texture causes magnetic instability in greigite. *Scientific Reports*, **11**, 1-10.
- Madsen, K.N, 2004. Angular dependence of the switching field and implications for gyromagnetic remanent magnetization in three-axis alternating-field demagnetization. *Geophysical Journal International*, **157**, 1007-1016.
- Madsen, K.N., 2003. A reversed gyromagnetic effect in chromium dioxide particles. *Journal of magnetism and magnetic materials*, **260**, 131-140.
- Maher, B.A. & Hounslow, M.W., 1999. The significance of magnetotactic bacteria for the palaeomagnetic and rock magnetic record of Quaternary sediments and soils. In: Tarling, D.H & Turner, P. eds, Palaeomagnetism and diagenesis in sediments. *Geological Society, London, Special Publications*, **151**, 43-46.
- Maher, B.A. & Hallam, D.F., 2005. Magnetic carriers and remanence mechanisms in magnetite-poor sediments of Pleistocene age, southern North Sea margin. *Journal of Quaternary Science*, **20**, 79-94.
- Mahon, S.W. & Stephenson, A., 1997. Rotational remanent magnetization (RRM) and its high temporal and thermal stability. *Geophysical Journal International*, **130**, 383-389.
- Montgomery, P., Hailwood, E.A., Gale, A.S. & Burnett, J.A., 1998. The magnetostratigraphy of Coniacian-Late Campanian chalk sequences in southern England. *Earth and Planetary Science Letters*, **156**, 209-224.
- Mørk, M.B.E., 2013. Diagenesis and quartz cement distribution of low-permeability Upper Triassic–Middle Jurassic reservoir sandstones, Longyearbyen CO₂ lab well site in Svalbard, Norway. *AAPG bulletin*, **97**, 577-596.
- Nejbert, K., Krajewski, K.P., Dubinska, E. & Pecskay, Z., 2011. Dolerites of Svalbard, north-west Barents Sea Shelf: age, tectonic setting and significance for geotectonic interpretation of the High-Arctic Large Igneous Province. *Polar Research*, **30**, doi.org/10.3402/polar.v30i0.7306.

- Noel, M., 1988. Some observations of the gyroremanent magnetization acquired by rocks in a rotating magnetic field. *Geophysical Journal International*, **92**, 107-110.
- Peters, C. & Thompson, R., 1998. Magnetic identification of selected natural iron oxides and sulphides. *Journal of Magnetism and Magnetic Materials*, **183**, 365-374.
- Potter, D.K., 2004. A comparison of anisotropy of magnetic remanence methods—a user's guide for application to palaeomagnetism and magnetic fabric studies. In: Martin-Hernandez, F., Lüneburg, C. M., Aubourg, C. & Jackson, M. (eds) 2004. *Magnetic fabric: methods and applications*. Geological Society, London, Special Publications, **238**, 21-35.
- Potter, D.K. & Stephenson, A., 1986. The detection of fine particles of magnetite using anhysteretic and rotational remanent magnetizations. *Geophysical Journal International*, **87**, 569-582.
- Potter, D.K. & Stephenson, A., 2006. The stable orientations of the net magnetic moment within single-domain particles: Experimental evidence for a range of stable states and implications for rock magnetism and palaeomagnetism. *Physics of the Earth and Planetary Interiors*, **154**, 337-349.
- Reinholdsson, M., Snowball, I., Zillén, L., Lenz, C. & Conley, D.J., 2013. Magnetic enhancement of Baltic Sea sapropels by greigite magnetofossils. *Earth and Planetary Science Letters*, **366**, 137-150.
- Roberts, A.P., 2015. Magnetic mineral diagenesis. *Earth-Science Reviews*, **151**, 1-47.
- Roberts, A.P., Chang, L., Rowan, C.J., Horng, C.S. & Florindo, F., 2011. Magnetic properties of sedimentary greigite (Fe₃S₄): An update. *Reviews of Geophysics*, **49**, doi.org/10.1029/2010RG000336
- Roperch, P. & Taylor, G.K., 1986. The importance of gyromagnetic remanence in alternating field demagnetization. Some new data and experiments on GRM and RRM. *Geophysical Journal International*, **87**, 949-965.
- Slotznick, S.P., Winston, D., Webb, S.M., Kirschvink, J.L. & Fischer, W.W., 2016. Iron mineralogy and redox conditions during deposition of the mid-Proterozoic Appekunny Formation, Belt Supergroup, Glacier National Park. in *Belt Basin: Window to Mesoproterozoic Earth*, pp. 1–22, eds MacLean, J.S., and Sears, J.W., Society of America Special Paper 522, doi:10.1130/2016.2522(09).
- Snowball, I.F., 1997a. Gyroremanent magnetization and the magnetic properties of greigite-bearing clays in southern Sweden. *Geophysical Journal International*, **129**, 624-636.
- Snowball, I.F., 1997b. The detection of single-domain greigite (Fe₃S₄) using rotational remanent magnetization (RRM) and the effective gyro field (Bg): mineral magnetic and palaeomagnetic applications. *Geophysical Journal International*, **130**, 704-716.
- Stephenson, R.W., 1976. A study of rotational remanent magnetization. *Geophysical Journal International*, **47**, 363-373.
- Stephenson, A., 1980. Rotational remanent magnetization and the torque exerted on a rotating rock in an alternating magnetic field. *Geophysical Journal International*, **62**, 113-132.
- Stephenson, A. 1981. Gyromagnetic remanence and anisotropy in single domain particles, rocks and magnetic recording tape, *Philosophical Magazine B*, **44**, 635 -664.

- Stephenson, A., 1985. The angular dependence of rotational and anhysteretic remanent magnetizations in rotating rock samples. *Geophysical Journal International*, **83**, 787-796.
- Stephenson, A. & Molyneux, L., 1987. The rapid determination of rotational remanent magnetization and the effective field which produces it. *Geophysical Journal International*, **90**, 467-471.
- Stephenson, A., 1988. Gyromagnetic remanence produced by rotation of magnetite and maghemite particles in a slowly reducing direct field. *Journal of magnetism and magnetic materials*, **71**, 179-185.
- Stephenson, A. & Snowball, I.F., 2001. A large gyromagnetic effect in greigite. *Geophysical Journal International*, **145**, 570-575.
- Tauxe, L., Bertram, H.N. & Seberino, C., 2002. Physical interpretation of hysteresis loops: Micromagnetic modeling of fine particle magnetite. *Geochemistry, Geophysics, Geosystems*, **3**, doi.org/10.1029/2001GC000241.
- Thomson, G.F., 1990. The anomalous demagnetization of pyrrhotite. *Geophysical Journal International*, **103**, 425-430.
- Vincenz, S.A., Jeleńska, M., Aiinehsazian, K. & Birkenmajer, K., 1984. Palaeomagnetism of some late Mesozoic dolerite sills of east central Spitsbergen, Svalbard Archipelago. *Geophysical Journal International*, **78**, 751-773.
- Watkins N. D. & Haggerty S. E. 1967. Primary oxidation variation and petrogenesis in a single lava. *Contributions to Mineralogy and Petrology*, **15**, 251-71.
- West, G.F. & Dunlop, D.J., 1971. An improved ballistic magnetometer for rock magnetic experiments. *Journal of Physics E: Scientific Instruments*, **4**, 37.
- Wilson, R.L. & Lomax, R., 1972. Magnetic remanence related to slow rotation of ferromagnetic material in alternating magnetic fields. *Geophysical Journal International*, **30**, 295-303

Figure captions

Fig. 1. Schematic view of the rotational remanent magnetisation (RRM) and rotational anhysteretic magnetisation (ARM_{ROT}) measurement process. The rotation rate (ω) is symbolised also with a + or - sign indicating the down, or up-directed rotation vector. Inset shows the timing relationships between sample rotation and stages in the AF field build-up, hold and decay stages and their symbolised timings.

Fig. 2. Example micrographs of some of the test samples. A) Optical reflected light micrograph of sample PY2 (5-10 μm detrital monoclinic pyrrhotite magnetically separated from river sediment). B) Backscatter scanning electron microscope (BSE) image of pyrrhotite bearing phyllite. The brightest phase is pyrite, and the more abundant slightly greyer phase is pyrrhotite, both embedded in a fine-grained phyllosilicate-quartz matrix. C) BSE image of ca. $<0.5 \mu\text{m}$ in size, brighter greigite embedded in a clastic-phyllosilicate rich matrix. D) Transmission electron microscope image of chains of magnetofossils in a magnetic extract from Chalk sample at level of CC2. See the supplementary information for more details on the test samples.

Fig. 3. Magnetic extract samples LUD, OR2, OR3, MR1, MR2 and MR5. Variation of: a) normalised RRM, b) normalised rotational ARM (ARM_{ROT}) and c) Bg with revolution rate (ω in Hz [rps]). In a) and b) the absolute value for that at 0.5 Hz [rps] is used for normalisation. In a) sample OR3, MR2 share the right-hand scale. The legend in B) applies to all sub-panels. In b) is the ARM generated in the

same way as the RRM, but with zero rotation (ARM_{TRAN}). Additional scale in c) is ωT_D (in revolutions), where T_D is the decay time of the AF field in seconds.

Fig. 4. Chalk (CC1, CC2) and dolerite (SVD1, SVD2) test samples. In c) only sample SVD1 has a separate scale for B_g . See Fig. 3 caption for details.

Fig. 5. De Geerdalen Formation test samples DF1 to DF6. See Fig. 3 caption for details.

Fig. 6. Greigite-bearing siltstone test samples GR1 to GR4. See Fig. 3 caption for details.

Fig. 7. Sized detrital pyrrhotite test samples PY1 to PY5. In a) PY4 and PY5 share the right-hand scale. See Fig. 3 caption for details.

Fig. 8. Pyrrhotite bearing phyllite test samples PY6 to PY9. See Fig. 3 caption for details.

Fig. 9. RRM and ARM_{ROT} of test samples with three AF field hold times (T_H) of 0.092 s, 0.917 s and 9.17 s. A, B) are for magnetite sample MR1, C, D) for pyrrhotite sample PY5, and E, F) for diagenetic greigite sample GR1. The dotted vertical red lines in A,C,E) are the rotation rate thresholds at which the two smaller T_H values have full 90° of rotation at the maximum field of 100 mT. The longest hold time of 9.17s achieves 90° rotation at maximum field even at 0.05 Hz [rps]. Error bars are the 1σ uncertainty (smaller than symbols in C and E) from the remanence measurement. Most of the uncertainty in B, D, F relate to the uncertainty in the zero level of the ARM_{ROT} . Points are connected by an Excel fitted 'smoothed-curve'.

Fig. 10. Example demagnetisation of RRM obtained for both $+\omega$ and $-\omega$ conditions (both 0.5 Hz [rps] and 2.5 Hz [rps]). Static demagnetisation is along the Z-axis parallel to the rotation axis (Fig. 1). Left panels in each case show the RRM and GRMz curves in magnetic moment (Am^2) corrected for the subtraction and addition operations on the raw moments. Right panels show the X-Y axis GRM moment ($\sqrt{X^2+Y^2}$) for each of the four spin measurements (two for each ω) during demagnetisation. In each case the baselines have not been adjusted to zero. The measurement order is AFz demagnetisation at 150 mT, RRM ($-\omega=0.5$ Hz [rps]), progressive AF demagnetisation, RRM ($+\omega=0.5$ Hz [rps]), progressive AF demagnetisation; to be followed by the same four sets at 2.5 Hz [rps]. A) Arrows show the sign of the GRMz for increasing negative, and positive values respectively.

Fig. 11. A) B_g versus the effective field (B_gZ) of the additional nuisance magnetisation (GRMz) generated during static demagnetisation of the RRM (i.e., Fig. 10). Datasets for both $\omega=0.5$ Hz [rps] and 2.5 Hz [rps] are shown. Note both negative (upwards directed) and positive (downward directed) GRMz. Arrows indicate the off-graph positions of the greigite sample and its respective B_g values at $\omega=0.5$ and 2.5 Hz [rps]. B) Ratio of GRMz and ARMz expressed as a percentage with respect to the ARMz moment. Note the often much larger %GRMz/ARMz values for greigite and pyrrhotite. In each case the error bars include the RRM measurement uncertainties plus the baseline uncertainty for GRMz, both as $\pm 1\sigma$.

Fig. 12. Median destructive field (MDF) of the RRM versus MDF of ARMz in a) and B_g in b). This uses RRM demagnetisations using method -2 for both 0.5 Hz [rps] and 2.5 Hz [rps]. In a) note the soft ARMz (<20 mT) of the 'large'-pyrrhotite and dolerite sample SVD2, the hard ARMz (~64 mT) of greigite sample GR1, and the rather consistent intermediate ARMz stability (35-41 mT) of other samples. Both the 0.5 and 2.5 Hz [rps] measurements of greigite sample GR1 plots off the x-axis in b) at a B_g of -53 μT and -96 μT (Fig. 6c).

Fig. 13. Biplots of B_g and ARM_{ROT} ratios illustrating possible visualisation of mineral magnetic discrimination. In a) at top are shown two possible scales of B_g conversion from the high spin rate datasets (sized and crushed magnetite) of Potter and Stephenson (1986)– scale in microns. The lower micron scale is using the Mapico magnetite (Tables 2,3) with B_g value of -8 mT (at $\omega_{TD} = 1.05$ revolutions), which gives a high to low spin B_g conversion factor of -0.022. The upper micron scale is using γFe_2O_3 (GF01, TDK type D; Tables 2,3), which gives a conversion factor of -0.089. The magnetite-bearing samples marked as ‘residual’ contain a residual magnetic assemblage after extensive diagenetic dissolution (sample LUD only in this figure). The diagenetic greigite samples plot-off to the left of the graph in a), c) and d).

Fig. 14. Biplots of RRM, ARM_z and demagnetisation stability, illustrating possible visualisation of mineral magnetic discrimination. In b) and c) $d.ARM_{z40mT}$ is the proportion of the initial ARM_z remaining after 40 mT static-axis demagnetisation. Regions on the plots for pyrrhotite are loosely defined with a ‘bag’, and the $B_g=0$ line indicates truly MD magnetite in a) and c). Those marked as ‘residual’ contain a residual magnetic assemblage after extensive diagenetic dissolution (samples LUA, LUD, LUD2, LUD3, OR4, OR5, OR6, MR6; Table 4). Various additional unlabelled samples are shown from the Chalk and De Geerdalen Fm sample sets (See SI datasets). B) top scales show the $d.ARM_{z40mT}$ values for the petrological oxidation states I to VI (Watkins & Haggerty 1967) of basalts from the Steen’s Mountain and Icelandic basalts (from Dunlop, 1983). C) Arrows on right show the mean (the tick) and standard deviation (1σ) range of the MDF of ARM_z for basic igneous rock classed as single domain (SD) type by Dunlop (1983) with the dotted arrow showing the maximum MDF in this class. Dunlop’s (1983) MD-type mean and 1σ range falls below 10 mT (so off the graph). D) Top arrow is the mean (tick) and range of $d.ARM_{z40mT}$ from Fe-oxides inclusions in silicates (Hounslow & Morton, 2004) for nine UK basement complexes (all discrete Fe-oxides outside silicates removed). The greigite samples plot off the graphs to the left in a) and c).

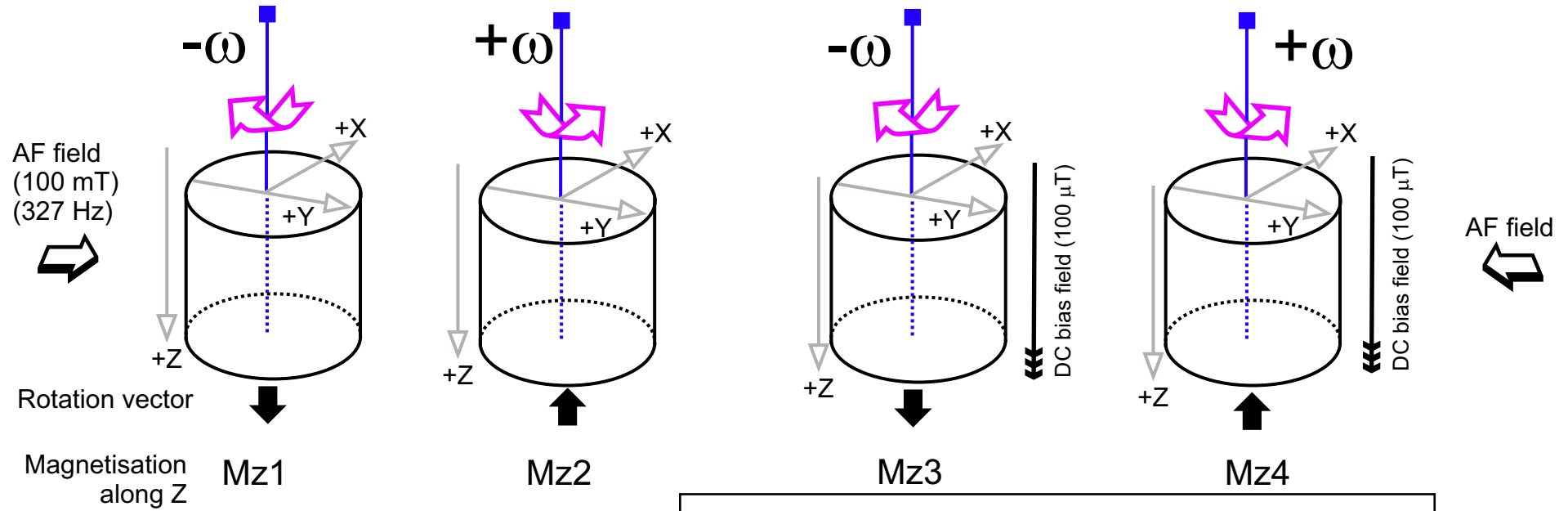
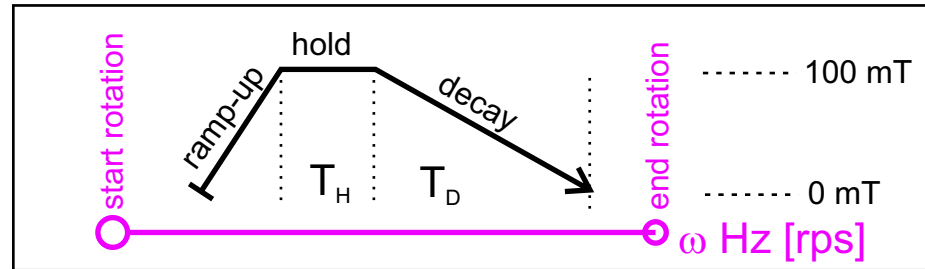


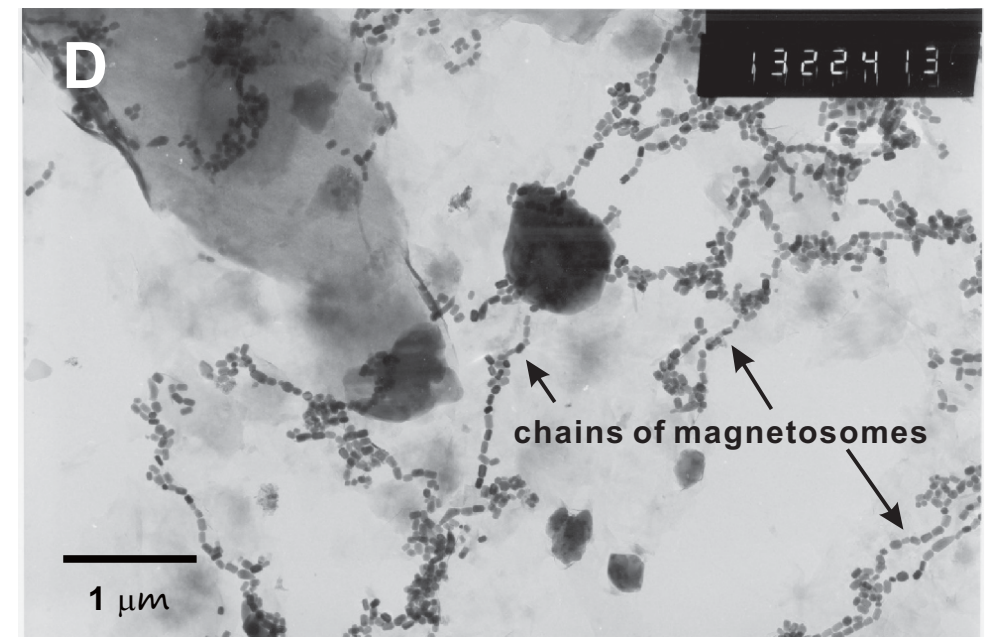
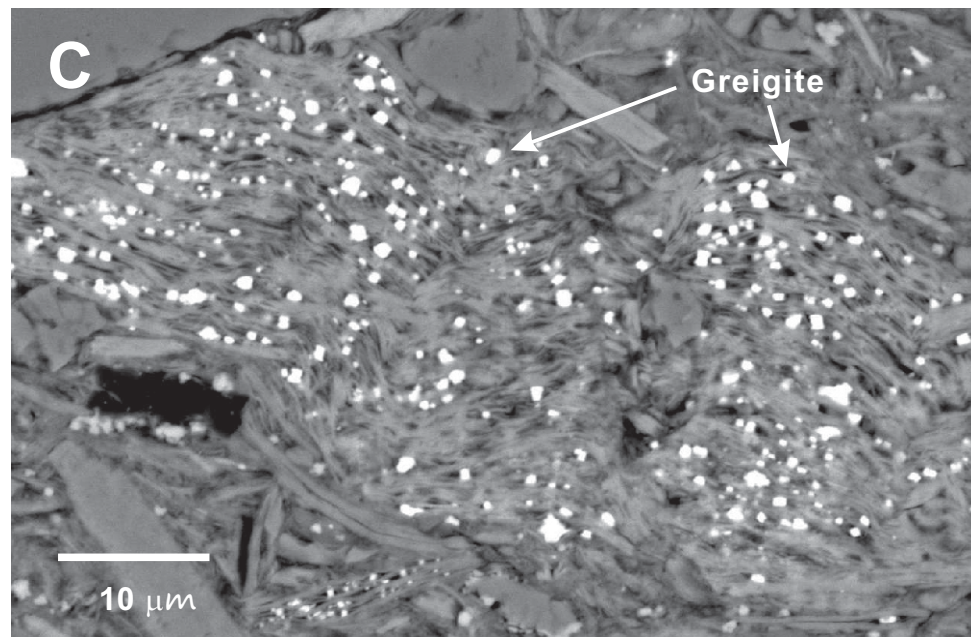
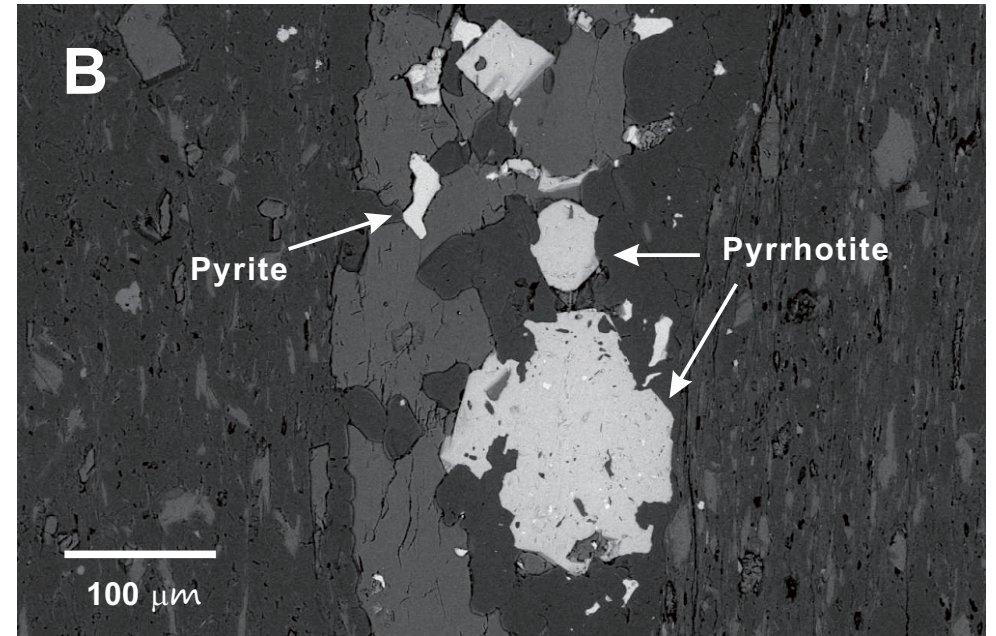
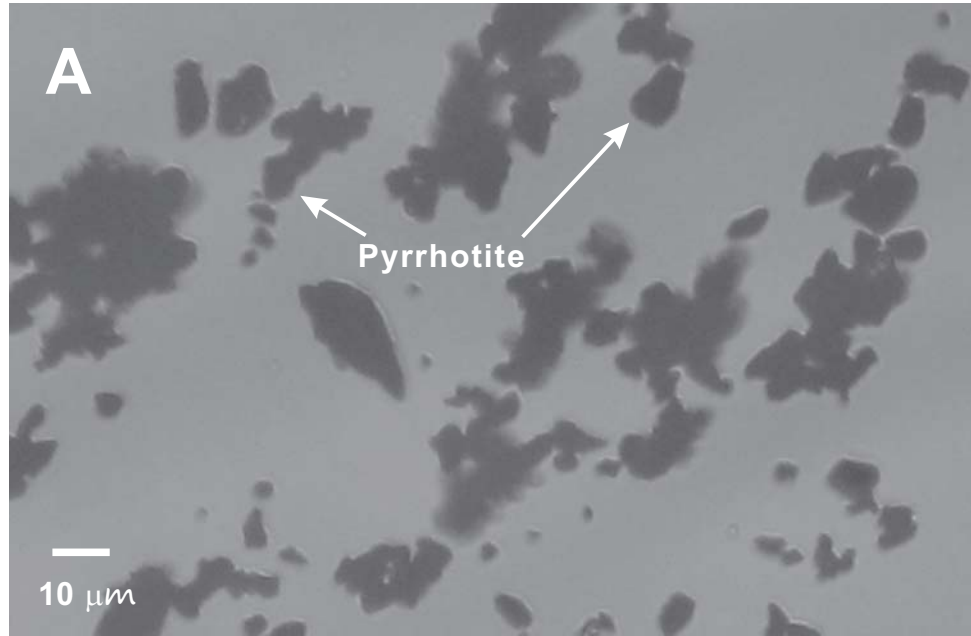
fig. 1

$$RRM = (Mz1 - Mz2) / 2$$

$$ARM_{ROT} = (Mz3 + Mz4) / 2$$

$$RRM_{100} = (Mz3 - Mz4) / 2$$





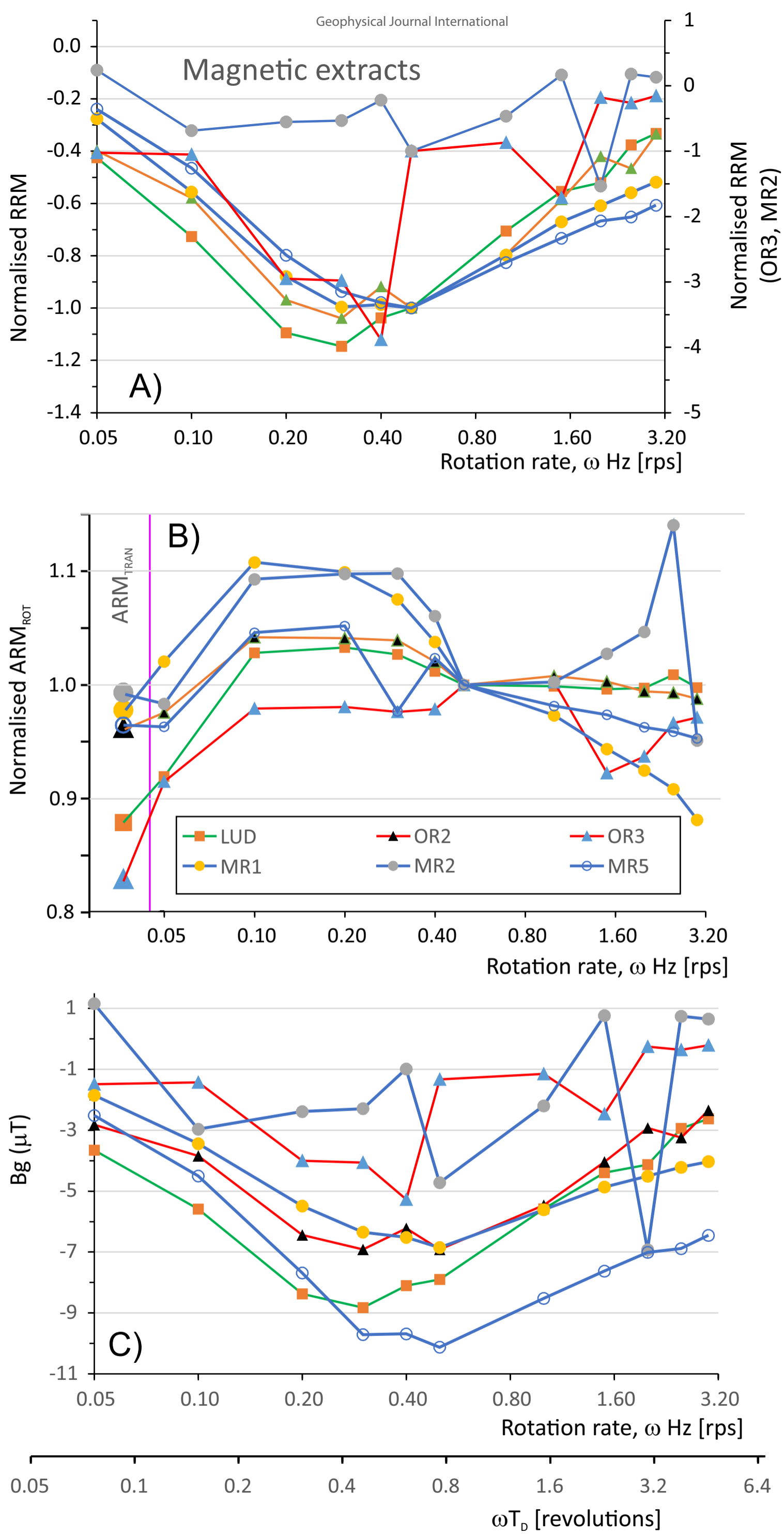


fig. 3

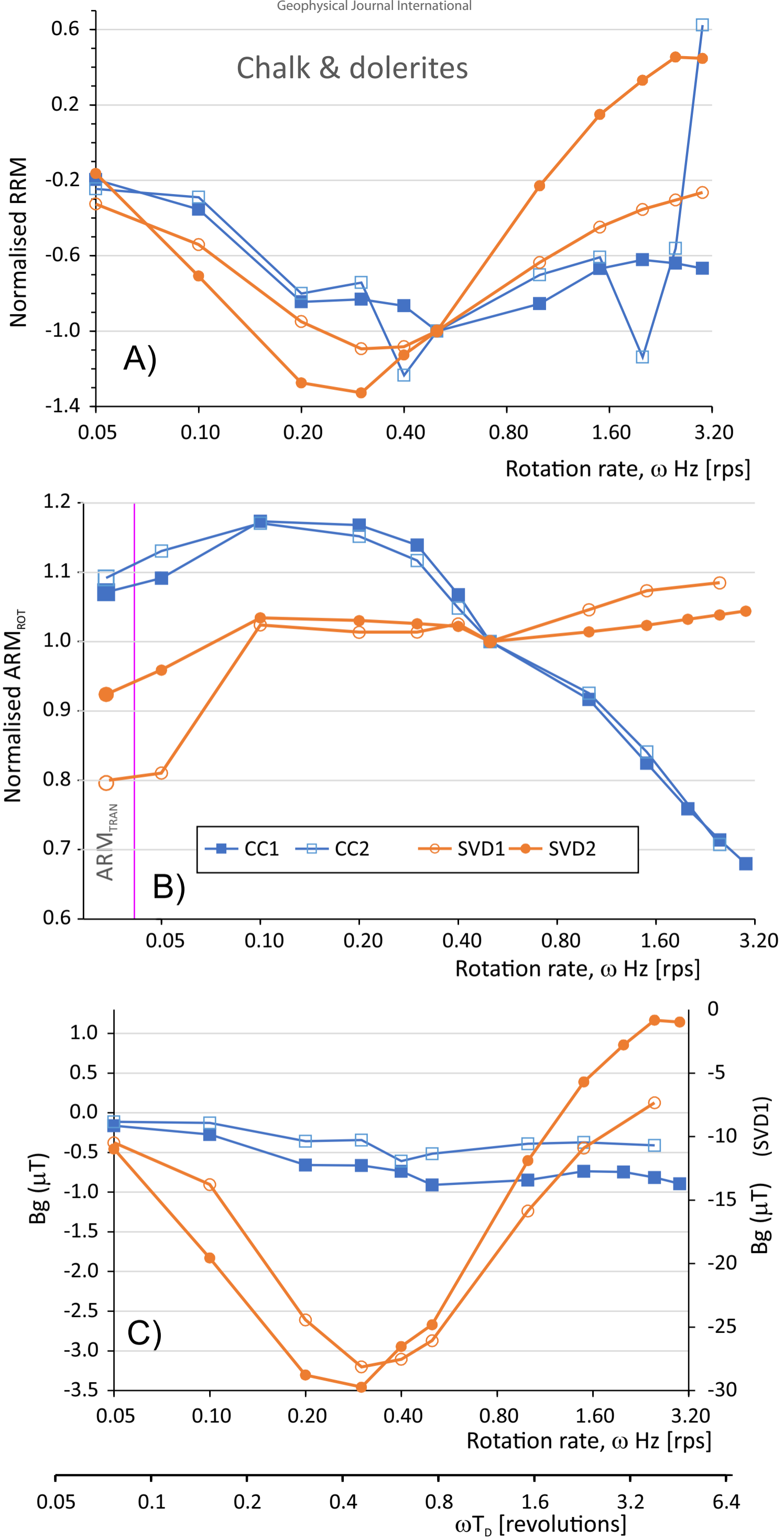


fig. 4

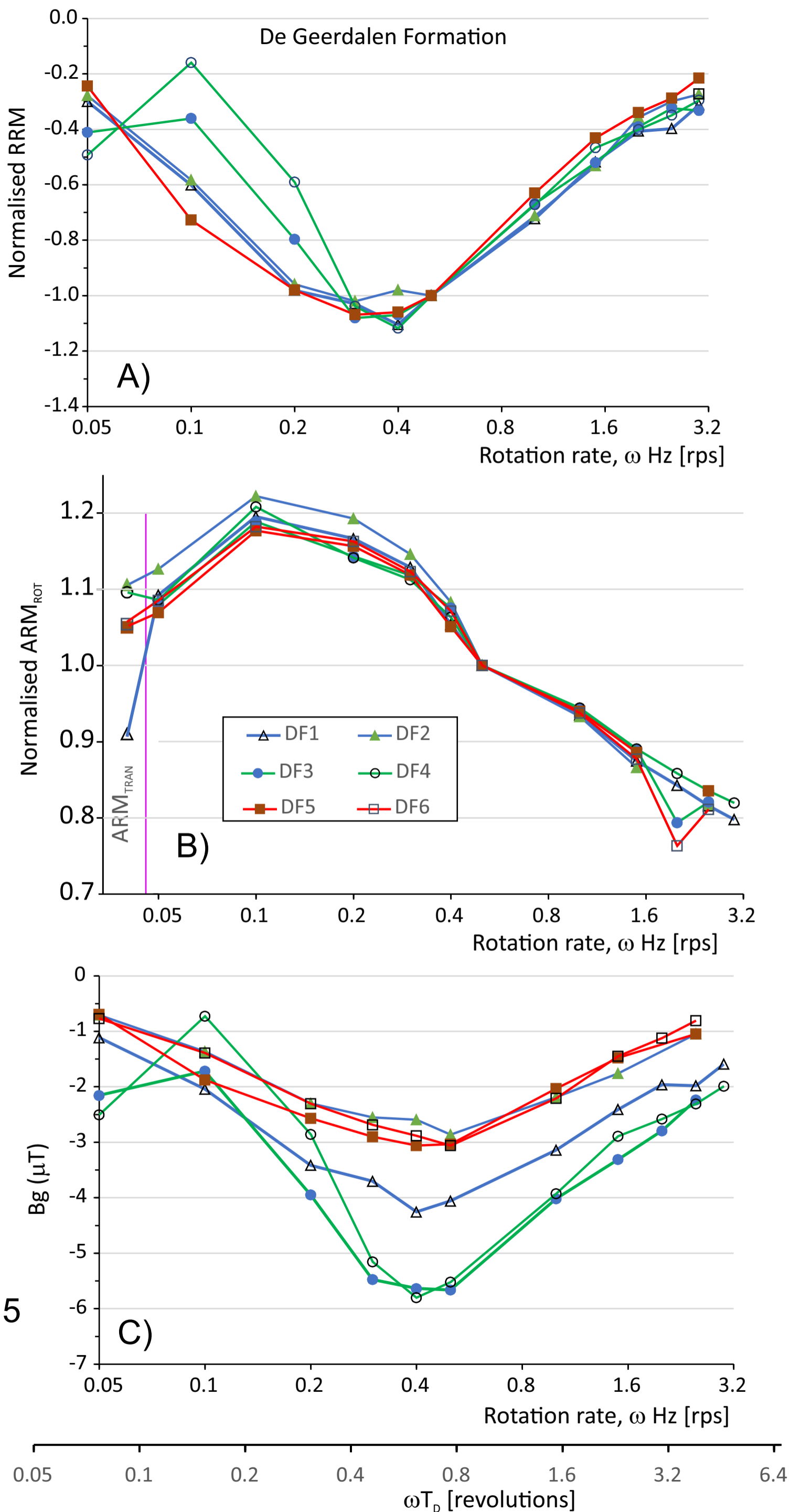
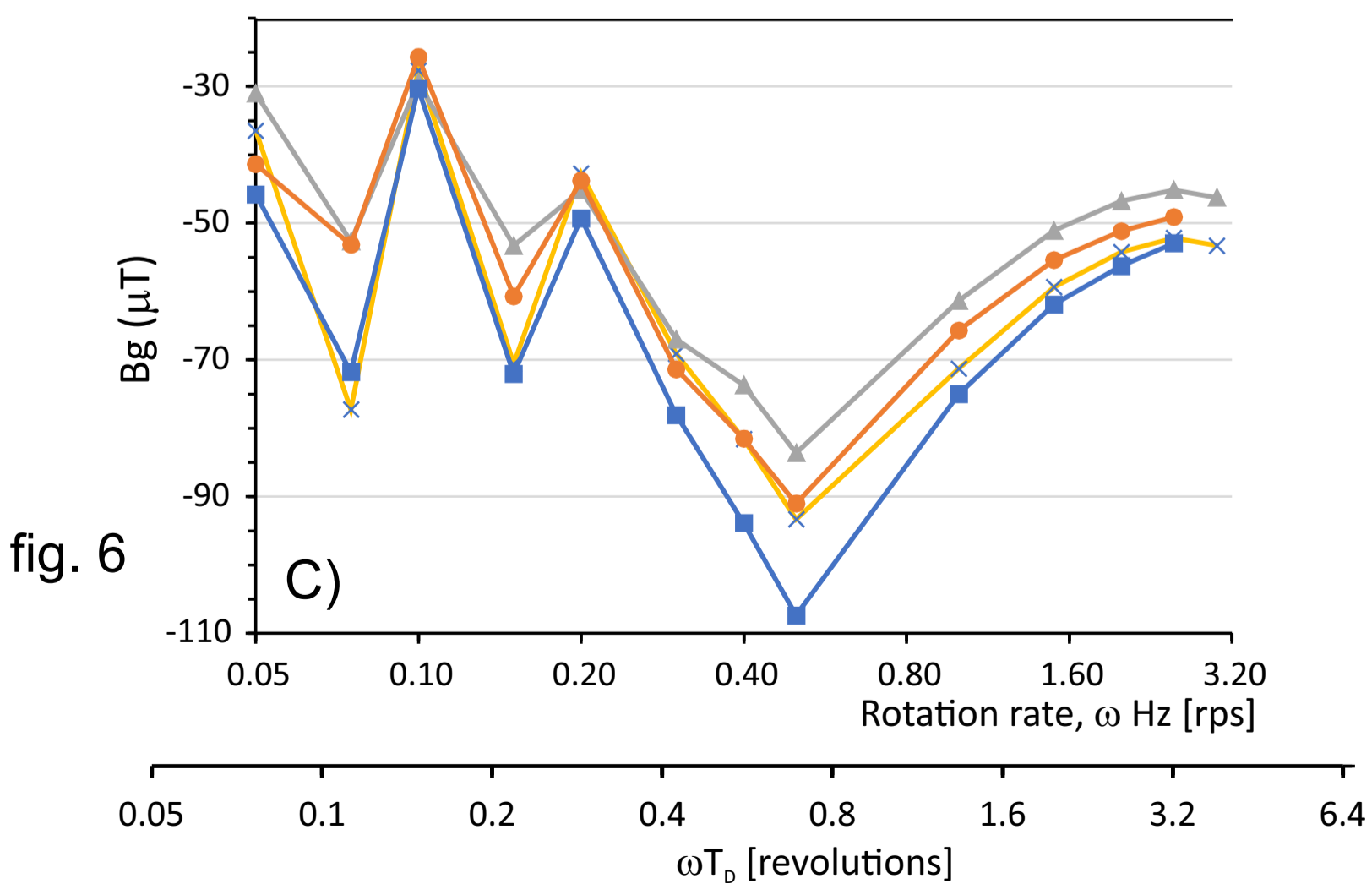
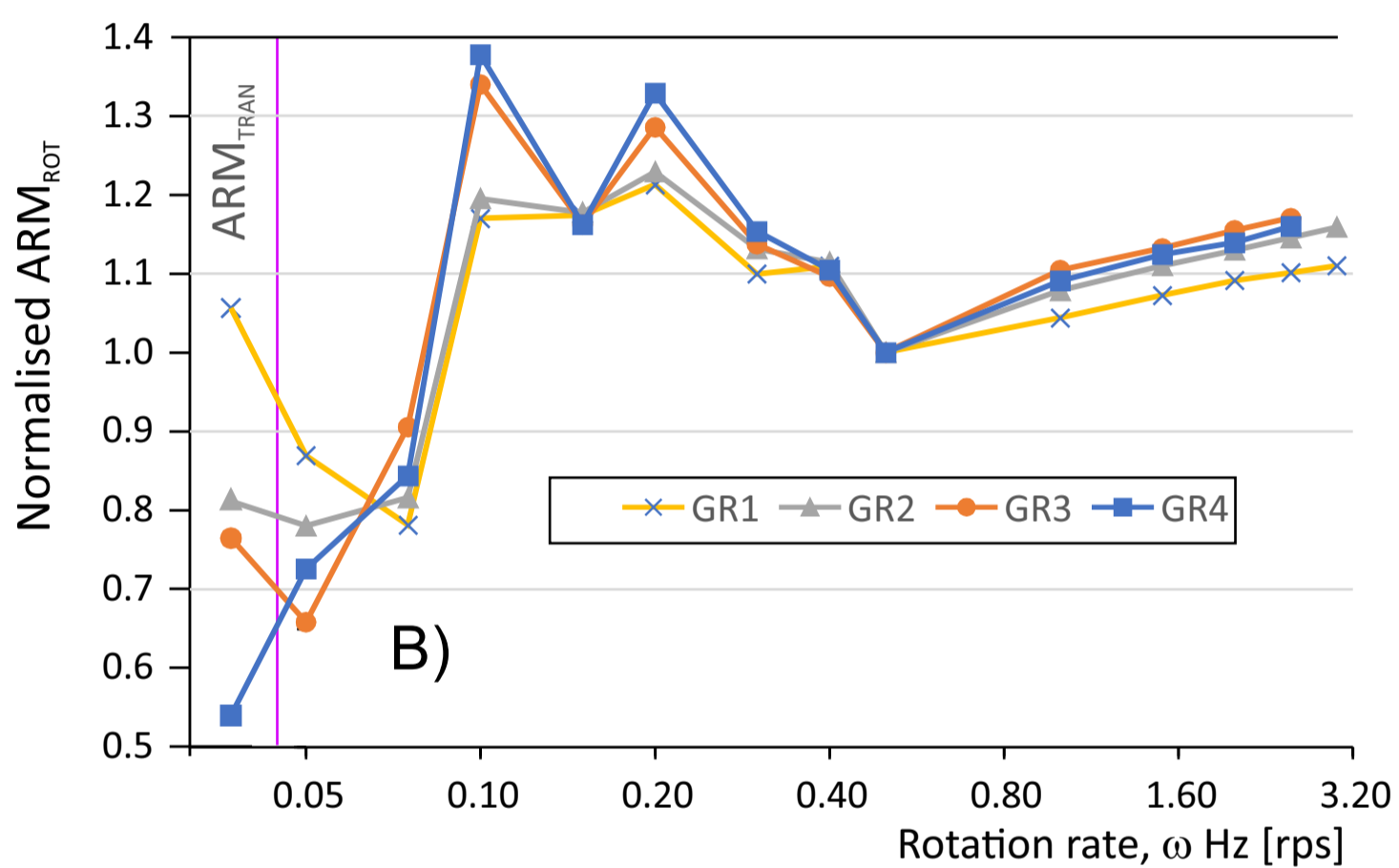
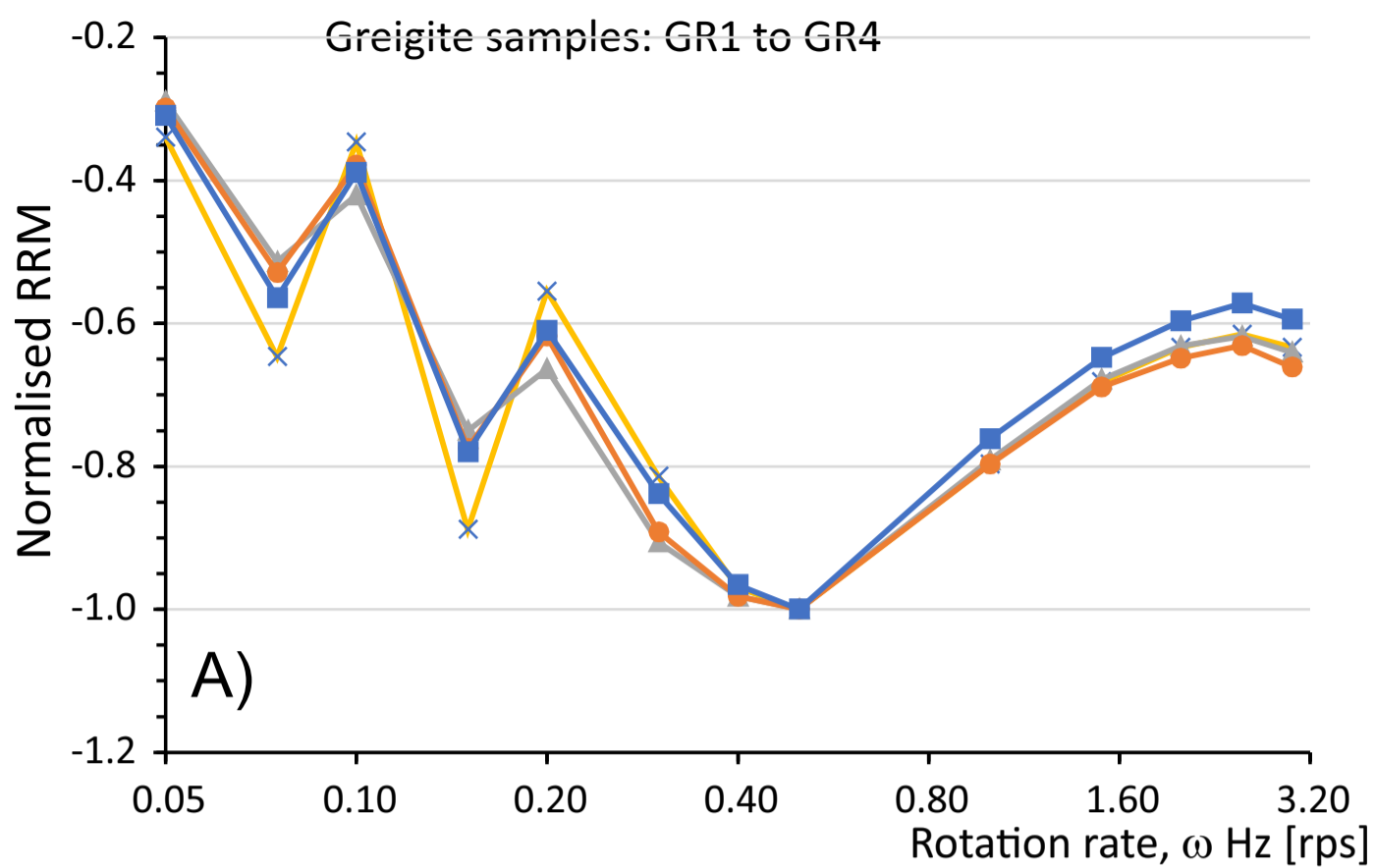


fig. 5



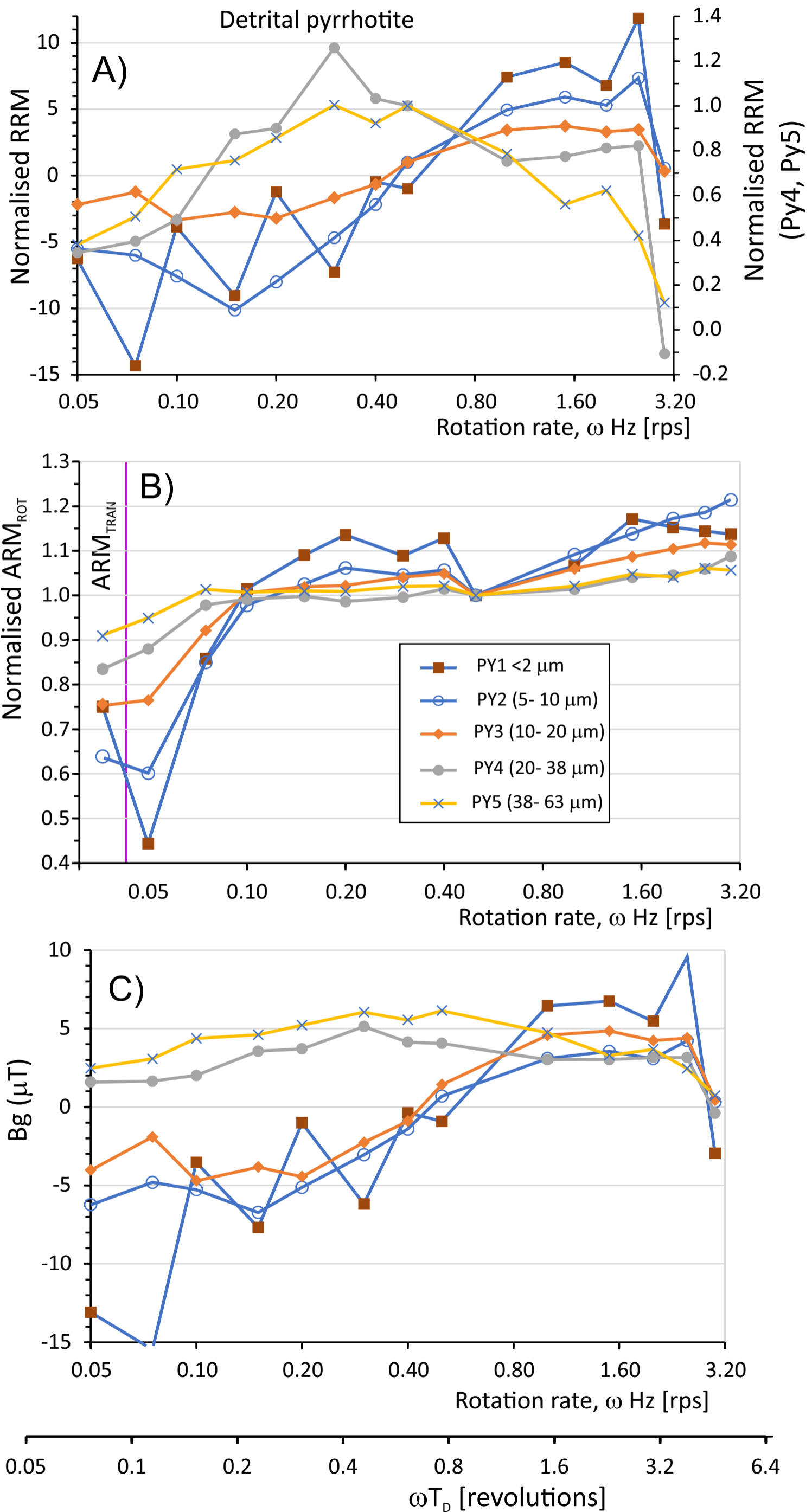


fig. 7

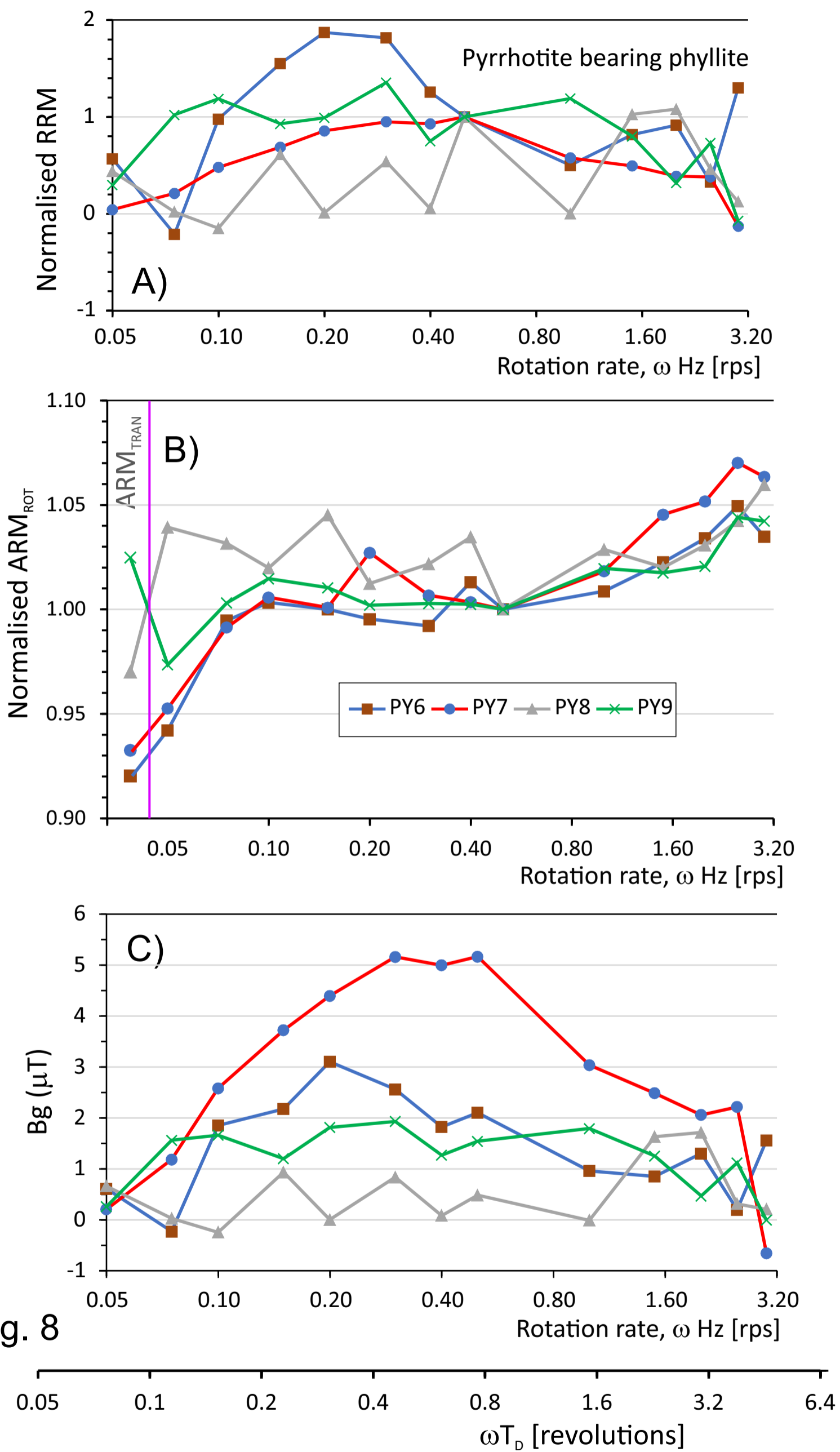


fig. 8

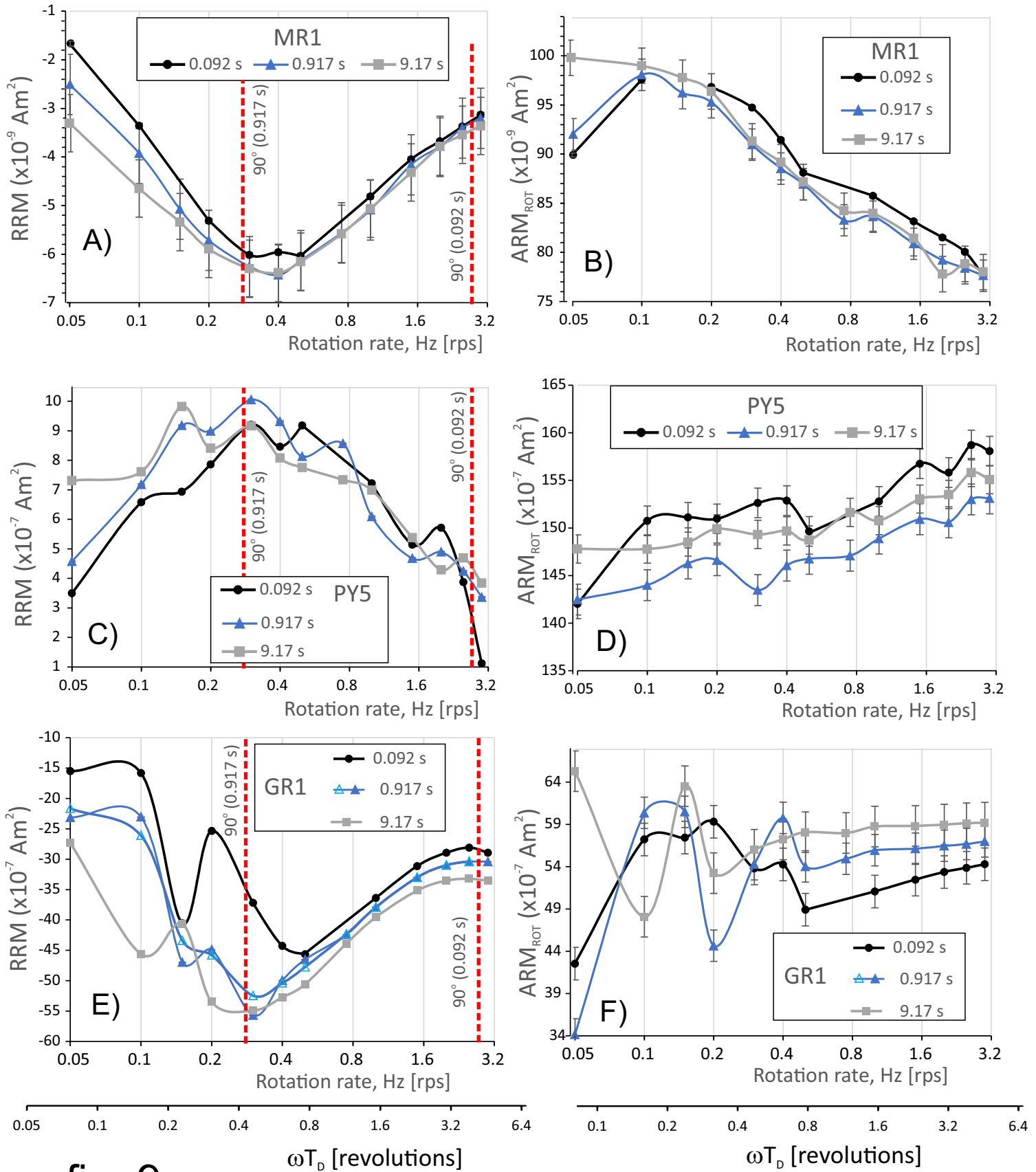


fig. 9

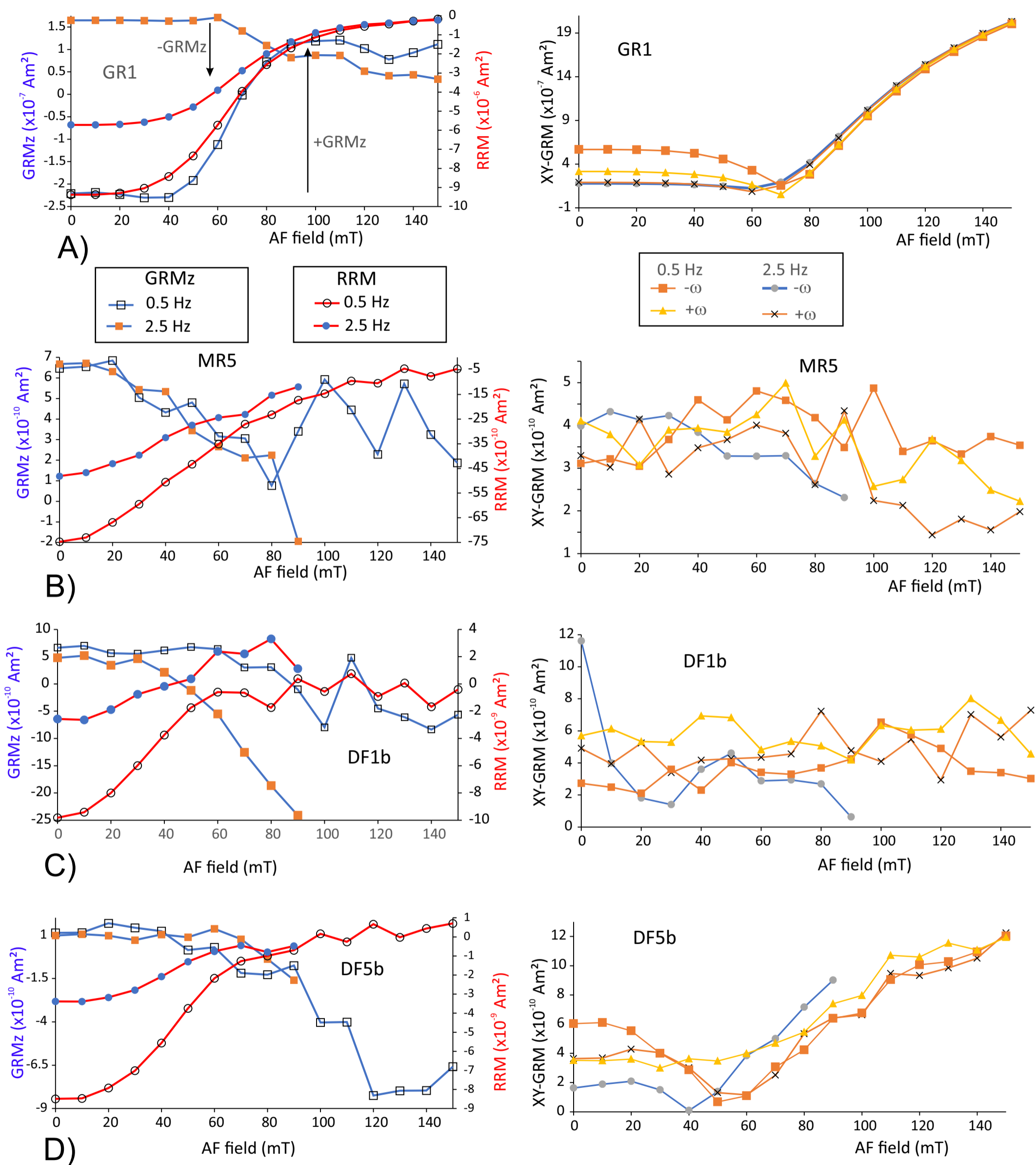


fig. 10

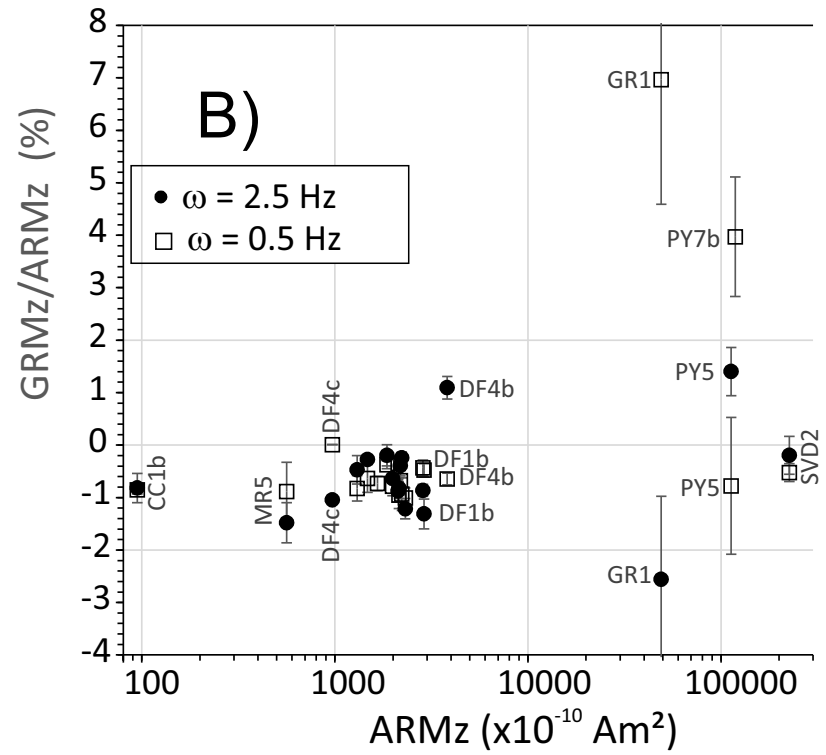
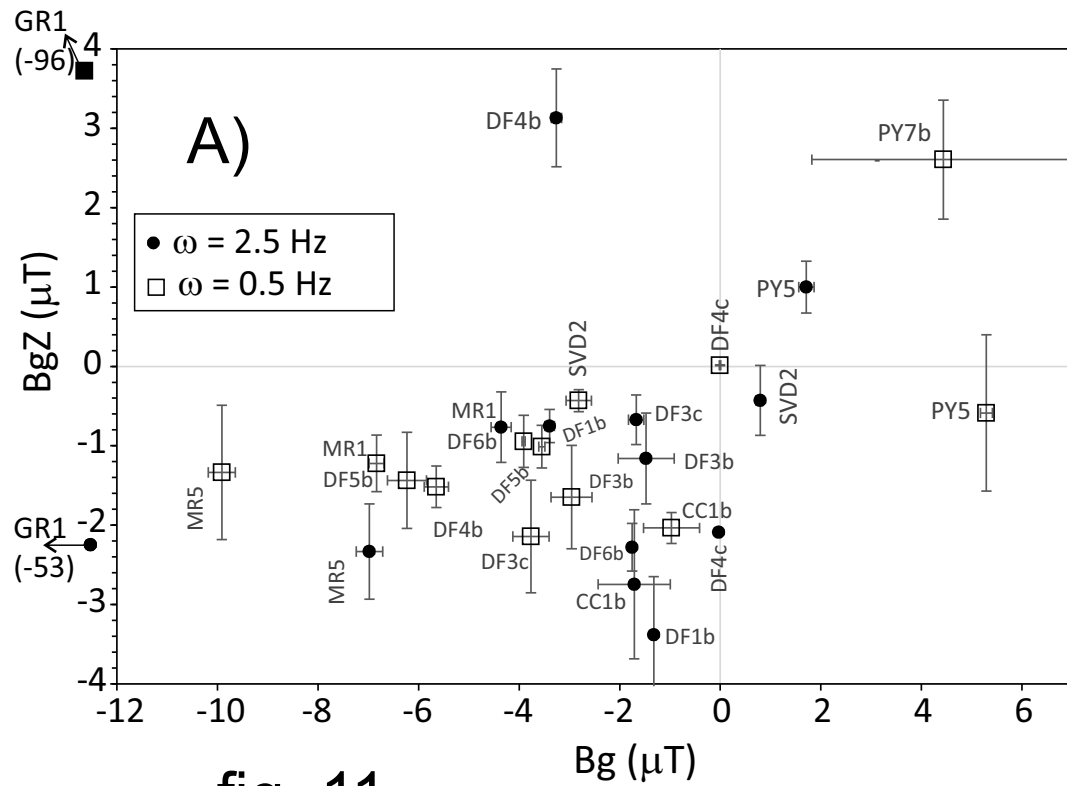
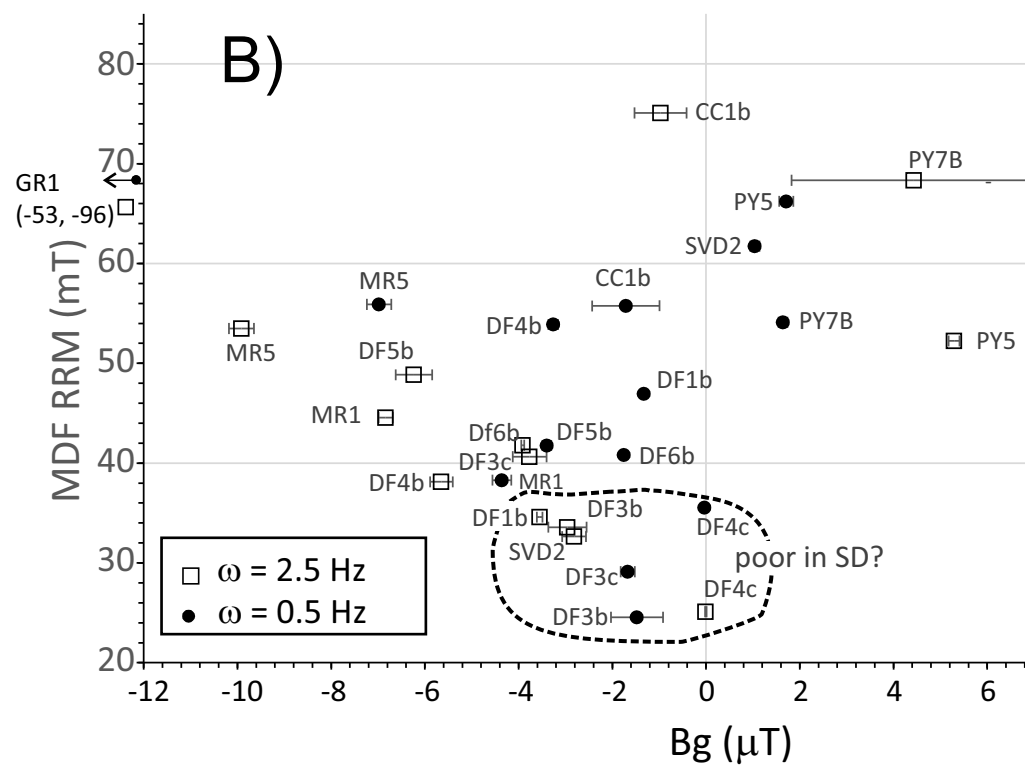
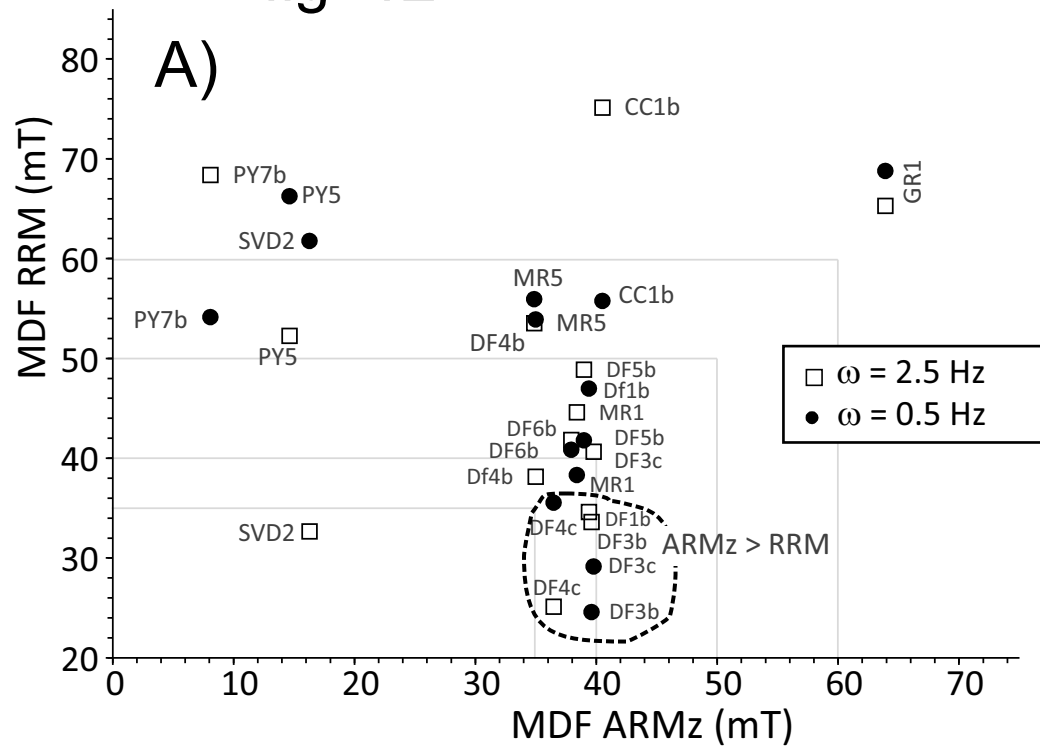


fig. 11

fig. 12



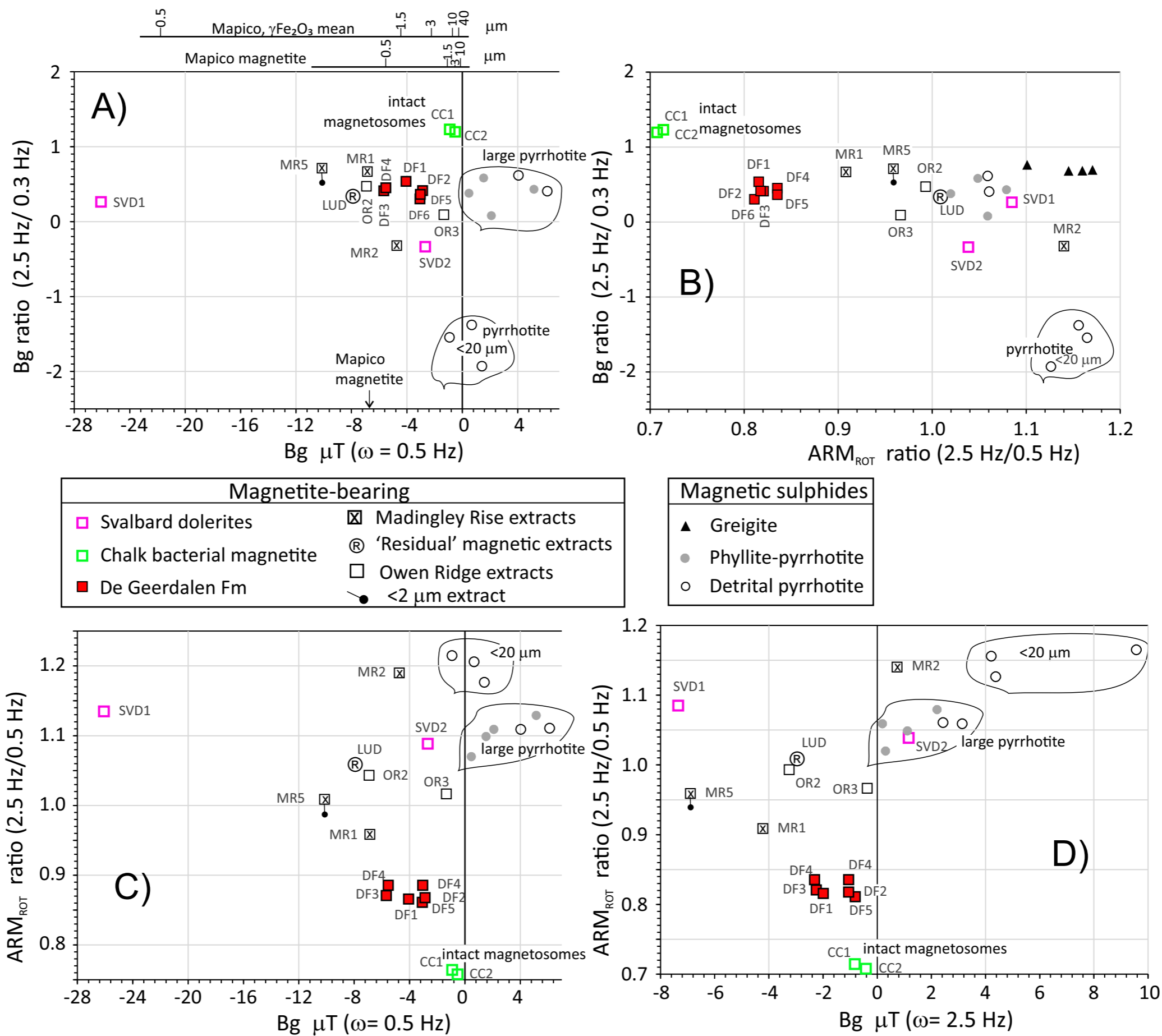


fig. 13

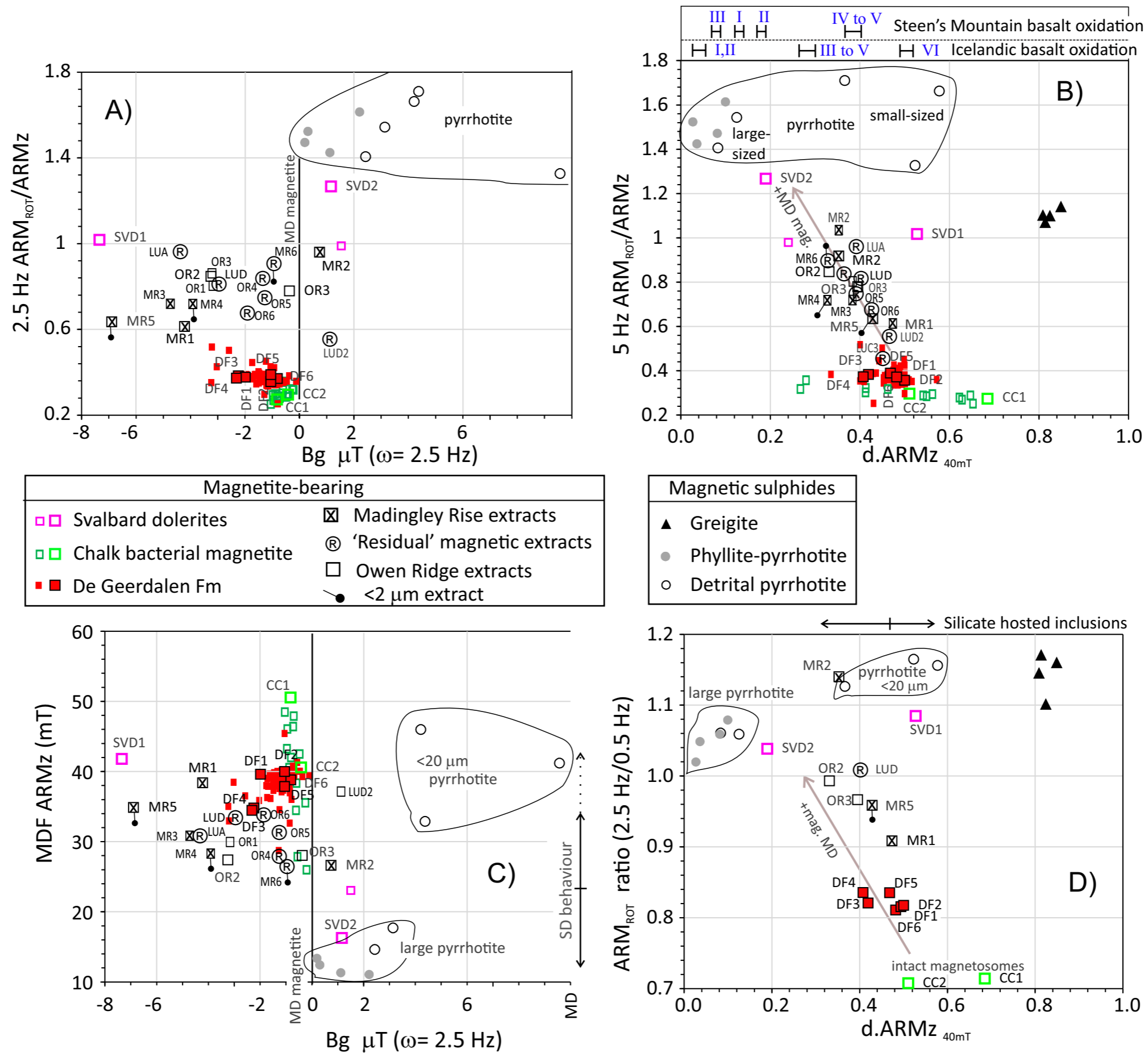


fig. 14

Table 1. Data sources for RRM and ARM_{ROT} versus rotation rates (ω in Hz [rps]). T_D = Alternating field decay time (i.e. demagnetising field time) in secs. ?= value unspecified. *Stephenson & Molyneux (1987) device uses decay rate of $\sim 7 \text{ mT s}^{-1}$ (hold time, $T_H = 5 \text{ s}$), so this is assumed if not given in publication, when this device is used. TM= titanomagnetite.

Mineral/ grain size	AF Hz/mT;	ω range [T_D]	Ref. Fig.	Reference
Crushed magnetite $<0.7 \mu\text{m}$	50/ 40,80	0-180 [~ 10]	fig. 6	Potter & Stephenson 1986
Natural magnetite 13-0.7 μm	50/60	0-200 [~ 10]	fig. 5	Potter & Stephenson 1986
Mapico magnetite (0.2-0.8 μm), Cubical	50/60	0-200 [~ 10]	fig. 5	Potter & Stephenson 1986
Synthetic magnetite	50/50-60	0.01-6 [?]	fig. 3	Wilson & Lomax 1972
2.2-4.4 magnetite	50/80	0-100 [11.4*]	fig. 2	Stephenson & Snowball 2001
Synthetic magnetite (63-125 μm)	63.5,128,603,1210/40-55;	0.003-0.10 [45]	fig. 1	Edwards 1980a
Synthetic magnetite (63-125 μm)	128/55;	0.003-0.40 [6.6,67]	fig. 8	Edwards 1982a,1982b
$\gamma \text{ Fe}_2\text{O}_3$ TDK tape, Type D. elongate	50/60	0-200 [~ 10]	fig. 5	Potter & Stephenson 1986
$\gamma \text{ Fe}_2\text{O}_3$	50/60	0-200 [\sim minutes?]	fig. 3	Madsen 2003
CrO_2	50/65,80,95	0-200 [\sim minutes?]	fig. 3	Madsen 2003
Heated pyrrhotite	50/80	0-130 [11.4*]	fig. 3	Thomson 1990
Various pyrrhotite bearing rocks	?/?	-20 to +20 [?]	fig. 4C	Slotznick et al. 2016
BAM8, BMR7 natural greigite	50/80	0-100 [11.4*]	fig. 3, 4	Stephenson & Snowball 2001
Igneous rock sample A66B1	50/51	0-250 [few secs]	figs 4,5	Stephenson 1980
Icelandic basalts C10-2a, S2-1a	50/80	0.01-60 [?]	fig. 5	Stephenson 1976
Igneous samples (TM bearing)	50/50-60	0.01-6 [?]	fig. 3	Wilson & Lomax 1972
Rock sample R1	63.5,128,603,1210/55	0.003-0.16 [45]	fig. 2	Edwards 1980a
Rock R1, Igneous samples F37B-1a, D264-26 (TM bearing)	128/55	0.003-0.4 [6.6,34,67,101]	figs. 5,6,7	Edwards 1982b, samples from Wilson & Lomax

Table 2. RRM and Bg values measured at spin rates exceeding the AF frequency threshold. Rotation rate, ω , in Hz [rps]. [&] also gives data for AF field down to 20 mT, at approximately linear decrease for all, except for γ Fe₂O₃ TDK tape. * in 10⁻³ A/m, ** in 10⁻⁶ A/m. Negative RRM indicate RRM acquired opposite to rotation vector (Fig. 1). \pm shows SD or uncertainty on Bg averages. Stephenson & Molyneux (1987) device uses decay rate \sim 7 mT/s (5 s hold time), so this is assumed if not given in the publication using this machine. T_D= Alternating field decay time (i.e. demagnetising field) in seconds. ?=decay time unspecified. ^c Chen (2014) inconsistently uses sign on RRM, assume Bg has the correct sign. TM= titanomagnetite.

Mineral/ grain size	AF Hz/mT	ω [T _D], DC Field (μ T)	Bg (μ T)	RRM, ARM _{ROT} ($\times 10^{-3}$ Am ² /kg)	Reference
Crushed magnetite <0.7 μ m	50/ 80	108 [\sim 10],43	108 ^{&}	95,	Potter & Stephenson 1986
Crushed magnetite 0.7-2.2 μ m	50/ 80	108 [\sim 10], 43	44 ^{&}	33,	Potter & Stephenson 1986
Mapico magnetite (0.2-0.8 μ m), Cubical	50/ 80	108 [\sim 10], 43	301 ^{&}	177,	Potter & Stephenson 1986
Crushed magnetite 2.2-4.4 μ m	50/ 80	108 [\sim 10], 43	28 ^{&}	15.5,	Potter & Stephenson 1986
Crushed magnetite 2.2-4.4 μ m	50/80	95 [11.4 [*]], 70	28	10.9,39	Stephenson & Snowball 2001
Crushed magnetite 4.4-7.6 μ m	50/ 80	108 [\sim 10], 43	17.8 ^{&}	9.2,	Potter & Stephenson 1986
Crushed magnetite 7.6-13.1 μ m	50/ 80	108 [\sim 10], 43	8 ^{&}	2.9,	Potter & Stephenson 1986
Crushed magnetite 13.1-25.5 μ m	50/ 80	108 [\sim 10], 43	4.1 ^{&}	1.01,	Potter & Stephenson 1986
SD3 Crushed magnetite	50/95	90 [minutes], 150	330	6.8,18.3 [*]	Madsen 2004
γ Fe ₂ O ₃ TDK tape, Type D. elongate	50/80	108 [\sim 10], 43	161 ^{&}	330,	Potter & Stephenson 1986
γ Fe ₂ O ₃ , BASF FT26 tape	50/95	90 [minutes], 43	85 to 150	167,218	Madsen 2003, 2004
CrO ₂ , BASF CK40-13 tape	50/95	63 [minutes], 70	-15	83.5,7098	Madsen 2003,2004
Natural SD magnetite magnetosomes (water column)	50/80	95[11.4], 70	0	0,-	Chen 2014 ^c
MV-1 magnetite magnetosomes	50/80	95[11.4], 70	1, 10.9	0.105, 0.674 ^{**}	Chen 2014 ^c
SD magnetite and greigite	50/80	95[11.4], 70	2.4, 5.6	0.037,0.461	Chen 2014 ^c
SD greigite magnetosomes	50/80	95[11.4], 70	7.3, 22.5	0.0006, 0.00187	Chen 2014 ^c
Heated (315°C) vein pyrrhotite	50/80	100[11.4-86.4], 70	-	3.3,-	Thomson 1990
Rock and pottery samples below					
DG1 vesicular basalt, Low Ti-TM	50/95	90 [minutes], 150	34	1552,1910 [*]	Madsen 2004
DG17 vesicular basalt, Low Ti-TM	50/95	90 [minutes], 150	26	1014,2384 [*]	Madsen 2004
T97A flood basalt with TM	50/95	65 [minutes], 150	9	327.7,5141 [*]	Madsen 2004
T54A sill, with magnetite	50/95	70 [minutes], 150	38	1368,5824 [*]	Madsen 2004

TC05, TM10, SD TM, Tiva Canyon Tuff	50/80	95[11.4], 70	32	0.804,1.76	Chen 2014 ^c
Supska potsherd	50/80	95[11.4],70	162	-, -	Mahon & Stephenson 1997
Soba potsherds	50/80	95[11.4],70	82 ±16	-, -	Mahon & Stephenson 1997
Baranda potsherds	50/80	95[11.4],70	23	-, -	Mahon & Stephenson 1997
YB7 marine sediment, maghemite	50/95	90 [minutes], 150	89	26.7,41.9*	Madsen 2004
Greigite bearing lake sediments	50/80	95 [11.4],70	482± 221	264,33.1*	Hu et al. 2002
BAM8 natural greigite	50/80	95 [11.4*], 70	1050	998,95	Stephenson & Snowball 2001
BMR7 natural greigite	50/80	95 [11.4*], 70	1070	375,35	Stephenson & Snowball 2001
SD greigite, Gutingkeng Fm (EJC49.1c, EJC50.1c)	50/80	95[11.4], 70	552-790	0.201,0.0210	Chen 2014 ^c

Table 3. RRM and Bg values measured at spin rates below the AF frequency threshold. Rotation rate, ω , in Hz [rps]. ^{AR}= partial rotational ARM (static sample during AF decay). See caption to Table 2 for details.

Mineral/ grain size	AF Hz/mT	ω [T _D], DC Field (μ T)	Bg (μ T)	RRM, ARM _{rot} ($\times 10^{-3}$ Am ² /kg)	Reference
Low spin rate data					
γ Fe ₂ O ₃ Sony MC30	50/100	5 [?], 100	-5.5 ^{Ss}	-, -	Snowball 1997b
γ Fe ₂ O ₃ TDKD1	50/100	5 [?], 100	-8.0 ^S	-, -	Snowball 1997b
γ Fe ₂ O ₃ TDKD2	50/100	5 [?], 100	-7.1 ^S	-, -	Snowball 1997b
MCF0-1, Co- γ Fe ₂ O ₃	128/46	0.07 [15], 60	-37	-,12 ^{AR}	Edwards & Desta 1989
GFO-1, γ Fe ₂ O ₃	128/46	0.07 [15], 60	-30	-,31 ^{AR}	Edwards & Desta 1989
MBL-1, Mapico Black magnetite	128/46	0.07 [15], 60	-8	-,9.7 ^{AR}	Edwards & Desta 1989
Magnetite (63-125 μ m), Mag6	128/18.4	0.4 [17], 60	-3	-,2.13 ^{AR}	Edwards & Desta 1989
MDM- MD detrital magnetite	50/100	5 [?], 100	0 ^S	-, -	Snowball 1997b
CRO-1 CrO ₂ powder	128/46	0.07 [15], 60	-5	-,2.0 ^{AR}	Edwards & Desta 1989
CrO ₂ TDKMF1	50/100	5 [?], 100	-31 ^S	-, -	Snowball 1997b
Rock R1-a	128/36.4	0.4 [17], 45	-15	-,0.21 ^{AR}	Edwards & Desta 1989
D264-2a (TM bearing)	128/36.4	0.4 [17], 60	0	-,0.12 ^{AR}	Edwards & Desta 1989

Carboniferous Lavas	800/150	1 [30], 15	-3.1 ±1.9 ^S	-260,1350*	Roperch & Taylor 1986
Miocene Basalt (with -RRM)	800/150	1 [30], 15	-13.6 ±16.7 ^S	-1200,1850*	Roperch & Taylor 1986
Miocene Basalt (with +RRM)	800/150	1 [30], 15	8.9±1.2 ^S	1120,1910*	Roperch & Taylor 1986
Pliocene Basalt	800/150	1 [30], 15	-5.6 ±1.2 ^S	-290,780*	Roperch & Taylor 1986
Serpentinite	800/150	1 [30], 15	-3.8±4.8 ^S	-50,200*	Roperch & Taylor 1986
Pajep8- SD magnetite magnetofossils+detrital	50/100	5 [52?], 100	-0.14 ^S	-, -	Snowball 1997b
Hol81- SD detrital magnetite	50/100	5 [52?], 100	-14 ^S	-, -	Snowball 1997b
Hol252- SD detrital magnetite	50/100	5 [52?], 100	-3.6 ^S	-, -	Snowball 1997b
Embmr1-SD greigite sediment	50/100	5 [52?], 100	-98 ^S	-, -	Snowball 1997b
Embmr5-SD greigite sediment	50/100	5 [52?], 100	-110 ^S	-, -	Snowball 1997b
Embmr6-SD greigite sediment	50/100	5 [52?], 100	-84 ^S	-, -	Snowball 1997b
Embmr8-SD greigite sediment	50/100	5 [52?], 100	-101 ^S	-, -	Snowball 1997b
Bmr9x-SD greigite concentrate	50/100	5 [52?], 100	-108 ^S	-, -	Snowball 1997b
St15-SD greigite sediment	50/100	5 [52?], 100	-119 ^S	-, -	Snowball 1997b
St79x-SD greigite concentrate	50/100	5 [52?], 100	-137 ^S	-, -	Snowball 1997b
Heated (315°C) pyrrhotite	50/80	~5 [11.4-86.4], 70	-	1.9,-	Thomson 1990

Table 4. The test samples used in this work. SD=single domain, MD=multidomain. T_c= Curie temperature; TM= titanomagnetite, Ti content (wt%). See the SI for further details about these test samples.

Sample codes	Description	Mineralogy	References
PY1	< 5 μm magnetic separate from river sediment, Taiwan	Monoclinic pyrrhotite	Horng & Roberts 2006.
PY2	5-10 μm magnetic separate from river sediment, Taiwan	Monoclinic pyrrhotite	Horng & Roberts 2006.
PY3	10-20 μm magnetic separate from river sediment, Taiwan	Monoclinic pyrrhotite	Horng & Roberts 2006.
PY4	20-38 μm magnetic separate from river sediment, Taiwan	Monoclinic pyrrhotite, quartz, goethite	Horng & Roberts 2006.

PY5	38-63 μm magnetic separate from river sediment, Taiwan	Monoclinic pyrrhotite, quartz, goethite, lepidocrocite, chlorite	Horng & Roberts 2006.
PY6-PY9	Monoclinic pyrrhotite bearing phyllites from Taiwan metamorphic Central Range	Monoclinic pyrrhotite	Horng et al. 2012,
GR1-GR4	Greigite bearing mudstones, Plio-Pleistocene Lower Gutingkeng Formation, SW Taiwan	Fine-grained greigite	Horng et al. 1998; Jiang et al. 2001.
LUA-LUD	<38 μm magnetic extract from Late Triassic Lunde Fm, N. Sea.	Mn and Cr-bearing magnetites, chromite, (magnetite) oxide inclusions in various silicates.	Hounslow et al. 1995; Hounslow 1996
LUD2, LUD3	38-63 μm and 63-250 μm magnetic extract from Late Triassic Lunde Fm, N. Sea	Dominated by Fe-oxide (magnetite) inclusions in silicates, lesser chromite and Mn-magnetite.	Hounslow et al. 1995; Hounslow 1996.
OR1, OR2	<38 μm Magnetic extract from 0.35 m, 1.25 m depth in IODP 722B, Indian Ocean, Owen Ridge	Magnetite as mixed detrital and very minor bacterial magnetite. Fe-oxide inclusions in various silicates (probably minor contribution)	Hounslow & Maher, 1996; 1999
OR3	<38 μm Magnetic extract from 7.8 m, depth in IODP 722B, Indian Ocean, Owen Ridge	Detrital magnetite. Fe-oxide inclusions in various silicates, ilmenite.	Hounslow & Maher, 1996; 1999
OR4, OR5, OR6	<38 μm Magnetic extract from 38.6m, 40.6 m, 60-62 m in IODP 722B, Indian Ocean, Owen Ridge	Residual assemblage of detrital magnetite, ilmenite and major Fe-oxide inclusions in various silicates.	Hounslow & Maher, 1996; 1999
MR1	<38 μm Magnetic extract from 118-120 m in IODP Site 709A, Madingly Rise, Indian Ocean (oxic interval)	Magnetite as mixed detrital and important bacterial magnetite.	Hounslow & Maher, 1996; 1999
MR2, MR3	<38 μm Magnetic extract from 112.9 m and 28-29.7 m in IODP Site 709A, Madingly Rise, Indian Ocean (reduced interval)	Magnetite as mixed detrital and less important bacterial magnetite.	Hounslow & Maher, 1996; 1999
MR4	<~2 μm Magnetic extract from 5.89-8.41 m and IODP Site 709A, sample levels with SIRM/ χ ARM >390 Am^{-1} . E_{mpt} extract.	Major bacterial magnetite with similar content of fine detrital magnetite	Maher & Hounslow 1999, unpubli. data

MR5	<~2 μm magnetic extract from 22.8-23.5m in IODP site 709C, Madingly Rise, Indian Ocean. E_{mpt} extract.	Minor bacterial magnetite with larger content of fine detrital magnetite	Maher & Hounslow 1999, unpubl. data
MR6	<~2 μm magnetic extract from 45.8-47.3 m in IODP site 709C, Madingly Rise, Indian Ocean. E_{mpt} extract (sulphide-reduced interval)	Residual assemblage of detrital magnetite, ilmenite, and major Fe-oxide inclusions in various silicates.	Maher & Hounslow 1999; unpubl. data
CC1, CC2	Whole rock Upper Cretaceous Chalk from the level of WC9b at Culver Cliff, Isle of Wight, UK.	Rich in bacterial magnetite in chains, no detrital oxides, but common Fe-oxides as inclusions in silicates.	Montgomery et al. 1998; Kopp & Kirschvink 2008
SVD1, SVD2	Fine-grained dolerites from the Diasbasoddon suite of the High Arctic province, sills near lower contacts at Botneheia, Svalbard	TM (20-31)–ilmenite intergrowths, altered to maghemite at margins. 1–500 μm in size; Low alteration, SD–MD behaviour. Maybe minor pyrrhotite. T_c 520-550°C	Halvorsen, 1973; Vincenz et al. 1984; Nejbort et al. 2011.
DF1 to DF6	Sandstones, siltstones, De Geerdalen Fm, Svalbard. DF1, DF2 from central Spitsbergen, DF3, DF4 from Hopen, DF5, DF6 from E. Svalbard.	Detrital magnetite, T_c ~450-600°C, in part oxidized, possibly wide range of grain sizes.	Hounslow et al. 2007; 2022.

Supplementary information for: Rotational remanent magnetisation as a magnetic mineral diagnostic tool at low rotation rates

Mark W Hounslow^{1,2}, Chong-Shern Horng³ & Vassil Karloukovski¹

¹. Lancaster Environment Centre, Lancaster University, Lancaster, UK.

(mark.w.hounslow@gmail.com, correspondence author), (v.karloukovski@lancaster.ac.uk)

². Earth, Ocean and Ecological Sciences, Univ. of Liverpool, Jane Herdman Building, Liverpool, UK.

³. Institute of Earth Sciences, Academia Sinica, PO Box 1-55, Nankang, Taipei 11529, Taiwan.

(cshorng@earth.sinica.edu.tw).

The supplementary information consists of:

- Section 1- Additional magnetic and mineralogical information about the test samples
- Section 2- Additional information about measurement uncertainty on the RAPID.
- Section 3- Additional characteristics of RRM-related magnetisations
- Section 4- An evaluation of AF hold times and AF frequency on the RAPID
- Associated excel file which contains the data used in this study.

1. Further details about the test samples used in this study

1.1 Rock test samples

The sized pyrrhotite samples are dominated by monoclinic pyrrhotite, with the coarser samples like PY5 having a little quartz and chlorite (probably with associated Fe-oxide inclusions) and small amounts of goethite and lepidocrocite (probably from minor pyrrhotite oxidation, Figs. S1, S2, Table S1).

The Chalk test sample (Campanian in age) come from the CC9b horizon at Culver Cliff (Isle of Wight, UK), sampled across the foreshore within the same horizon (ca. ± 10 cm error). This bed has locally the highest concentration of bacterial magnetofossils from several Chalk samples tested (unpublished data of Hounslow). A magnetic extract from this bed is figured in Chalk sample data (sample Chalk B) shown in Hounslow & Maher (1996, fig. 7a, 10), Montgomery et al. (1998, plate 1, sample WC9b), Maher et al. (1999, plate 1.10, 1.11), Hounslow & Maher (1999a, fig. 9.9c) and Kopp & Kirschvink (2008, fig 6c-d). The XRD of the E_{MP} type extract is in Fig. S5a. The E_{mpt} type magnetic extract from CC9b contains >95% magnetofossils representing the electron dense material in TEM images with an estimated 80% of these in chains. The ARMz extraction efficiency from the sample is around 94% (Hounslow & Maher, 1996). Magnetofossils are dominantly of prismatic type with a modal size of 65 nm and modal aspect ratio of 0.63 (Fig. S3, S4b), which fall into the single domain particle size (Fig. S4a). The Chalk samples contain few detrital Fe-oxide particles (detritals are largely as inclusions in silicates) either in the E_{mpt} or E_{mp} extracts, being dominated by a residual Ti-oxide assemblage (Fig. S5a). Using the sample Chalk-A (devoid of magnetofossils, Hounslow & Maher, 1996) for comparison, silicate hosted inclusions + residual discrete detritals may contribute something like 5% of the ARMz in the CC9b-level samples.

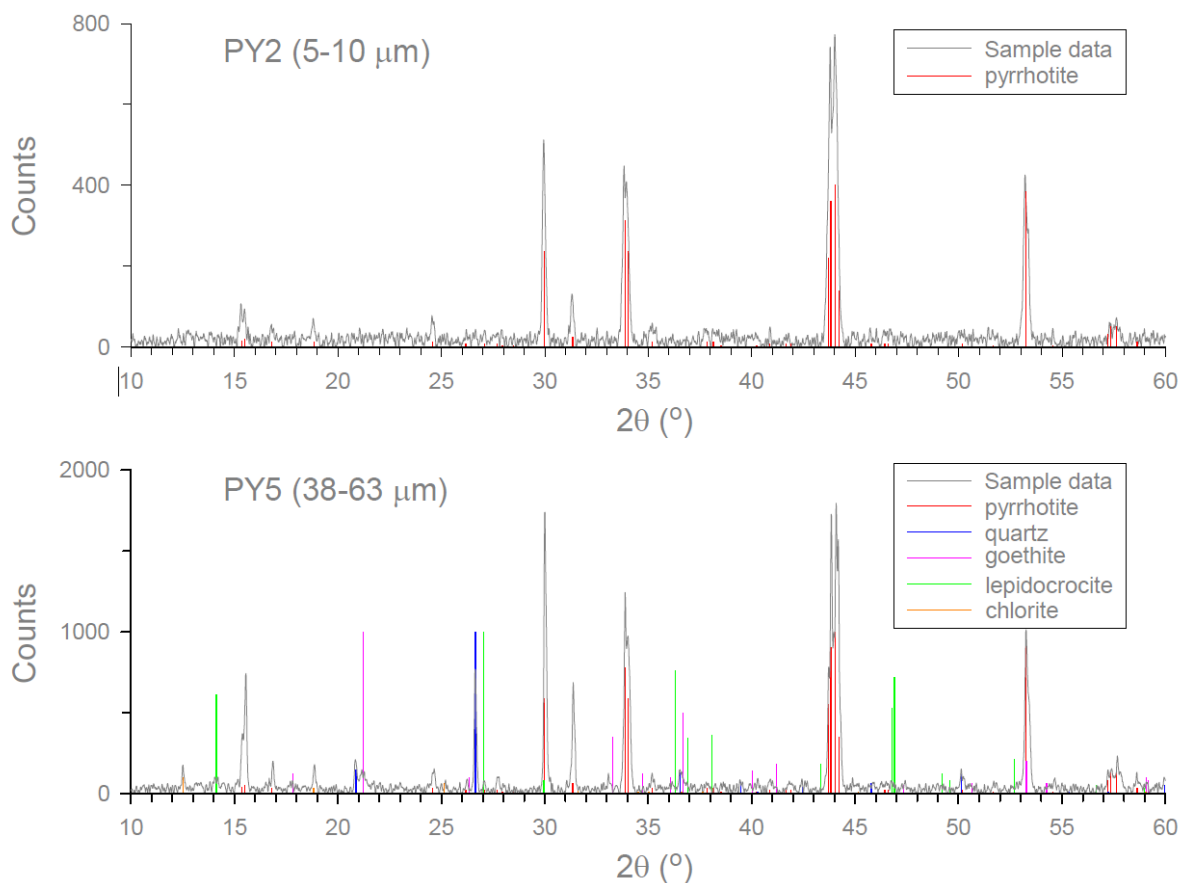


Fig. S1 (above). Representative XRD data for the sized natural pyrrhotite samples (5-10 μm and 38-63 μm , respectively) separated from river sediment by using magnetic extraction. Reference XRD minerals were identified using the powder diffraction file (PDF) from the International Centre for Diffraction Data. Minerals with PDF numbers (#) are as follows: monoclinic pyrrhotite (#29-723), quartz (#79-1906), goethite (#29-713), lepidocrocite (#44-1415), and chlorite (#29-701).

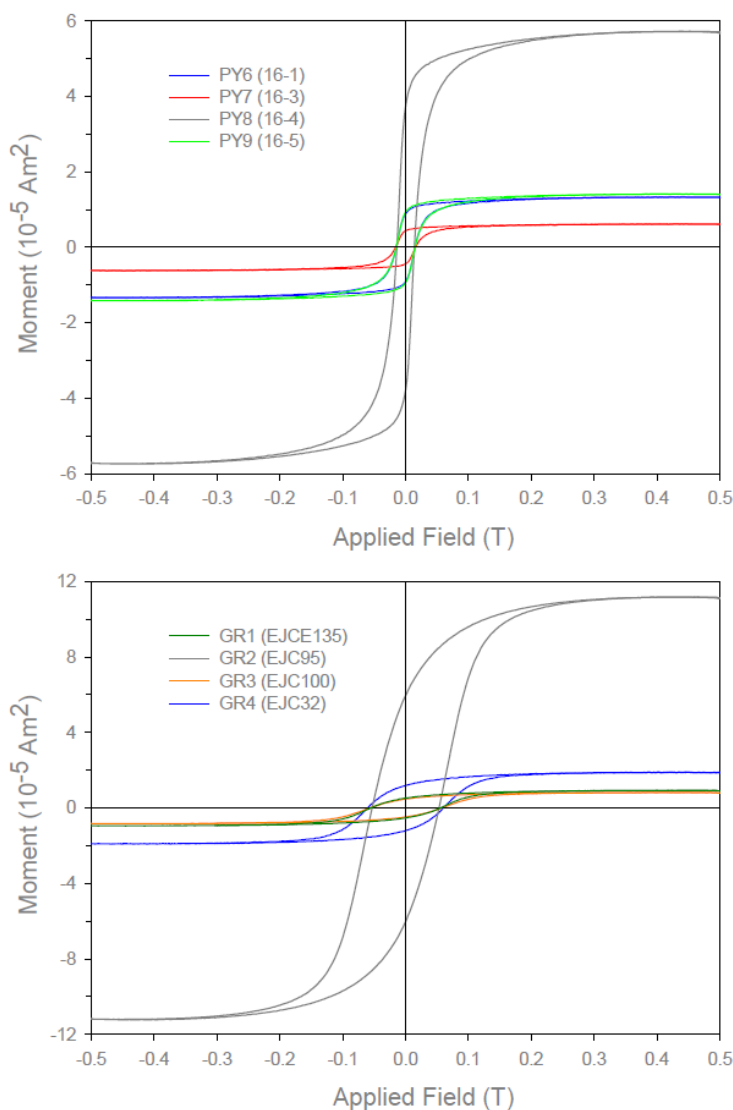


Fig. S2 (left). Magnetic hysteresis loops after slope correction for a) (top) pyrrhotite-bearing and b) (bottom) greigite-bearing test samples. Hysteresis parameters M_s , M_{rs} , B_c , and B_{cr} are shown in Table S1.

Table S1. Hysteresis parameters (after paramagnetic slope correction) for the pyrrhotite-bearing (PY6-PY9) and greigite-bearing (GR1-GR4) test samples. The original specimen codes are shown in brackets.

Sample	Weight (mg)	Hc (mT)	Hcr (mT)	Ms (Am ²)	Mr (Am ²)	Hcr/Hc	Mr/Ms
PY6 (16-1)	227.6	15.07	16.69	1.33E-05	8.99E-06	1.11	0.68
PY7 (16-3)	202.0	15.86	17.38	6.11E-06	4.37E-06	1.10	0.72
PY8 (16-4)	227.1	14.00	15.73	5.71E-05	3.76E-05	1.12	0.66
PY9 (16-5)	214.8	15.01	16.69	1.41E-05	9.36E-06	1.11	0.67
GR1 (EJCE135)	801.3	55.76	73.60	9.27E-06	5.25E-06	1.32	0.57
GR2 (EJC95)	752.8	53.31	73.92	1.12E-04	5.99E-05	1.39	0.54
GR3 (EJCE100)	596.2	57.19	79.28	8.19E-06	4.75E-06	1.39	0.58
GR4 (EJC32)	684.4	60.40	76.40	1.88E-05	1.19E-05	1.26	0.63

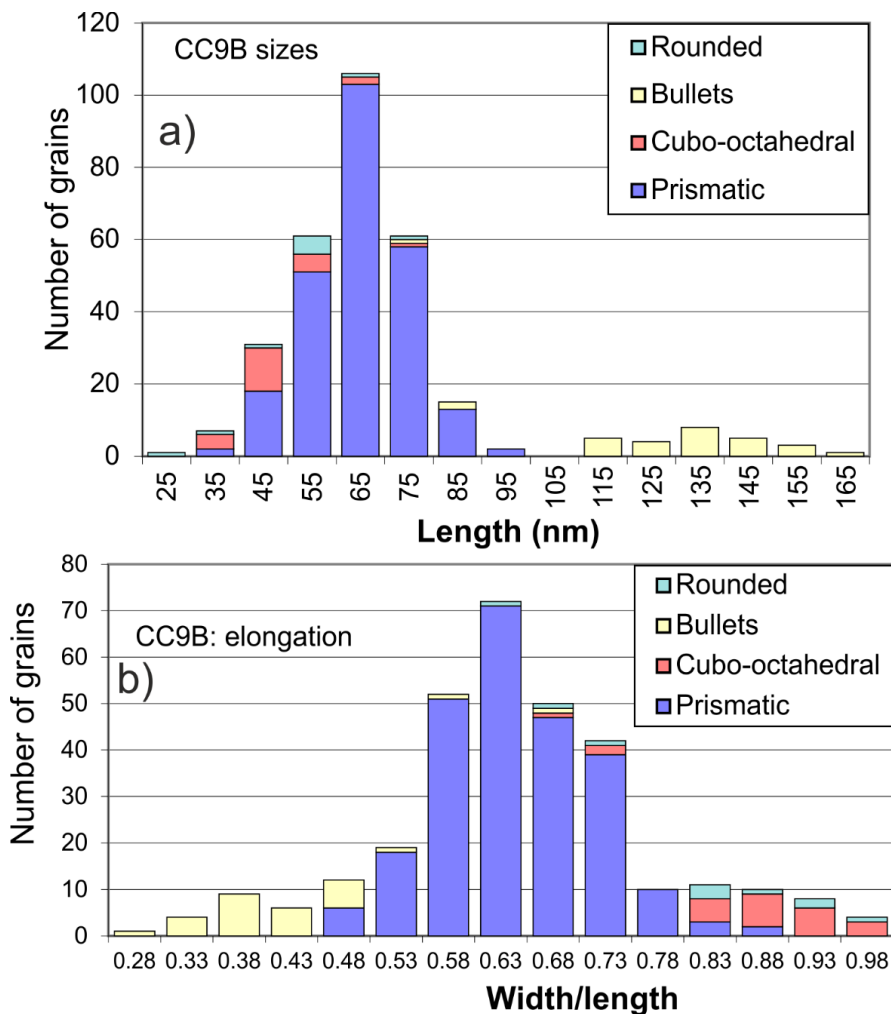


Fig. S3. Magnetofossil morphology and sizes in the E_{mpt} extract from Chalk sample CC9b. A) The length and type of the magnetofossils. B) The width and length ratio versus magnetofossil morphology. The number on each of the bars represents the mid-point of the class, so for example modal column labelled length 65 nm in a) are those between 60 to 69 nm in size etc.

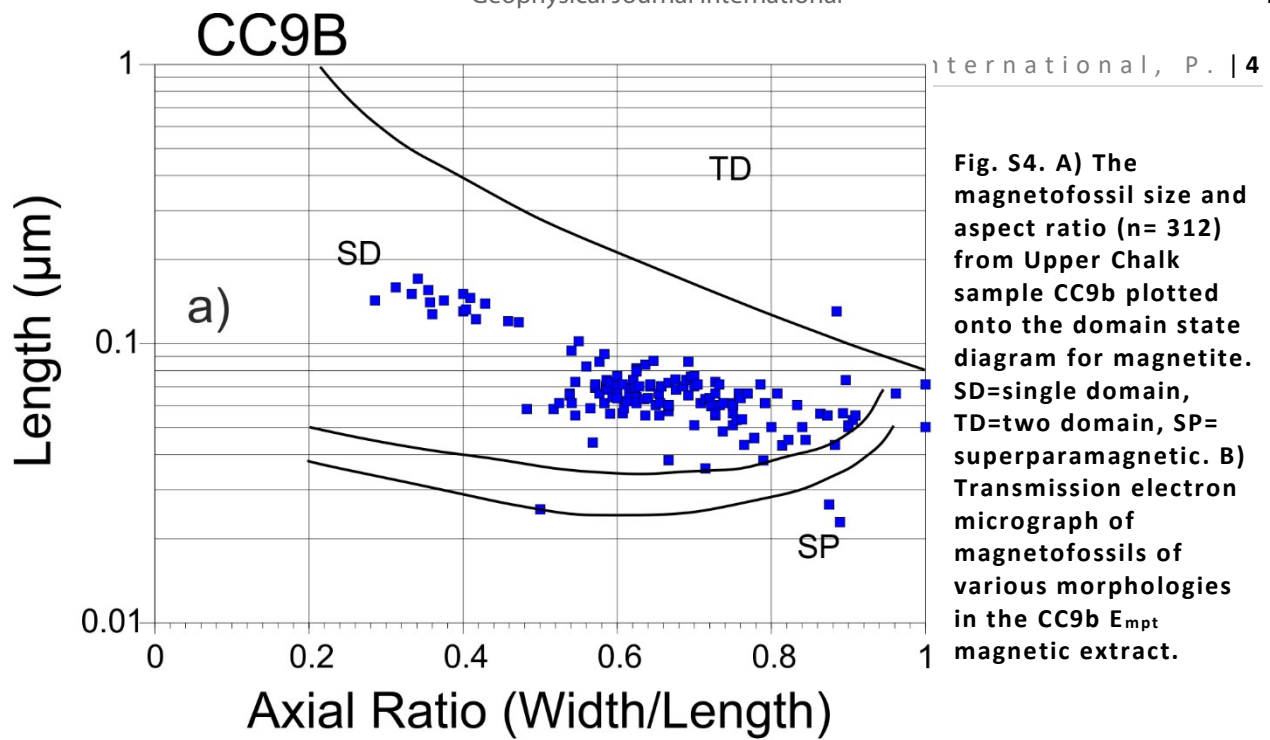


Fig. S4. A) The magnetofossil size and aspect ratio ($n=312$) from Upper Chalk sample CC9b plotted onto the domain state diagram for magnetite. SD=single domain, TD=two domain, SP=superparamagnetic. B) Transmission electron micrograph of magnetofossils of various morphologies in the CC9b E_{mpt} magnetic extract.

1.2 Magnetic extracts

Further magnetic-related and mineralogical details about the magnetic extracts used here are detailed in Tables S2 and S3. These are taken in part from Hounslow & Maher (1996, table 3), Hounslow et al. (1995, tables 2, 3) and Hounslow & Maher (1999b, table 1, fig 12). The relationship of the simplified sample codes used here and those used in the original publications are shown in Table S4. The variation of magnetic susceptibility at low temperatures (Fig. S6) suggests the extracts may be largely dominated by oxidized forms of Fe_3O_4 , due to suppression of the Verwey transition (Özdemir & Dunlop, 2010). However, this behaviour may also be due to minor Ti-substitution, so an alternative interpretation is that the lack of the Verwey transition is related to the lack of substitution-free magnetite and the dominance of Ti-substituted magnetites (Özdemir & Dunlop, 2010). The XRD-derived cell edge spacing suggests the Ti-magnetite oxidation parameter z ranges from around 0.3 (sample OR2) to around 0.8 (sample OR5) (Table S3)- this assumes the Ti-content is near zero using the data of Readman & O'Reilly (1972). If the Ti content is not minor the cell edge spacing suggests rather more oxidized Ti-magnetites ($z > 0.7$). For the Lunde magnetic extracts some

data collected from thermal demagnetisation of ARMz and IRM indicates that the blocking temperatures of the remanence carrying phase has a broad range of temperatures, with this phase having maximum blocking temperatures at around that of the magnetite Curie temperature (Figs. S6, S7). The broad range of blocking temperatures may be representative of the range of the complex Mn, Ti and Cr substitution in the ferrimagnetic phases in these samples (Hounslow, 1996).

The LUD3 magnetic extract is representative of the magnetic behaviour of the inclusions in the silicates in the Lunde samples, which apart from the Mn-Ti-Cr-Fe oxides in the samples (Fig. S9a-c) are the second main ferrimagnetic source in these samples (Fig. S9d). This inference is based on the observation that the >63 μm fraction has few discrete detrital magnetic oxides. The average SIRM of Fe-oxide inclusions in sediments sourced from various basement terrains (excluding Lewisian gneisses) and sediments in the UK is $6 \pm 3.3 \times 10^{-5} \text{ Am}^2/\text{Kg}$ (from Hounslow & Morton, 2004)– which agrees broadly with the data from LUD3 (Table S2). An upper range for the magnetic concentration of inclusions in silicates is probably the sand sourced from Lewisian gneisses which have an inclusion-related SIRM of $45\text{--}60 \times 10^{-5} \text{ Am}^2/\text{Kg}$ (Hounslow & Morton, 2004) which is within the SIRM range seen in the reduced intervals in ODP holes 722B (sample OR4, OR5, OR6) and 709 (MR6) (Tables S2 and S4)– although like the Lunde samples these ODP core intervals contain residual discrete Fe-T oxides. The pyrite in some ODP core extracts (Table S3) is associated with the diagenetic pyritization of the Fe-oxides, seen in the Owen Ridge extracts (OR4, OR5 and OR6). However, the impact of sulphate-reduction on the Madingley Rise sediments (extracts MR2, MR3) has not generated pyrite associated with the Fe-Ti oxides (Table S2).

The non-reduced intervals in the ODP cores are represented by extracts OR1, OR2, MR1, MR4, MR5, which have a complex assemblage of largely Fe-Ti oxides as discrete detrital phases (Fig. S9e-g), plus small amounts of bacterial magnetite, largely not in chains (see fig 7b in Hounslow & Maher, 1996; fig. 3 in Maher & Hounslow, 1999), plus Fe-oxide inclusions in many types of silicates, but especially quartz (see fig. 12 in Hounslow & Maher, 1996) and feldspar (Figs. S9f, S5c-d). The silicate-hosted Fe-oxide inclusions largely account for the large contents of quartz and feldspar in the magnetic extracts seen in XRD (Fig. S5) and the many types of minor accessory minerals seen in optical microscopy (Table S3).

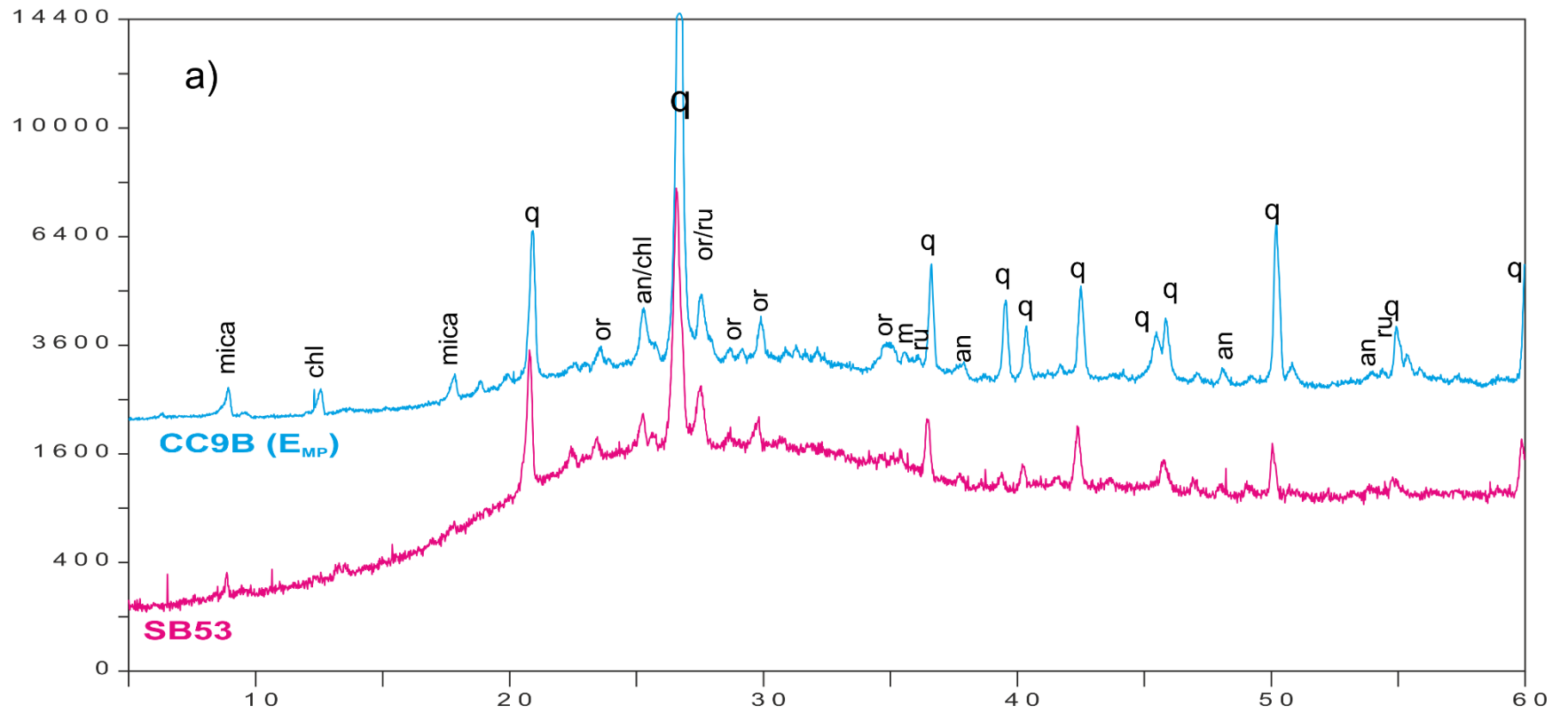
All the magnetic extracts from the Madingley Rise samples contain ‘biogenic’ baryte (see Martinez-Ruiz et al. 2019 for review), largely as $0.5\text{--}10 \mu\text{m}$ ellipsoidal grains (Fig. S8h-l; Fig. S5e-f). It is inferred that these baryte grains contain small amounts of dispersed nanoscale magnetic inclusions. Optical microscopy failed to find any opaque inclusions in these and EDS in TEM and SEM only detected Ba and occasional Sr in these particles; and they are too rounded and electron dense in TEM to see internal structures at grain edges– implying any ferrimagnetic phases are scattered, few in total amount (below EDS detection and not near the grain surface) and too small to see ($<0.5 \mu\text{m}$) in optical microscopy. Biogenic baryte grains appear to form progressively in the ocean associated with organic matter films promoted by enhanced bacterial activity (Martinez-Ruiz et al., 2019). We speculate that the apparent net-ferro-magnetic behaviour of some biogenic baryte grains (see Fig S8i) is due to bacterial magnetofossils captured and dispersed through the grains, during the growth phase of the baryte particles associated with their origin in organic matter aggregates and films.

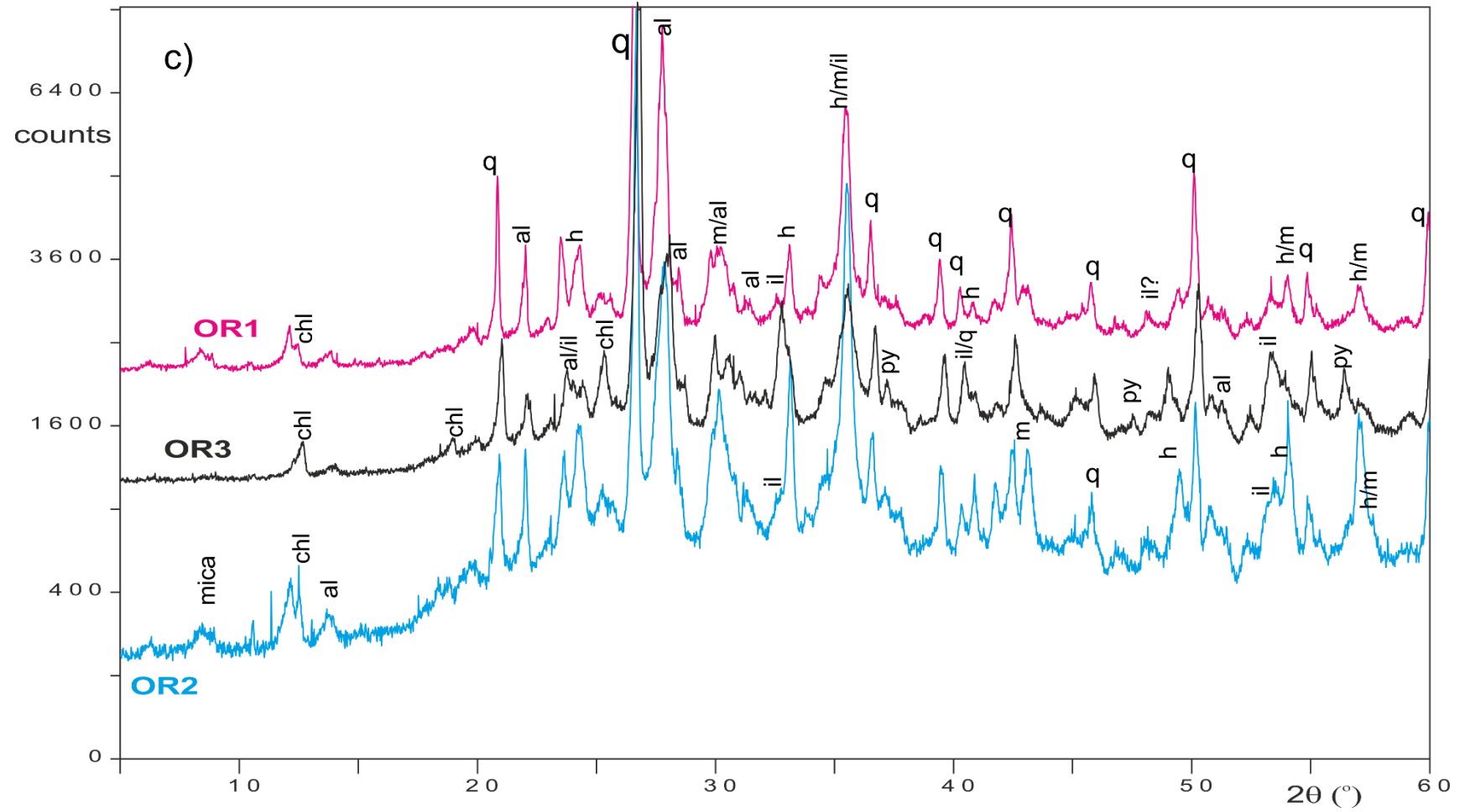
Sample code	χ_{LF}	χ_{ARMz}	SIRM	H'cr	%HIRM	weight%	weight% (x10 ⁻³)	¹ Paramagnetic MS	Extraction efficiency (%)			
	x10 ⁻⁷ (m ³ /kg)	x10 ⁻⁸ (m ³ /kg)	x10 ⁻⁵ (Am ² /kg)	(mT)	(%)	E _{mp} /wt-fine	E _{mp} /wt-fine		χ_{LF}	ARM	SIRM	0- 100 mT
LUA	2.11	42	392	248	38.2	0.076	1.37	0.57	7	40	12	24
LUD	1.22	29	112.1	57	3	0.064	0.67	~0.90	54	86	92	93
LUD2	0.25	7.9	14.0	55	11.1	0.470 ^s	na	nd	12	~0	31	31
LUD3	0.14	6.9	8.9	62	17.3	0.180 ^s	na	nd	7	5	15	13
OR1*	4.1	286	716	43	6	0.105	19.10	0.36	63	70	82	84
OR2*	4.8	279	715	41	6	0.890	11.50	0.29	66	59	79	85
OR4	1.24	12.5	36.1	53	6.4	0.071	0.97	0.96	17	33	51	53
OR5	1.20	13.1	36.7	53	6.6	0.111	0.56	1.00	10	7	54	56
OR3*	1.23	15.6	59.8	52	5.6	0.192	2.68	0.89	11	15	73	75
OR6	0.96	12.1	28.7	52	6.4	0.503	0.69	0.97	0	38	55	54
MR1	3.7	1203	1026	45	2.7	0.280	13.58	~ 0	44	74	67	66
MR2	1.27	8.8	23.1	48	6.9	0.137	3.77	1.00	0	58	62	67
MR3	1.59	28.7	63.1	50	9.9	0.145	4.51	0.82	31	81	8	83
MR4*	6.0	1196	965	37	2.8	nd	nd	0.06	50	88 ⁺	84	72
MR5*	3.5	1813	766	38	1.2	nd	nd	0.27	57	81 ⁺	65	~ 100
MR6*	1.58	9.8	34	61	6.1	nd	nd	0.95	41	~0 ⁺	62	51

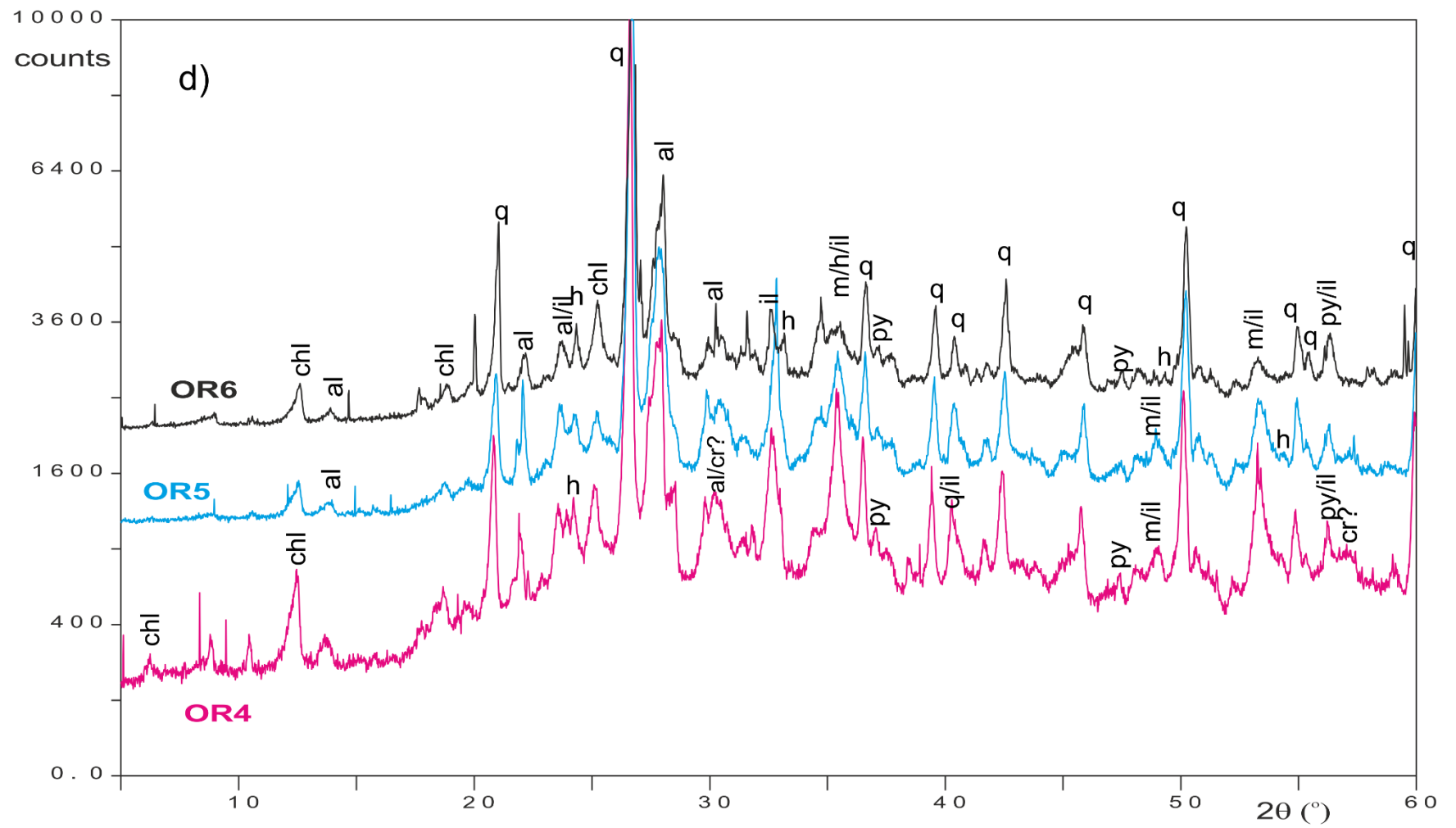
Table S2. Summary magnetic and magnetic extraction data for the magnetic extracts. The rock magnetic data relate to the material after carbonate dissolution using the method in Hounslow & Maher (1996, 1999a), and before extraction. Most of the OR and MR samples have high carbonate contents >70%. *= <63 μ m fraction, all others are sieved at 38 μ m. + some contamination from carbonate removal chemicals (see Hounslow & Maher (1996, 1999a) has artificially lowered this value. MS=magnetic susceptibility, SIRM= IRM at 1 T. %HIRM is % of IRM in the range 0.3- 1T. χ_{LF} =low frequency mass magnetic susceptibility. ARMz applied at 0.08 mT, 90 mT AF field. Wt-fine= weight of fraction using the magnetic extractions (i.e., <38 μ m or <63 μ m). H'cr= DC field used to acquire 50% of the SIRM (using forwards fields). E_{mp} and E_{mp} are the type of extracts described by Hounslow & Maher (1996, 1999a). Nd = no data, na = not applicable. \$= E_{me} extract of Hounslow & Maher (1996, 1999a). Paramagnetic MS is the proportion of the total MS (i.e. 1.0= all MS due to paramagnetic behaviour, 0= none or very little) in the original sample (after carbonate removal). ¹ estimated uncertainty \pm 0.03. MR4, MR5 and MR6 are E_{mp} type extracts used for the RRM analysis here.

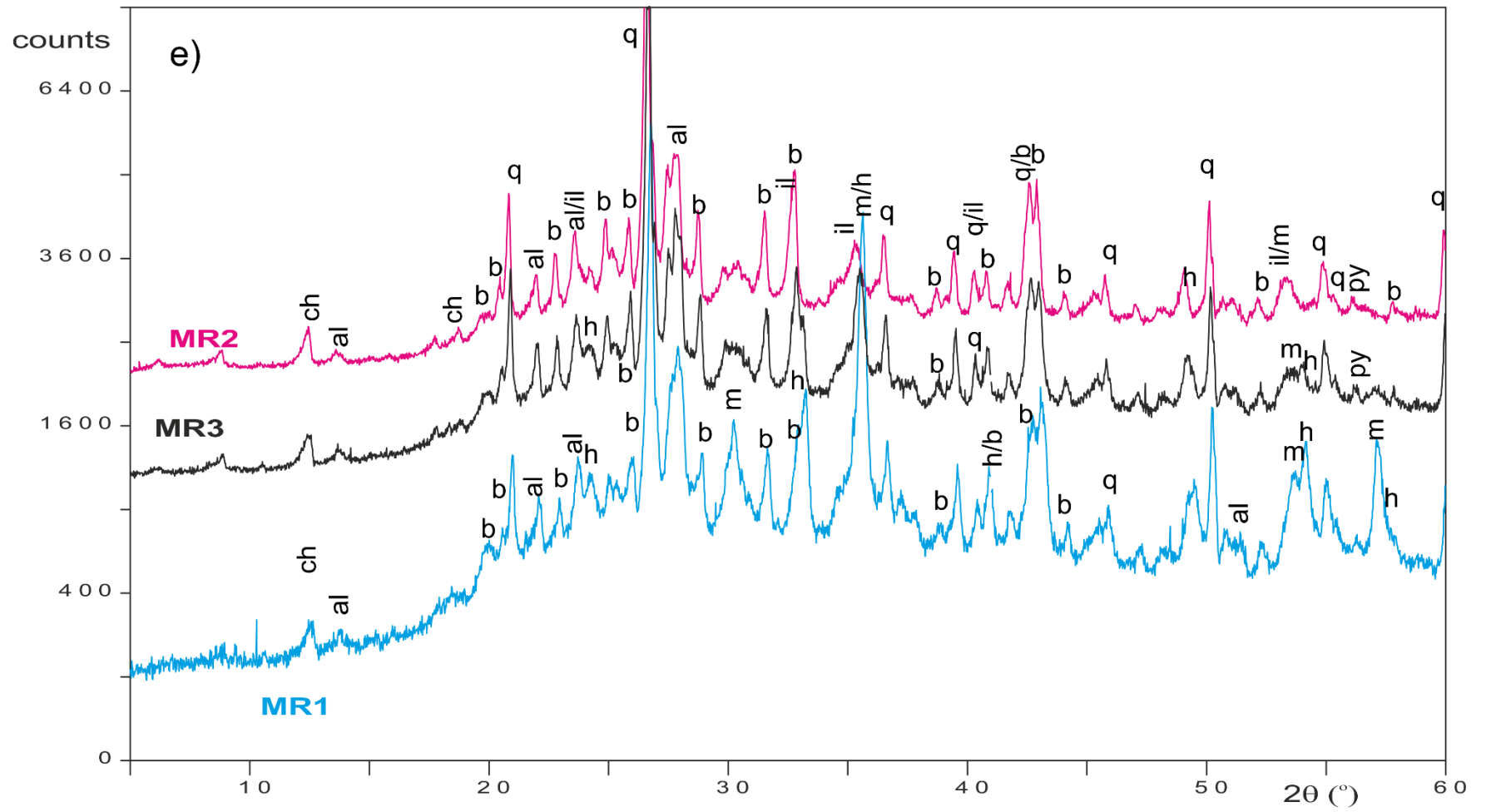
Sample code	Magnetite ² Cell edge spacing (Å)	Relative percent in extract (from XRD)								Weight % in fraction (x10 ⁻³ %)		From optical microscopy	
		Quartz	Plag. feldspar	Magnetite + spinels	Haematite	Ilmenite	Pyrite	Rutile	Baryte	Magnetite	hematite	Approx. % opaques ¹	Minor minerals
LUA [§]	nd	28.8	15.1	0	37.7	16.4	0	1.9	0	0.0	318	50	zir, spin, garn
LUD [§]	nd	59.6	32.8	3.3	2	0	0	2.4	0	2.3	1.8	5	rut, spin, zir, ank, mica, apa
LUD2	nd	nd	nd	nd	nd	nd	nd	nd	nd	nd	nd	tr	brown and clear mica, ank
LUD3	nd	nd	nd	nd	nd	nd	nd	nd	nd	nd	nd	tr	brown mica, garn, tour, green mica, rut, zir, ank
OR1*	8.381	33.6	45.5	11.5	6.6	2.7	0	0	0	140	100	22	prx, hor, chl, spin, mic
OR2*	8.379	20.8	45.4	15.8	7.5	7.7	2.8	0	0	165	101	28	prx, hor, tour, zir, rut, mic
OR4 [§]	8.383	26.9	39.4	6	3.1	16.3	6.9	1.4	0	8.0	3.2	nd	mic, chl, hor, rut
OR5 [§]	8.369	28.6	36.3	3.6	0	16.9	8.8	5.8	0	7.1	0.0	nd	mic, chl, hor, rut
OR3*	8.392	29.3	29.1	7	5.9	16.5	12.2	0	0	17.9	18.9	30	rut, mic, hor, chl, apa, spin
OR6 [§]	too low	37.7	41.2	0	0	6.5	12.3	2.4	0	0.0	0.0	nd	mic, chl, hor, rut
MR1 [§]	nd	25.1	25.2	25.8	13.2	0	0	0	10.7	110	88.0	nd	nd
MR2 [§]	nd	34.4	29.5	1.7	0	17.5	0	0	17	3.5	0.0	nd	nd
MR3	nd	31.9	29.4	5.7	4.1	14	0	0	14.9	10.0	9.0	nd	nd
MR4*	nd	19.6	28.7	22.6	2.9	0	0	0	26.2	nd	nd	common	bary, apa, rut, haem
MR5*	nd	32.6	29	5.8	1	0	0	0	31.7	nd	nd	common	rut, apa, bary
MR6*	nd	27.7	36.5	0	0.4	3	0	0	32.4	nd	nd	few	apa, glass, bary

Table S3. Summary mineralogical data for the magnetic extracts, largely based on semi-quantitative XRD, using the method detailed in Hounslow & Maher (1999a, 1999b). The weight % are those in the appropriate fraction of the sediment (* <63 or § < 38 µm; LUD2=38-63 µm, LUD3=63-250 µm) ¹ excludes leucoxene which may appear opaque in transmitted light by has bright internal reflections in reflected light. ² using internal quartz reference peaks. nd= no data, tr=trace. Minor minerals: apa= apatite, ank= ankerite, bary=baryte, garn= garnet, rut=rutile, haem=haematite, mic= mica, chl= chlorite/chlorotoid, spin= spinels (most Cr), hor= hornblende, prx= pyroxene, zir=zircon, tour=tourmaline, glass=volcanic glass. See Fig. S5 for some of the source XRD data.









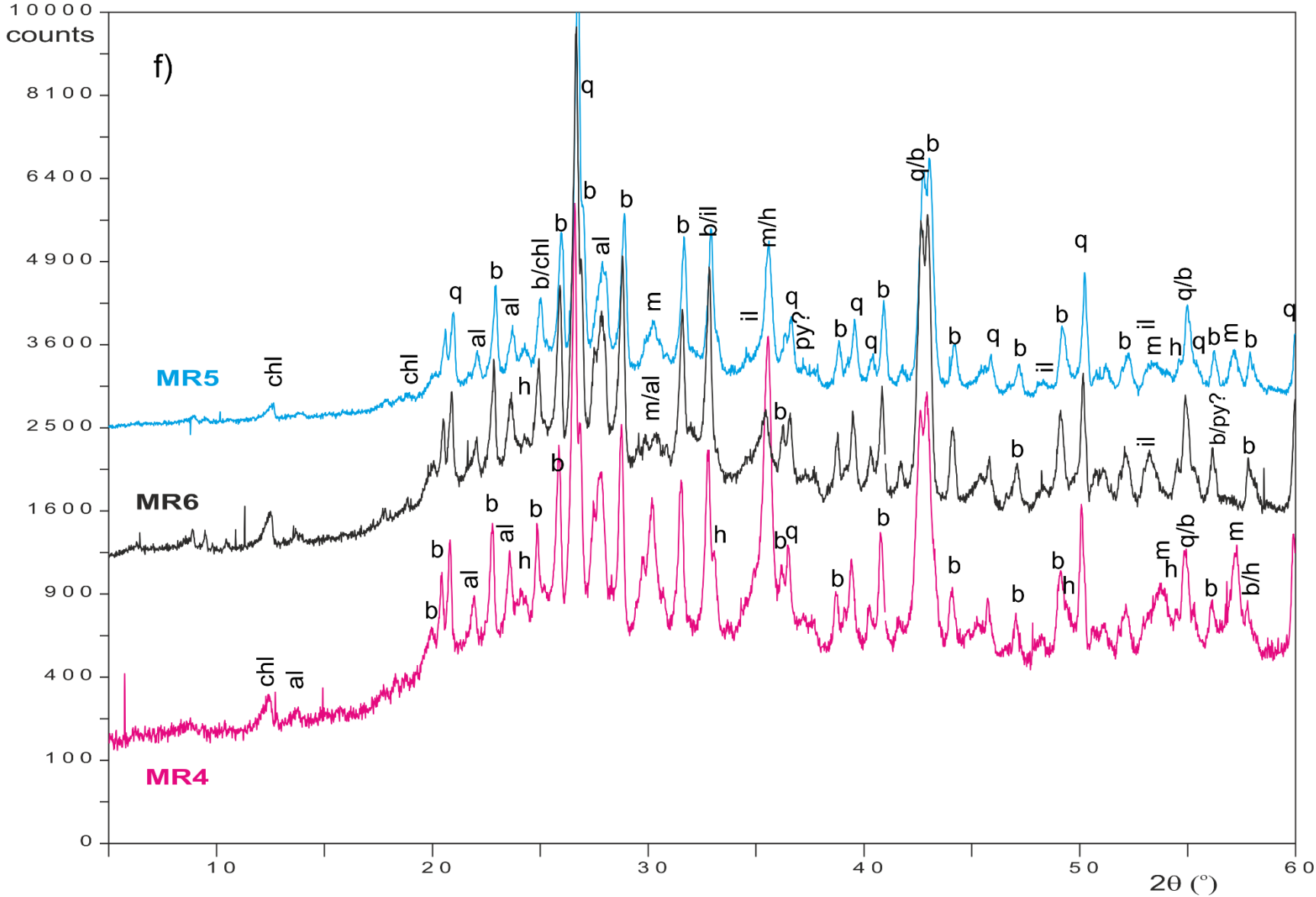


Fig. S5. X-ray diffraction data for the magnetic extracts (b-f), and two example ones from the Chalk (a). In each case these are the extracts from the E_{MP} type extracts of Hounslow & Maher (1996), eventhough the MR4,MR5,MR6 test samples use E_{MPT} type extracts. The peaks have been labelled with the inferred corresponding minerals: m= magnetite, h=haematite, il=ilmenite, py=pyrite, q=quartz, al=albite (or similar plagioclase feldspar), b=baryte, chl=chlorite, an=anatase, or=orthoclase or similar K-feldspar, ru=rutile, cr=chromite. /=peaks overlap here, ?= alternatively may be from one of the feldspar or phyllosilicate phases. In a) the SB53 sample (no RRM measurements here) is from Scrathell's Bay on the Isle of white, and has similar but lesser abundance of magnetofossils, most of which are in the E_{MPT} extract. Extract samples LUD2, LUD3 have no useful XRD data. The large quartz peak has been truncated in a-e.

This paper	Native	Other sample codes
+Sample code	Sample code	Code & depths below sea floor
LUA	A36b <38 μm	Lunde group A ¹
LUD	A45a <38 μm	Lunde group D ¹
LUD2	A45A 38-63 μm	Lunde group D ¹
LUD3	A45A 63-250 μm	Lunde group D ¹
OR1*	L35 <63 μm	722B (0.35 m) ² zone 1 oxidized
OR2*	L36 <63 μm	722B (1.25 m) ² zone 1 oxidized
OR4	L58 <38 μm	722B (38.6 m) ² , reduced interval, zone 5
OR5	L59 <38 μm	722B (40.6 m) ² , reduced interval, zone 5
OR3*	L42 <63 μm	722B (7.8 m) ² partially reduced interval, zone 3
OR6	L69-70 <38 μm	722B (59.5-61.5 m) ² , reduced interval, zone 5
MR1	L23-24 <38 μm	709A (118.4-120.4 m) ²
MR2	L20 (1) <38 μm	709A (112.9 m) ²
MR3	L10-11 <38 μm	709A (28.0-29.7 m) ²
MR4*	709 A/A	³ 709A (1H-4, 5.9-8.4 m) high SIRM/ARM subset
MR5*	709C-3H-3	709C (22.8- 23.5 m), partially reduced set
MR6*	709C/D	³ 709C (6H; 44.3-53.9 m), reduced set

Table S4. Shows the relationships of sample codes used here and in prior publications (¹Hounslow et al. 1995; ¹Hounslow, 1996; ²Hounslow & Maher, 1996; 1999b) about these extracts. ³ Additional data in Maher & Hounslow (1999, figs. 3, 4). MR4, MR5, MR6 are the E_{mpt} extracts, others <63 μm or <38 μm are E_{mp} type extracts and LUD2, LUD3 are E_{me} type extracts (Hounslow & Maher, 1999a). * <63 μm sediment fraction used for extraction instead of <38 μm .

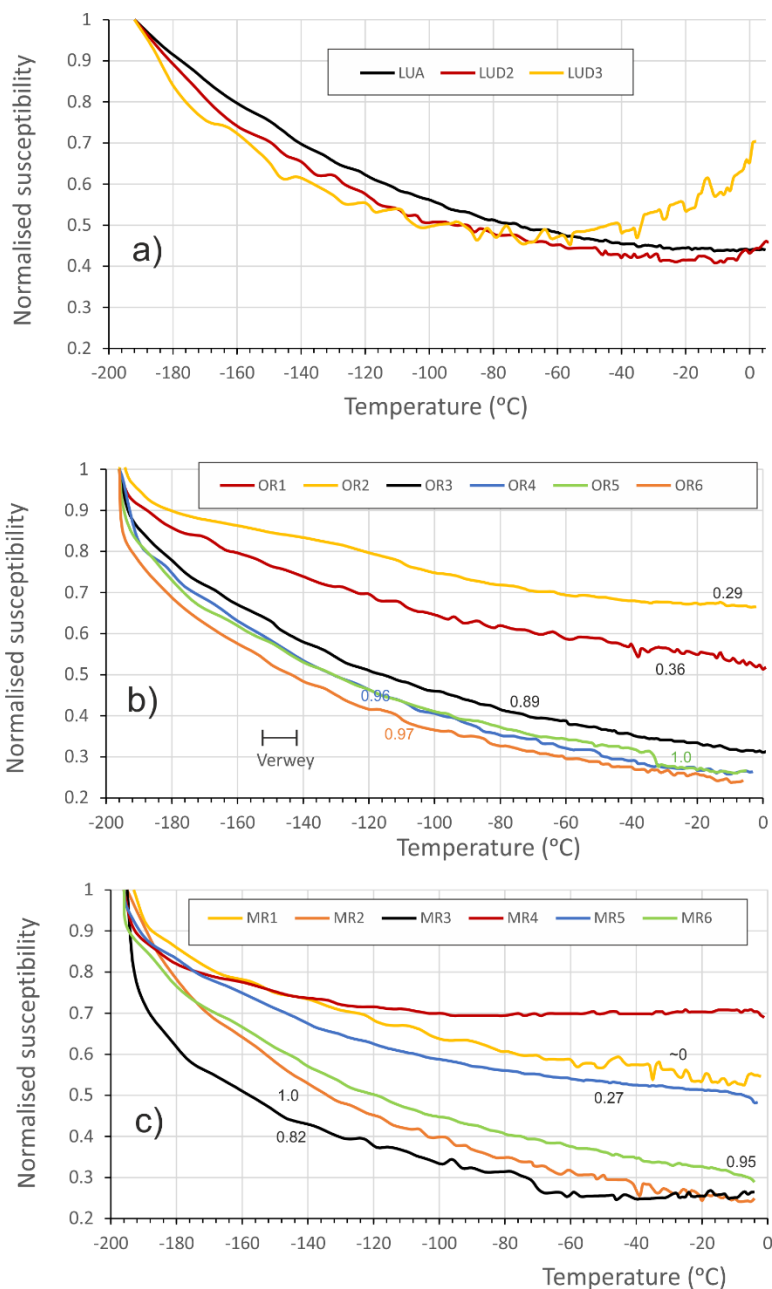
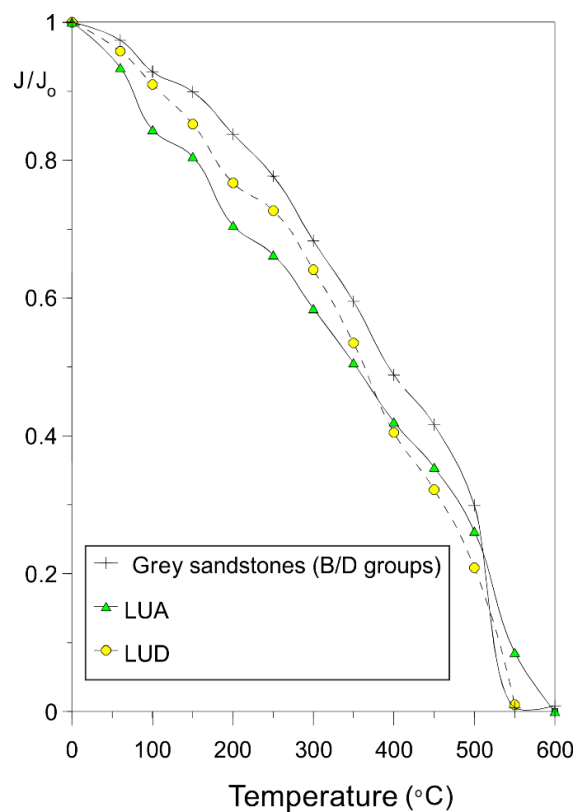


Fig. S6. Low temperature magnetic susceptibility data for the magnetic extract samples (prior to the magnetic extraction, but after carbonate removal). Note the absence of the Verwey transition, and the variable contribution of paramagnetic minerals to the magnetic susceptibility (proportion at 0°C shown next to curve, using method in Hounslow et al., 1995). The data for LUD2 LUD3 are impacted by some thermal drift in the Bartington meter.

Fig. S7. Thermal demagnetisation of the normalised ARMz (J/J_0) in whole-rock specimens representative of the Lunde extracts. Note the broad range of blocking temperatures in the samples and the Curie temperature $\sim 550-600^\circ\text{C}$.



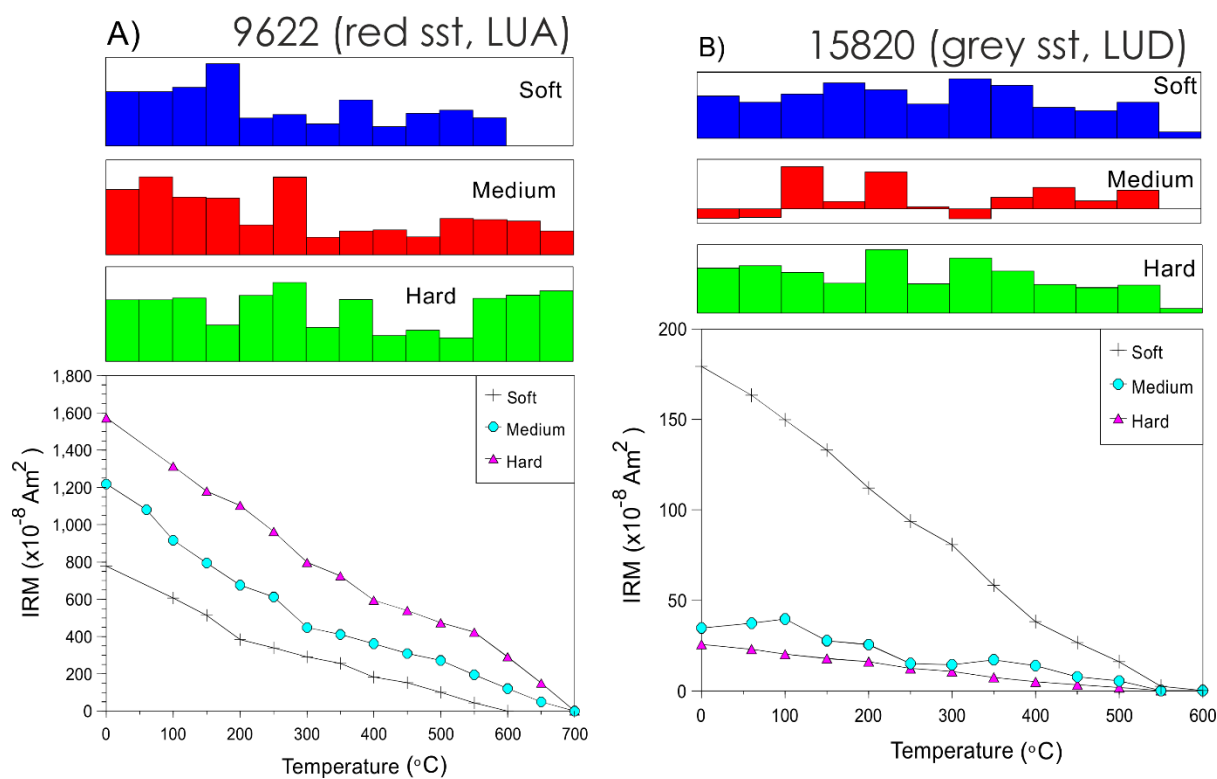


Fig. S8. Thermal demagnetisation of a three component IRM in samples representative of the Lunde magnetic extracts (soft= 0-0.1 T, medium= 0.1- 0.3 T; Hard= 0.3-1 T coercivity fractions). In sample 9622 (a red coloured palaeosol), note the broad range of blocking temperatures and the haematite Curie temperatures at ca.700°C for the hard and medium coercivity components. The soft coercivity component is demagnetised at 550-600°C like the ARMz shown in Fig. S7.

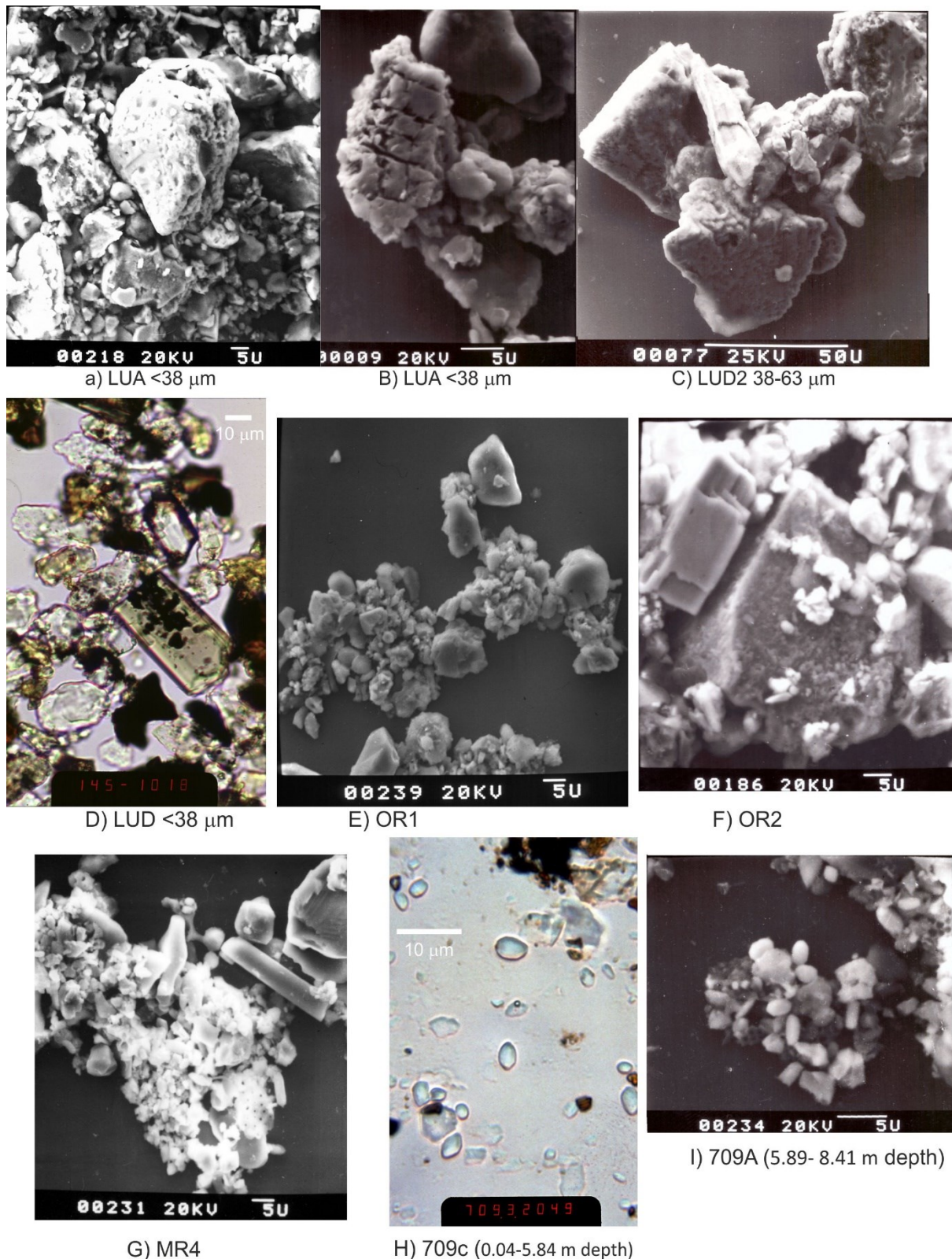


Fig. S9. Typical features of the magnetic extract test samples. Scanning electron microscope images (a-c, e-g, i). Transmitted light optical micrographs (d, h) under oil immersion. A) Sample LUA (<38 μm fraction) showing a cluster of magnetic particles from $\sim 1 \mu\text{m}$ to $\sim 35 \mu\text{m}$ in size. Large pitted grain is Fe-Ti rich and is likely an ilmenite or ilmenco-haematite detrital particle. Of the smaller particles many are angular and not rounded and may in part represent broken and fragmented relicts of original Fe-Ti-Mn-Cr particles (see Hounslow, 1996 for details).

- B) Sample LUA (<38 μm fraction) largest grain is a pitted Fe-Ti grain rich in Ti probably representing an ilmenite or Fe-rich rutile grain in which Fe has been leached from the irregular lamellae like features by diagenesis. Rounded grain at top is a zircon.**
- C) LUD2 (38- 63 μm fraction), a magnetic clump of grains, with on the left two large detrital Fe-Mn grains (Mn substituted magnetite), and in the top-right is an Fe-Ti grain (ilmenite or martite). The elongate fragment attached to top of cluster is also a Mn-Fe rich grain, a probable relict of a decomposed primary grain.**
- D) LUD (<38 μm fraction) showing a typical view of an extract with a mix of clear quartz and feldspar, some with opaque inclusions, some nearly opaque rutiles (dark ruby colour), scattered detrital opaques, and in the centre a green tourmaline grain with opaques; directly above is a smaller zircon (high relief) particle.**
- E) Typical Owen Ridge extracts (OR1) showing magnetic clump of small (0.5- 10 μm) particles. The larger grains around the edge of the clumps are feldspars (Ca-Mg rich) and the finer-grained clusters are Fe-Ti rich (mix of Ti-magnetite, ilmenite and Ti-hematite).**
- F) Sample OR2 showing two large feldspar grains. One on right has a rough surface (and richer in K), and the one top left has cleavage-like surfaces and is angular. Both also give strong Fe-Ti EDS spectra indicating they are heavily included with Fe-Ti oxides and have magnetically (?) attached brighter Fe-rich particles (probably magnetite).**
- G) Typical SEM view of magnetic extract from Madingley Rise (MR4), showing a magnetic clump with satellite additional siliceous microfossil fragments. Large grain in top right is Ca-P rich and probably a biogenic phosphate fragment. In TEM the irregular and porous nano-structure of the siliceous fragments sometimes contained Fe-oxide particles (and magnetofossils), which probably accounts for their common presence in the extracts at this site (B. Maher pers comm.).**
- H) x1000-Optical micrograph view of typical Madingley Rise extract from the cores (in this case composite of samples 0.04-5.84 m depth) showing a collection of largish typically ellipsoidal biogenic baryte grains (high relief, 'bluish'), and in the top a magnetic clump of Fe-oxides. Some are clumped together (bottom left), other not. The barytes contain no observable opaque grains.**
- I) Magnetic clump of largely detrital grains (Madingley Rise extract, 5.89- 8.41 m) with brighter ellipsoidal biogenic baryte attached, apparently magnetically aligned to the cluster, suggesting that for reasons which are unclear, these barytes have a net ferromagnetism. Compare this to H) where many of the barytes are not clumped and therefore have a much weaker net ferromagnetism.**

2. Further information about noise characteristics of the RRM

Since RRM is often weak in sediment samples (sometimes undetectable in limestones), it is important to evaluate the impact of noise on the measurements, to both consider the uncertainty in the RRM measurements and its impact during demagnetisation. There are two main sources of noise in the RAPID system at Lancaster, the first is the measurement noise which is suitably evaluated during the four SQUID measurements defining the moment (4 on z-SQUID for Z-axis, two on each of the x and y SQUID for X and Y axis components), and secondly noise from demagnetisation.

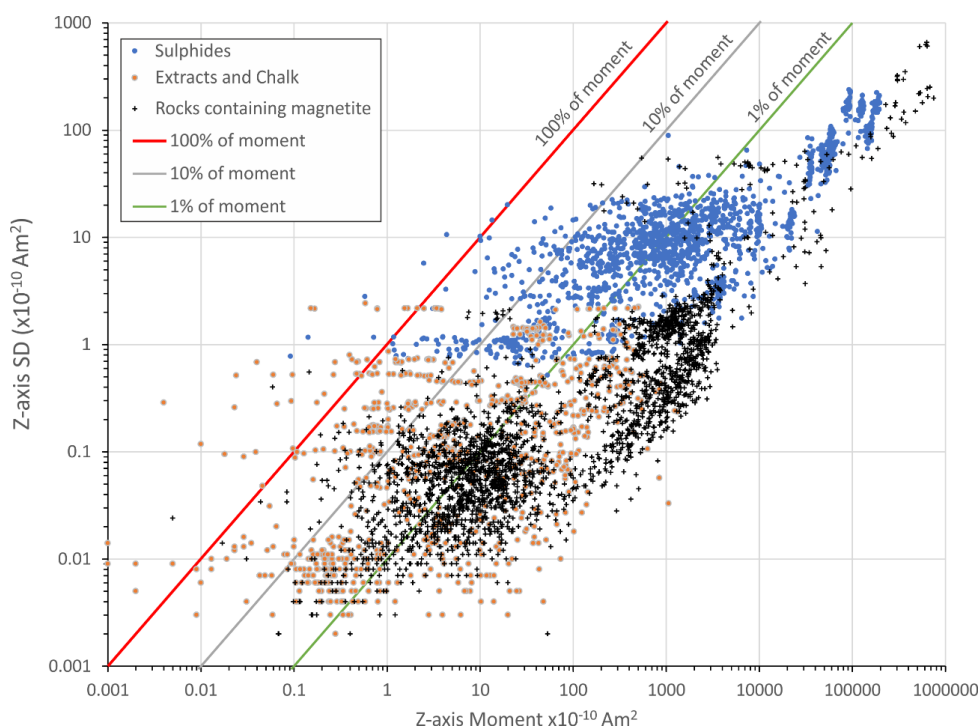


Fig. S10. The standard deviation of the raw measured moments (MSD) along the Z-axis (i.e., that which the RRM and ARMz are acquired along) versus the magnitude of the measured moment (after removal of holder+ rod moment). This clearly shows that overall, the measurements have MSD less than 10% of the net moment (~ 1% on average) when the moment is <10000 x10⁻¹⁰ Am² and around 0.1% at moment > 10000 x10⁻¹⁰ Am². The measurement floor is around 10⁻¹² Am² on the Lancaster RAPID on a good day with a well cleaned holder.

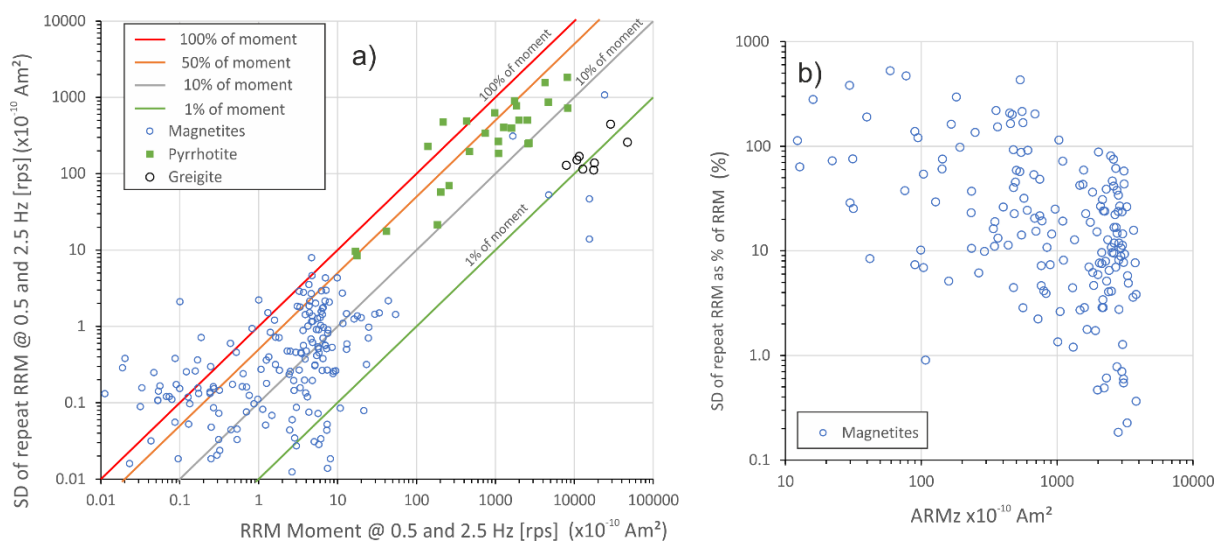


Fig. S11. a) The standard deviation (RSD) of the limited number of RRM repeats. RSD shown on both y-axes is the moment in a), and as percentage of RRM in b). The RSD is determined from two repeats for most, but three repeats for some. Compared to the MSD in Fig. S10 the RSD is considerably enhanced at some 1 to 100% of the RRM moment. The RSD of magnetite-bearing samples shown in b) has a rather weak relationship to ARMz moment, which suggests some of the scatter in RSD is inversely related to abundance of magnetic minerals. The four lines shown in a) are the percentages of RSD with respect to the RRM moment.

The measurement standard deviation (MSD) is related to the samples net moment (Fig. S10). The subtraction of the holder and quartz-silica rod moment (with attendant MSD) from the measurement moment will also impact on the final RRM uncertainty, so it might be expected that at moments close to the holder+rod value the uncertainty of the RRM will increase, which is seen in the increased uncertainty in RRM moments at less than ca. $0.2 \times 10^{-10} \text{ Am}^2$ (Fig. S11A; the quartz-silica rod has a demagnetised NRM of ca. $0.15 \pm 0.4 \times 10^{-10} \text{ Am}^2$). This is probably also the reason for the increased % uncertainty shown in Fig. S11b for ARMz less than ca. $1000 \times 10^{-10} \text{ Am}^2$. This suggests that RRM moments below ca. $1 \times 10^{-10} \text{ Am}^2$ benefit greatly from repeat RRM measurements for enhanced quantification.

However, the scatter in RSD in those samples with RRM moment above $1 \times 10^{-10} \text{ Am}^2$ is rather larger than might be expected from combining MSD alone, and so there is another, larger source of noise—perhaps generated after the RRM at maximum field, and during sample rotation in the decay stage of the AF field (i.e. RRM-noise). A part of this variability in RSD may be related to the inadequate (only 2 to 3) number of repeats to characterise RSD. Perhaps part may be related to anisotropy in the sample if it moves during RRM acquisitions? Notably, the pyrrhotite samples have a much larger RSD than the greigite and the magnetite bearing rocks with high-moments. The source of the additional noise contributing to RSD is not understood, but seems to be a problem for some other published studies with a pyrrhotite NRM and AF demagnetisation. For those pyrrhotite samples with RRM $< 100 \times 10^{-10} \text{ Am}^2$ the RSD was not related to either the MDF of ARMz, or to particle size as measured proxied by the ARMz/SIRM ratio. The RRM stability is also similar for both greigite and pyrrhotite (main text Fig. 12a), suggesting this additional RRM-noise is not controlled by RRM stability.

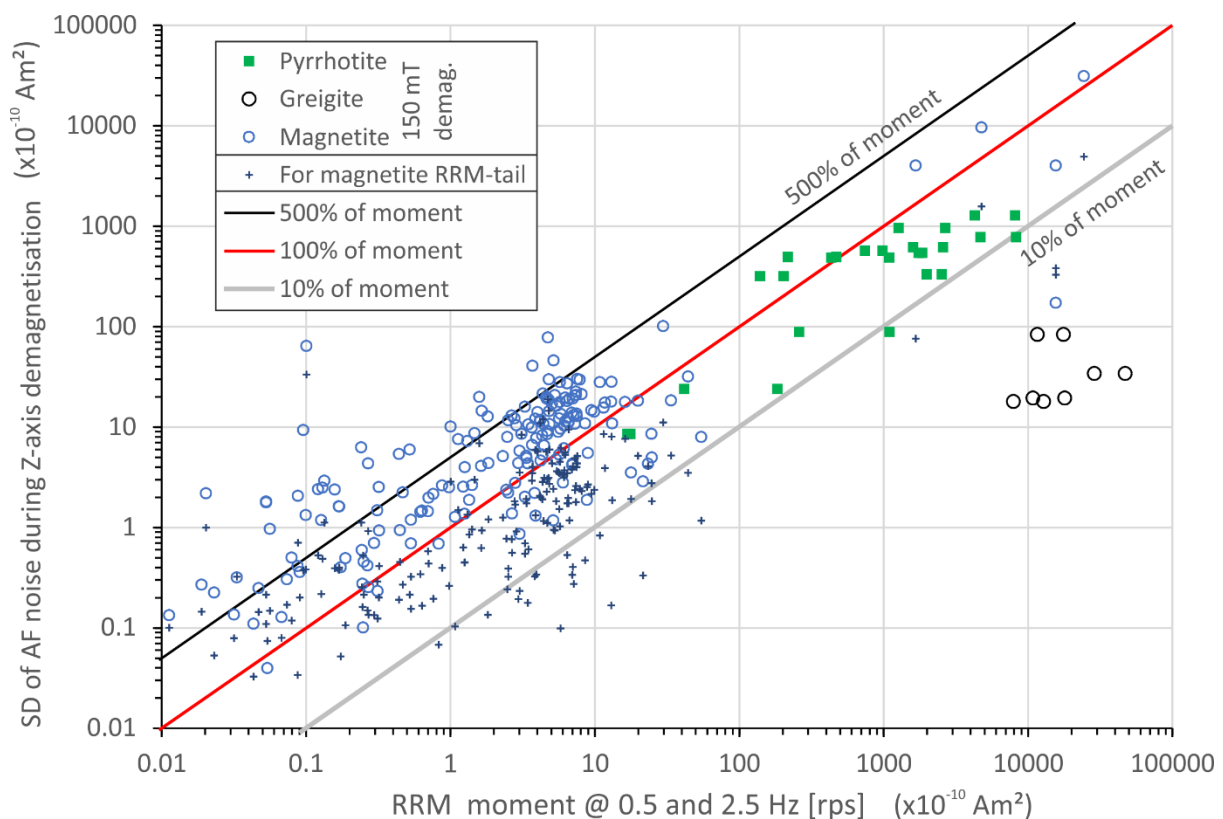


Fig. S12. Standard deviation of the sample remanence after being subjected to AF demagnetisation at 150 mT along the Z-axis (ZSD), versus the RRM moment acquired at 100 mT. This is shown for the three types of mineralogy (top part of legend). Also shown as crosses are estimates of the SD for the moment of the tail of the RRM demagnetisation curve (RRM-tail)— this data is largely from the RRM demagnetisation method-1 (see main

text), using data points up to around 100 mT demagnetisation fields. Note the lower RRM-tail SD values than the ZSD indicating high field-strength-dependency of the Z-axis demagnetiser noise. The three lines are the percentages of SD with respect to the RRM moment.

With conventional ARMz demagnetisation it is commonly assumed that AF demagnetisation at or above the AF field used in the ARMz production provides a suitable 'zero' or baseline level for determining the ARMz magnitude (also accounting for any residual remanence). This procedure was adopted here for the ARMz and ARM_{ROT} , since these remanences are large compared to the uncertainty in determining the 'zero' level. However, the small magnitude of the RRM along with the often-large standard deviation at 150 mT demagnetisation (ZSD; Fig. S12), precluded the use of this simple procedure for RRM demagnetisation (not to mention the additional GRMz generated –see main text). With ZSD typically 1 to 5-times larger than the resulting RRM for magnetite-bearing rocks (blue circles in Fig. S12). A better approximate method is to utilise several points on the tail of the demagnetisation decay curve to estimate the 'zero' level. This was used for assessing the RRM demagnetisation curves and the resulting determination of MDF of RRM. As explained in the main text, method-1 does not isolate the GRMz, whereas method-2 allows GRMz isolation from the RRM decay curve, but either method requires a base-line zero level to be determined to locate the magnitude of RRM or GRMz.

In summary, the uncertainty assessment suggests:

- RRM with magnitude less than about $0.5 - 1 \times 10^{-10} \text{ Am}^2$ benefit from repeat measurements.
- Uncertainty of the RRM measurements is larger than the sum of the measurement uncertainties, indicating additional sample and/or mineralogy related RRM-noise. This probably makes RRM measurements with respect to rotation rate, a better choice for use in mineral magnetic identification, since RRM measurements at single ω may be subject to additional unforeseen uncertainty, which can be identified by additional RRM at adjacent ω values. Alternatively repeats at a single rotation rate.
- Conventional zero-level determination seems suitable for determining ARMz and ARM_{ROT} in the presence of a residual remaining remanence after demagnetisation. However, this procedure is unsuitable to use for RRM demagnetisation, and the tail of the RRM demagnetisation curve should be used at fields beyond the maximum AF field used to generate the RRM decay curve. Method-2 for RRM demagnetisation should be used.
- RRM acquisition with AF field is probably the preferred method for assessing RRM stability, and since RRM can be weak in many sediments it may be best to adhere to a fixed AF field for acquisition (e.g. 40 mT), since it seems more reliable to determine this with repeat measurements, than to determine the median acquisition field from multiple, probably noisier single measurements at various AF fields (see Section 3.3).

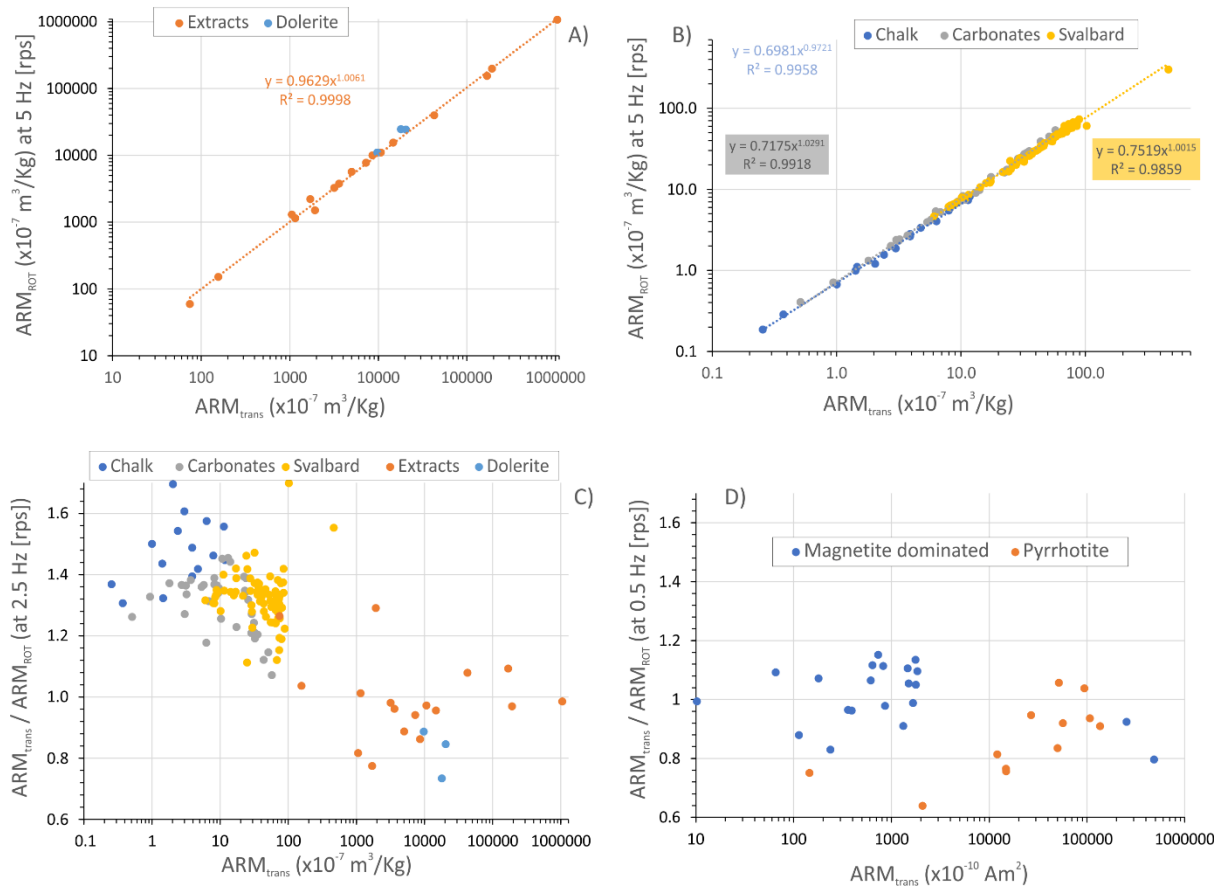
3. Additional information about RRM-related magnetic properties

3.1 Estimating the rotational ARM from a static transverse ARM

For kinds of equipment other than the RAPID it may not be possible to determine a rotational ARM, but only a transverse static ARM. Hence, a limited investigation was undertaken on recovering the ARM at a rotation rate of zero (ARM_{trans}), using the same configuration as that when acquiring the ARM_{ROT} . The difference is that ARM_{trans} is a single measurement obtained by using the same base-line zero level as that for the ARM_{ROT} . This was done for a large set of the samples (magnetic extracts, dolerites, various rock samples, Fig S13a,b,c) at $\omega=2.5 \text{ Hz}$ [rps], and for a small set (various stronger magnetite dominated samples and extracts, and pyrrhotite samples;) at $\omega=0.5 \text{ Hz}$ [rps] (Fig. S13d). Generally, there is a good correspondence between ARM_{trans} and ARM_{ROT} , but the

relationships vary somewhat between sample sets, as shown by the equations for the regression fitted lines in Figure S13(a, b). Figures S13(c, d), show that if using ARM_{trans} to estimate the ARM_{ROT} , this is subject to an uncertainty of the order of $\pm 10\%$ in ARM_{ROT} , and also a dependence on the magnitude of the ARM (Fig. S13c,d). As such the regression equation here for the magnetic extracts (Fig. S13a) may be best for strongly magnetic samples, and one of the rock-based ones for weaker samples (Fig S13b).

Fig. S13. The relationship of the transverse static ARM (ARM_{trans}) to the ARM_{ROT} values at rotation rates of 0.5 revs^{-1} (panel D) and 2.5 Hz [rps] (panels A, B and C; $T_H = 92 \text{ ms}$). The regression equations in A and B are colour coded according to the sample set used (chalk= bacterial magnetite set, carbonates= mixed magnetite and a possible(?) pyrrhotite-like phase (not in main paper) with both negative and positive RRM's, Svalbard=sample set from Svalbard in main paper, extracts= set as in this work). C and D the ratio of ARM_{trans} / ARM_{ROT} which shows the within-sample set variability, and what appears to be a magnetic mineral abundance control on this ratio (i.e. smaller ARM_{trans} / ARM_{ROT} for larger ARM). The pyrrhotite dataset is particularly noisy (see later also).



3.2 The RRM acquired in a DC bias field of $100 \mu\text{T}$

A limited investigation was undertaken on possibly utilising the RRM which was generated under those conditions of applied DC bias field used for determination of the ARM_{ROT} value. This is the RRM_{100} value (i.e. acquired during DC bias field of $100 \mu\text{T}$). This was obtained by subtraction of the rotational ARM values obtained for the $+\omega$ and $-\omega$ rotation states. RRM_{100} are broadly consistent with the RRM obtained with no DC bias field but display larger imposed noise since RRM_{100} is superimposed on a much larger ARM_{ROT} (Fig. S13). This also the case for differing peak AF hold times (Fig. S20). In magnetite-dominated samples the RRM_{100} noise is of the order of 10-15% of the RRM at $|RRM|$ less than ca. $300 \times 10^{-10} \text{ Am}^2$ (Fig. S14B,C,d), but larger than this at $< 0.05 \times 10^{-10} \text{ Am}^2$ (Fig.

S14a). At $>80,000 \times 10^{-10} \text{ Am}^2$ the noise may be less than ca. 5% (Fig. S14d). Greigite samples as here display comparable scatter in values (Fig. S15c). This is in contrast to pyrrhotite samples which display greatly enhanced noise in both RRM and RRM₁₀₀ (Fig. S15a,b).

Overall RRM₁₀₀ is of little use for additional evaluation of the RRM process, although the data suggests that RRM₁₀₀ may most often underestimate the RRM (see Fig. S14a,d), for a reason that is unclear.

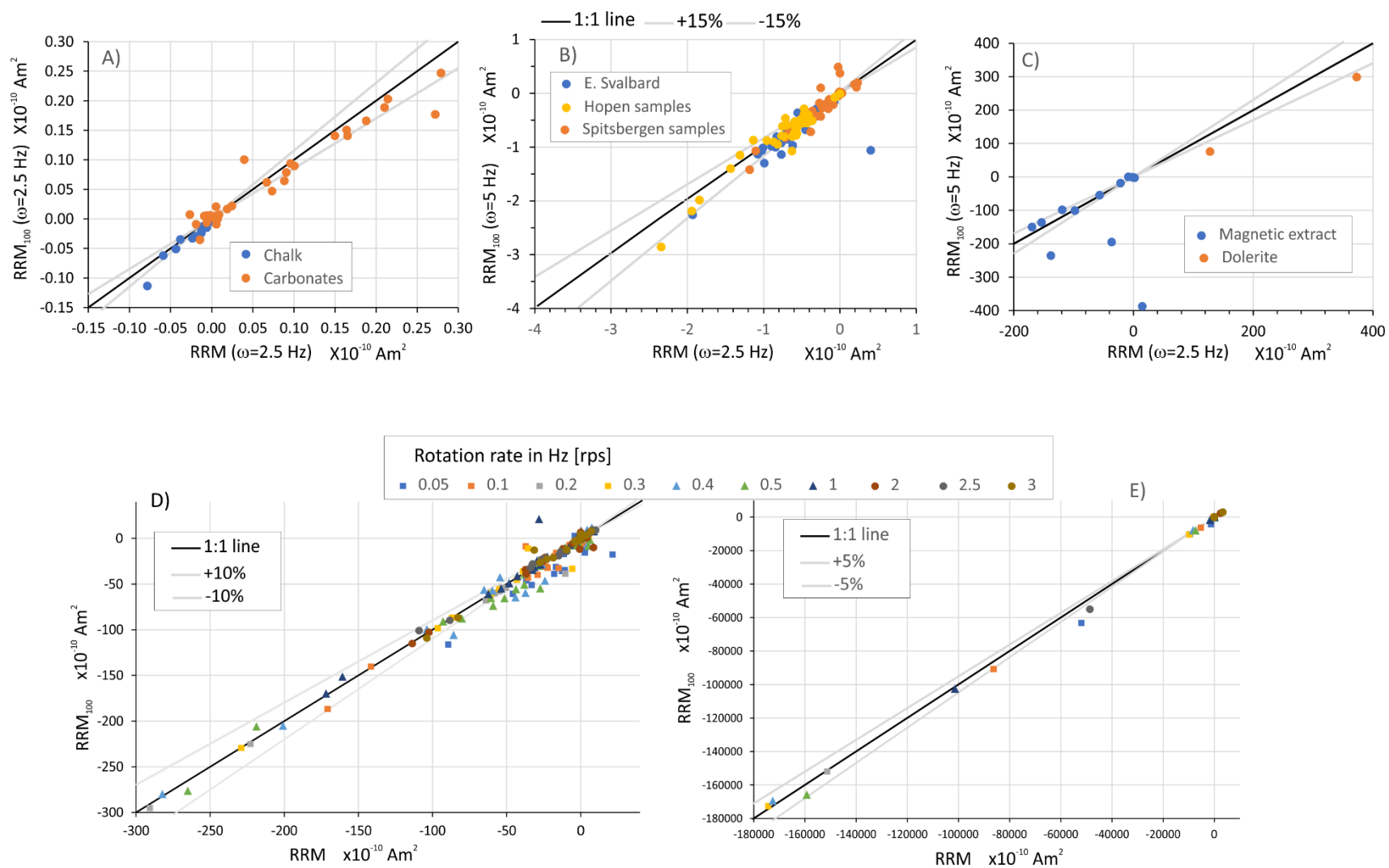


Fig. S14. Data for the RRM acquired under zero DC bias and that acquired during a DC bias field of 100 mT (i.e. RRM₁₀₀) at $\omega=2.5$ Hz [rps] (A,B, C) and with respect to rotation rate in D and E. The datasets have been separated in the graphs due to the large variation in RRM intensity,

to allow the spread of data points to be seen ($T_H = 92$ ms).

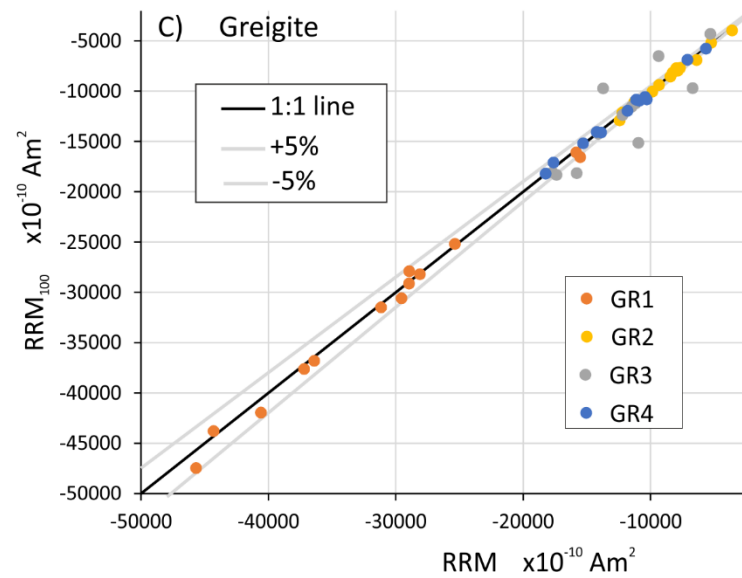
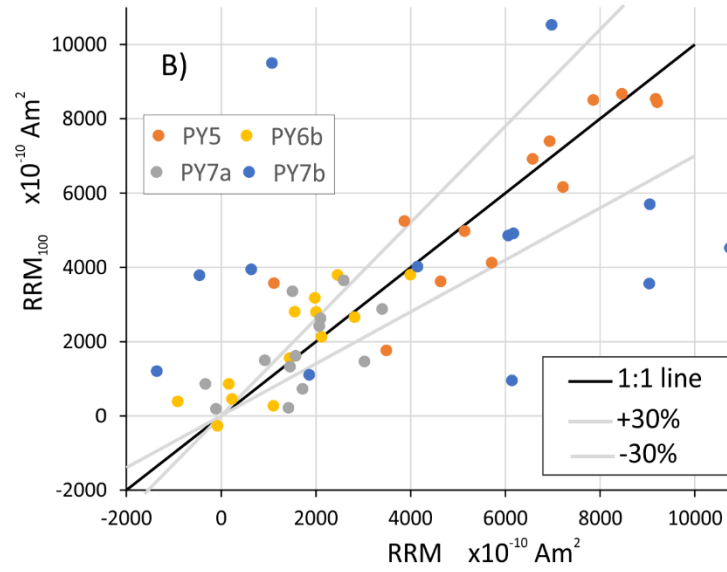
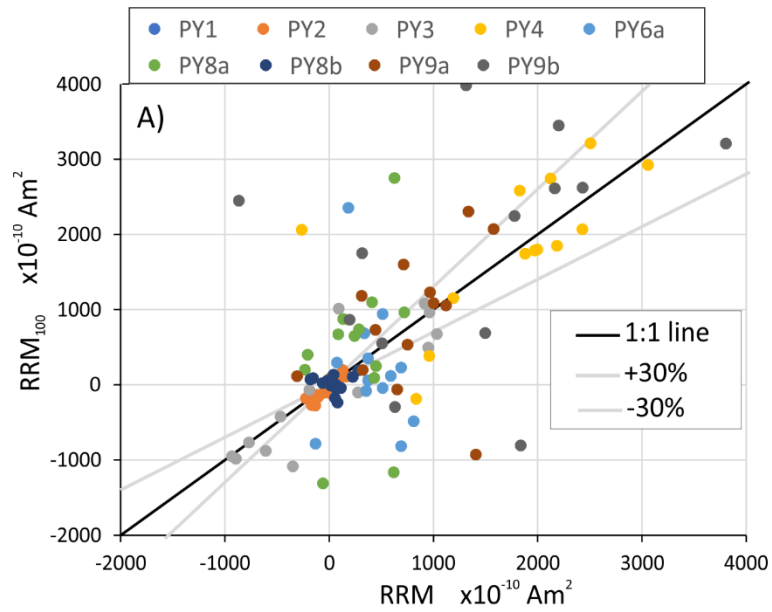


Fig. S15. Data for the RRM of pyrrhotite and greigite acquired under zero DC bias and that acquired with a DC bias field of 100 mT (RRM_{100}) at rotation rates ω of 0.05 to 3 Hz [rps] (sample codes as in this work, $T_H = 92$ ms). The dramatically noisier response of pyrrhotite apparent in A and B with $\pm 30\%$ error bands on RRM, but with RRM_{100} uncertainty for greigite comparable to that obtained with magnetite at similar RRM intensities in C (see Fig. S14e).

3.3 The RRM and ARM_{ROT} acquisition process with respect to the AF field intensity.

In comparison to the test magnetite samples used by Potter and Stephenson (1986) our samples display a limited approach to saturation of the ARM_{ROT} - theirs were nearly saturated by 50 mT (although their data were produced as a tumbling ARM_{ROT}). RRM acquisition is not saturated at 100 mT (Fig. S16), which is usually the case for samples previously studied for RRM at 80-100 mT peak field (Wilson & Lomax, 1972; Potter and Stephenson 1986; Snowball, 1997).

To compare the variation of RRM, ARM_{ROT} and B_g with respect to peak AF field and rotation rate, we normalise the values to that at $\omega=0.5$ Hz [rps] (Fig. S17). These indicate that the RRM shows similar changes with ω , with the most similar being samples MR1 and PY5 (over the range of rotation rates). The larger absolute normalised values tend to be consistently the lower AF fields (top row in Fig. S17). The relative changes with peak AF are also similar for the B_g values (bottom row of Fig. S17).

The normalised ARM_{ROT} values for the magnetite-bearing samples show the largest variability with respect to rotation rates, with the peak AF at ≤ 80 mT having negative slopes with respect to ω , and that at 100 mT a small positive slope. This variability in normalised ARM_{ROT} must be in part be related to the differing activated coercivity fractions carrying the ARM_{ROT} . This demonstrates that standardising the maximum AF field for ARM_{ROT} acquisition is an important issue, so that comparison of B_g values obtained with differing peak AF fields will least impact the shapes of the B_g to ω relationships (although the relative changes in ARM_{ROT} are mostly within $\pm 7\%$ of the value at 0.5 Hz [rps]).

The fact that the percentage of RRM and ARM_{ROT} varies between samples (Fig. S18) are useful additional properties comparable to the stability of the RRM and ARM_{ROT} to AF demagnetisation. This suggests that instead of demagnetisation of the RRM as a measure of RRM stability, the proportion of RRM acquired between 40-100 mT (or proportion acquired at 40 mT), or the median acquisition field of the RRM may be better alternatives to RRM demagnetisation, since they will be free of GRMz which complicates the RRM demagnetisation. That part between 0.5-1.5 Hz [rps] appears relatively consistent (Fig. S18) and a rotation rate in this interval may be a useful 'standard' rotation rate to use for both RRM and ARM_{ROT} (if using a hold time of 92 ms).

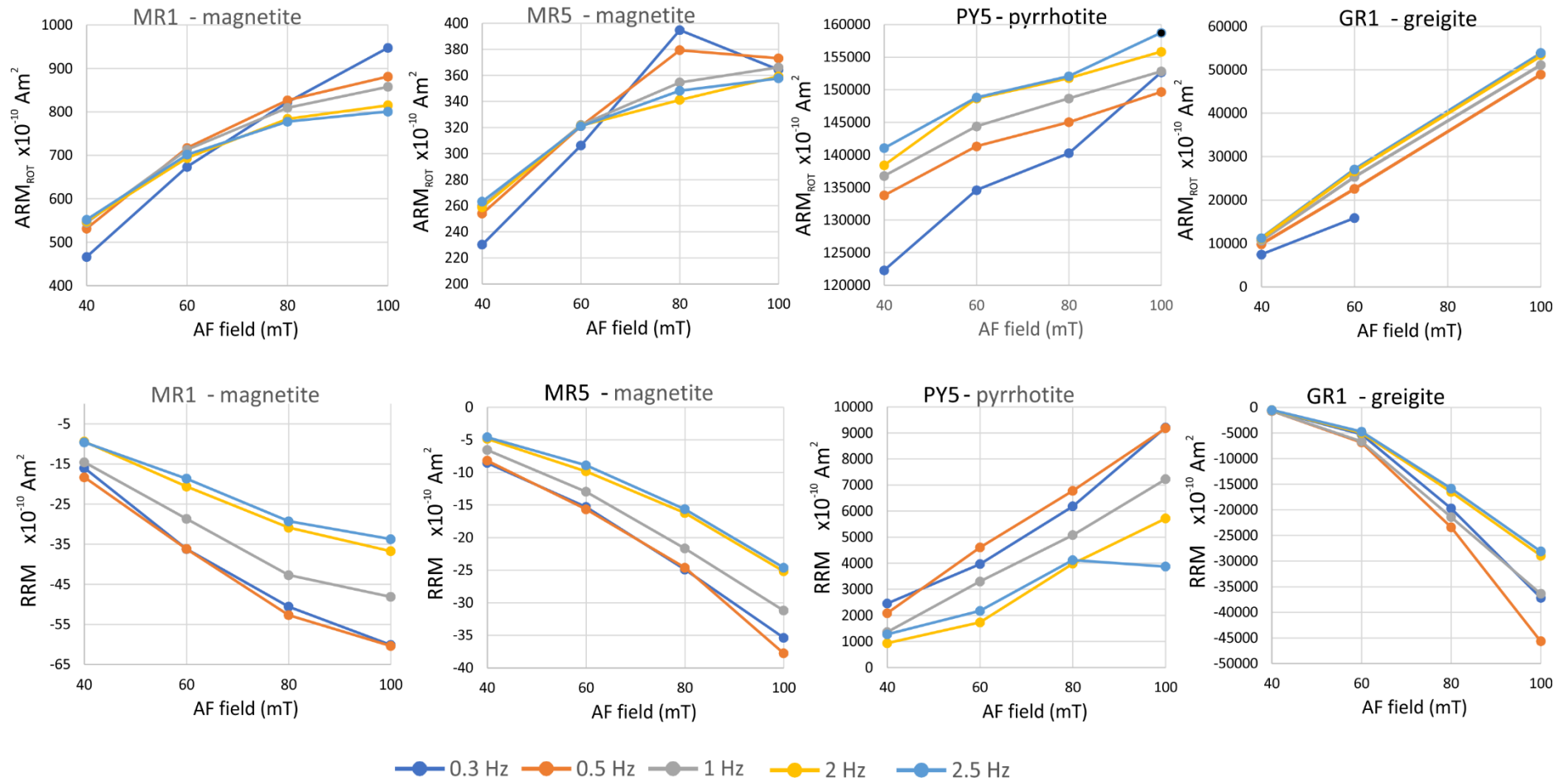


Fig. S16. Variation of RRM and ARM_{ROT} acquisition with AF field intensity for four test samples. Broadly the acquisition processes are near linear for fields between 40 and 100 mT, with a rather closer approach to saturation of the ARM_{ROT} for the two magnetite-bearing samples (T_H= 92 ms). Data is missing for some steps due to sample-drops during rotation.

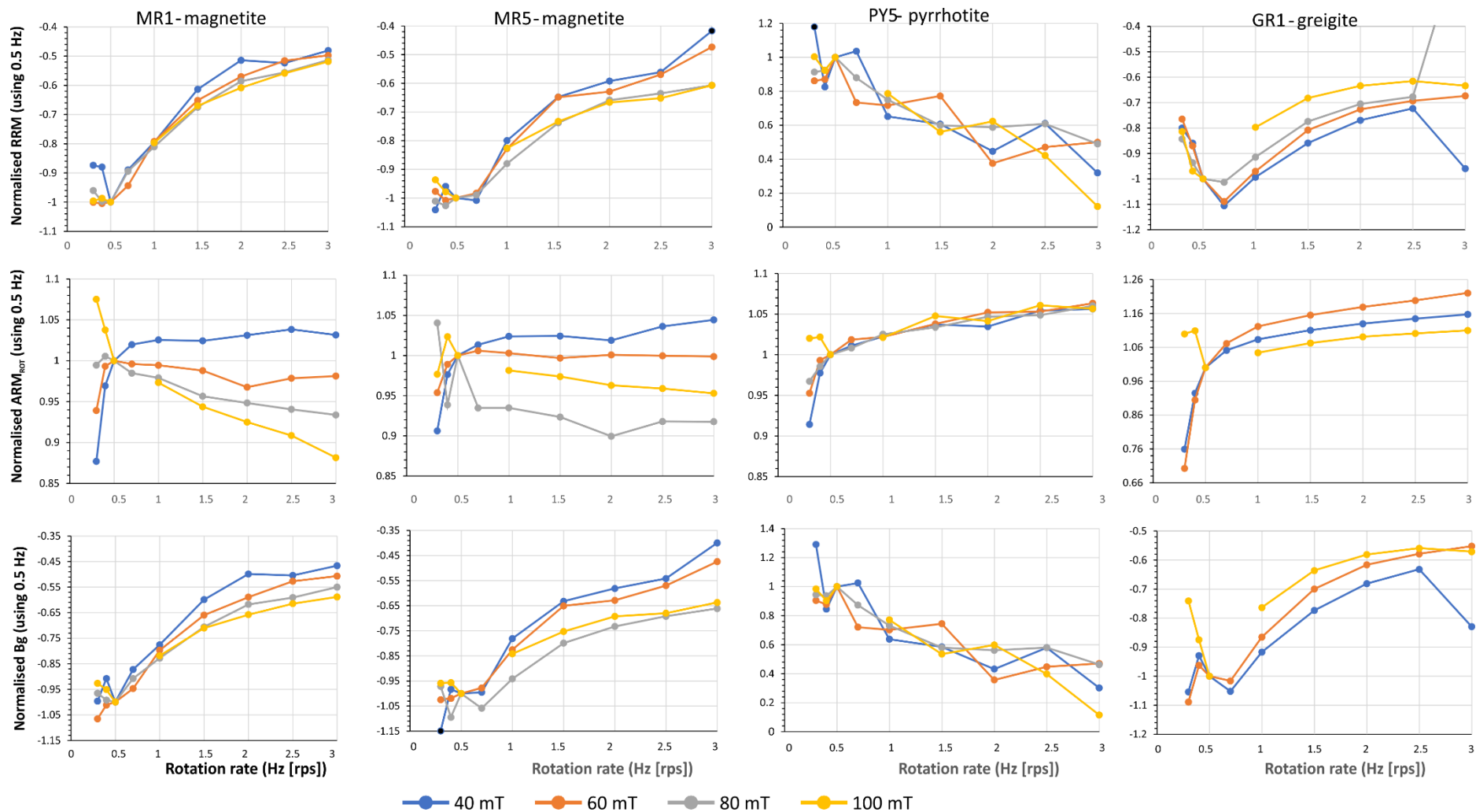


Fig. S17. Variation of normalised RRM, ARM_{rot} and B_g with respect to rotation rates. In each case normalised with respect to the value at 0.5 Hz [rps]. The four columns of graphs apply to each of the samples indicated at the top, and each row of graphs relates to the parameter show on the left ($T_H = 92$ ms).

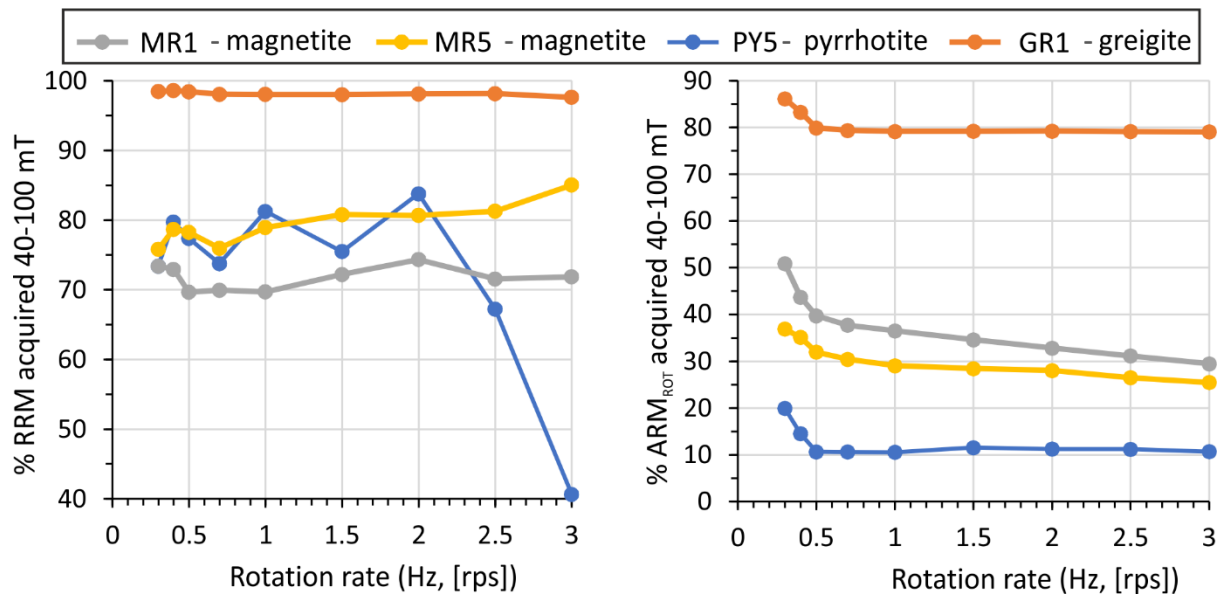


Fig.S18. The percentage of RRM and ARM_{ROT} acquired between 40-100mT with respect to the rotation rate. The differing percentages here represent the ability of the RRM and ARM_{ROT} to be acquired ($T_H = 92$ ms).

3.4 The RRM and ARM_{ROT} acquisition process with changes to the peak AF hold times.

The data in this section displays the impact of changing the hold time of the maximum AF field, to either have incomplete rotation initialisation (92 ms, 30 cycles on RAPID), adequate rotation initialisation (0.917 seconds, 300 cycles on RAPID) at about $\omega T_D = 0.4$ rev, and full rotation initialisation (9.17 seconds, 3000 cycles) across all rotation rates used.

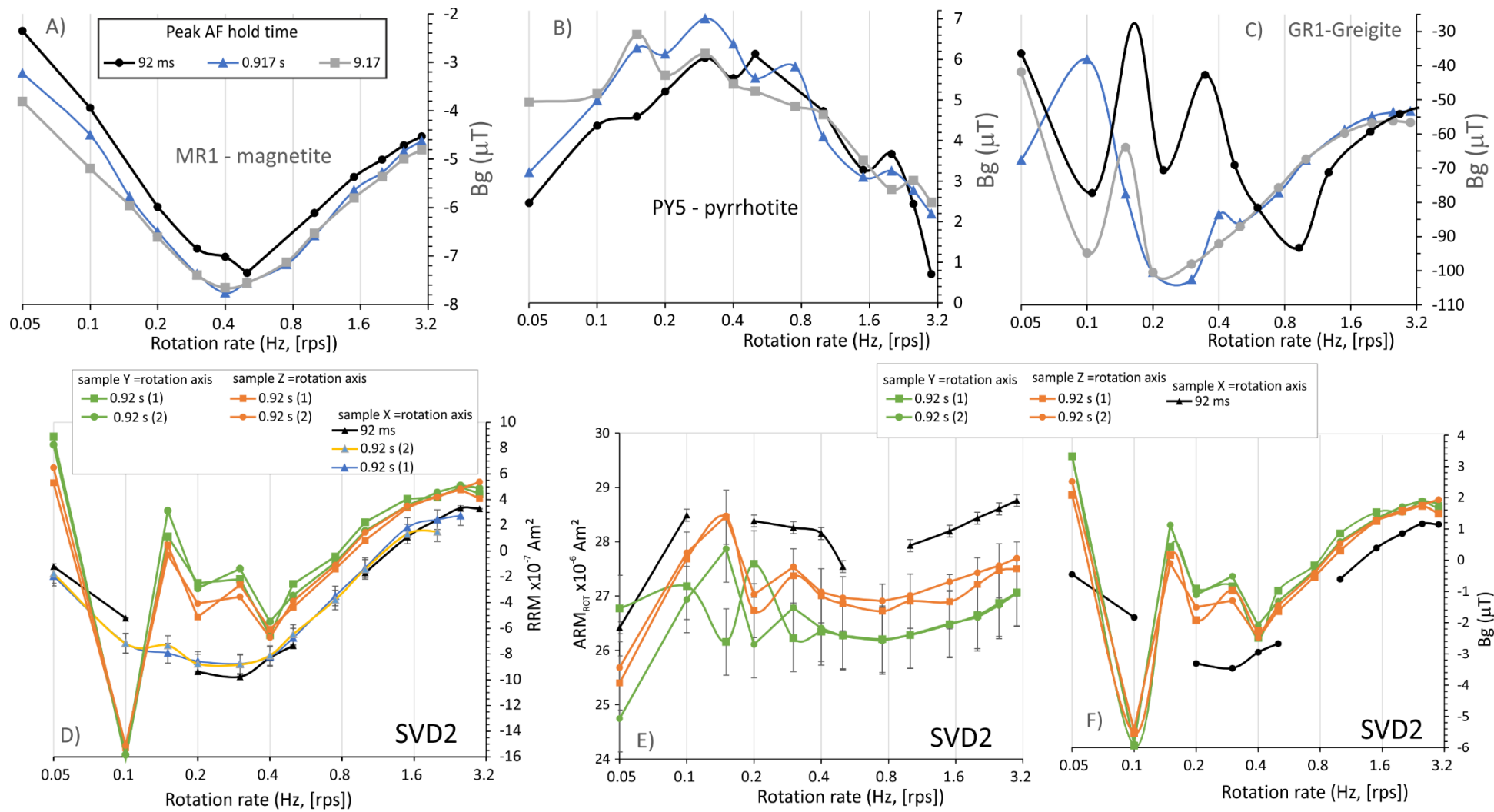


Fig. S19. A,B,C) The variation of Bg with rotation rate for the three tested values of peak AF hold times. Key to symbols and colours used in A). The 92 ms curve is the normal hold-time setting for most data reported here. A) For MR1 (magnetite) the 92 ms data is approximately 96% of the larger values shown by the data for the longer hold times. B) for PY5 (pyrrhotite) the data is rather noisy and the 92 ms dataset is rather similar to the longer hold times between ~0.4- 3 Hz [rps], but diverges below this. C) The greigite sample (GR1) displays large differences in Bg

for 92 ms, but the maximum is clearly around 0.2-0.3 Hz [rps] for the longer hold times, which for the 0.917 s hold time achieve the full 90° initialisation rotation by around 0.3 Hz [rps]. The large deviations in greigite are likely caused by large anisotropy in this sample which affects Bg at ω values below the rotation initialisation threshold. D,E,F) RRM. ARM_{ROT} and Bg data for dolerite sample SVD2 at the two smaller hold times versus rotation rate, and with different sample axes parallel to the spin vector (X= sample x-axis parallel to rotation axis etc). The sample is from the margin of near horizontal dolerite sill, and the X-Z plane is the surface approximately parallel to the margin, the Y-axis is near normal to the margin. This sample had been exposed to a 1T IRM between the measurements at 92 ms and 917 ms (responsible for the larger ZSD error bars on the 917 ms measurements, whereas the 92 ms measurements have error bars smaller than the symbols). D) Like the magnetite and basaltic samples studied by Edwards this sample (when spin vector along sample X-axis) has a peak of RRM (using 917 ms hold time) of ωT_D between 0.3- 0.45 rev (i.e., 0.2-0.3 Hz [rps] in the scale shown). E) corresponding change in ARM_{ROT} which like D) display differences between the axis rotated about, likely due to anisotropy. F) the corresponding changes in Bg. Although we have not independently confirmed the ferrimagnetic anisotropy (Potter, 2004) the curve showing the (negative) maximum in Bg with ω is likely that measured such that the rotation axis is near parallel to the maximum anisotropy, possibly represented by an ellipsoid with rather similar minimum and intermediate anisotropy axes, which is why the RRM and Bg along the sample Z and Y axes are similar. A few data points are missing due to sample non-pickup during some tests.

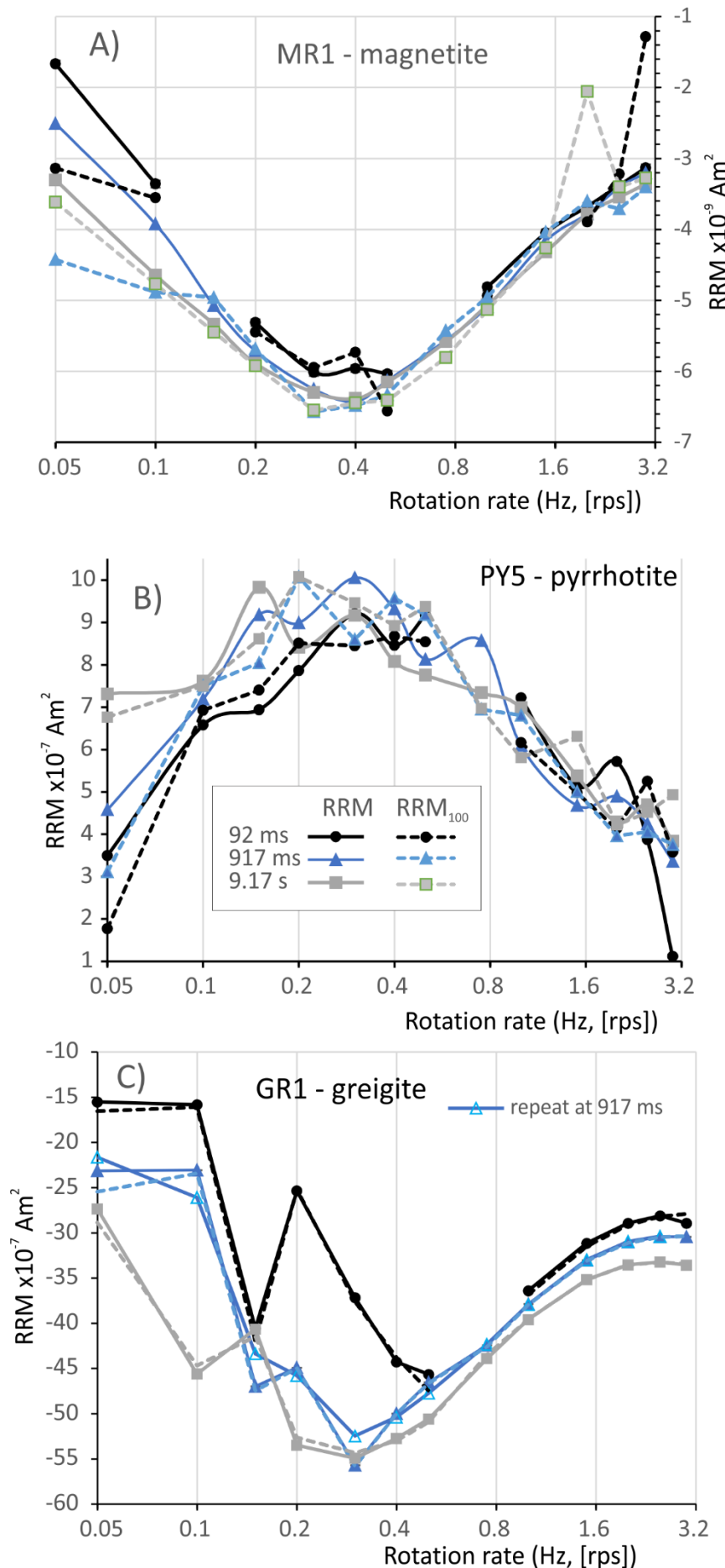


Fig. S20. Data for RRM and RRM₁₀₀ with respect to rotation rate for the three peak AF hold times tested. Key to symbols and colours used in B). Broadly the RRM₁₀₀ values (i.e., the RRM measured with a 100 μT DC bias field) track the RRM values acquired with no DC bias field. Like other pyrrhotite data the RRM₁₀₀ values are rather noisy in B), and noisy in A) due to weaker intensities. For the greigite sample (GR1) repeats for the 917 ms hold time suggest some additional 'RRM noise', since the measurement noise is smaller than the symbols used (likewise in B). This is perhaps because the sample was mounted differently with respect to the anisotropy axes (in plane normal to rotation axis) on each repeat (or it slipped during rotation).

4. A test of the AF peak hold time and field frequency

Some ambiguity about how to determine the duration of the peak field (T_H) during AF demagnetisation, is present in the RAPID software.

1. Indirectly, by reading the parameters "Total Ramp Time (ms)" and "Ramp Up Slope (in ms)" and "Ramp Down Slope (in ms)" (path: Main menu > Diagnostics > AF Demagnetizer > AF Demag Window) when running the AF field in diagnostics mode in the 'AF demag control' window
2. Directly, from the settable parameter D , "Duration in Sine Wave Periods at the Peak Field" (path: Main menu > View > Settings > AF Demag (2) tab) which controls overall characteristics of the demagnetiser. However, varying the parameter D does not affect the readings of "Total Ramp time" and "Ramp Up" and "Ramp Down" time as in 1.

A simple test determined that T_H is governed by D . Hence, to test the relationship between D , the AF field frequency and the time of a demagnetisation cycles, we did the following.

- a) Four low AFz (axial) AF fields (between 10 to 30mT) were applied one after another, without any measurements in between.
- b) The total duration of three concatenated AF demagnetization cycles was timed at seven settings of D . These were 30, 300, 600, 900, 1200, 1500, and 1800 sine-wave cycles.
- c) Each *AF demagnetization cycle* included lowering of the quartz sampling rod to the AFz coil, then the actual AF demagnetization and, finally, the raising of the sampling rod to the starting position.

Figure S21 shows that the lowering and the raising of the sampling rod takes 14.73 ± 0.21 s on average, whilst an increase in D by 1000 since waves increases T_H by 2.687 ± 0.19 s on average (uncertainties here are 95% confidence intervals). This corresponds to a frequency of the AFz coil of 372 Hz (95% confidence interval 347-401 Hz) which is close to the 360 Hz frequency indicated in the RAPID software. The conclusion is the hold times and field frequencies seem consistent with the settings in the software.

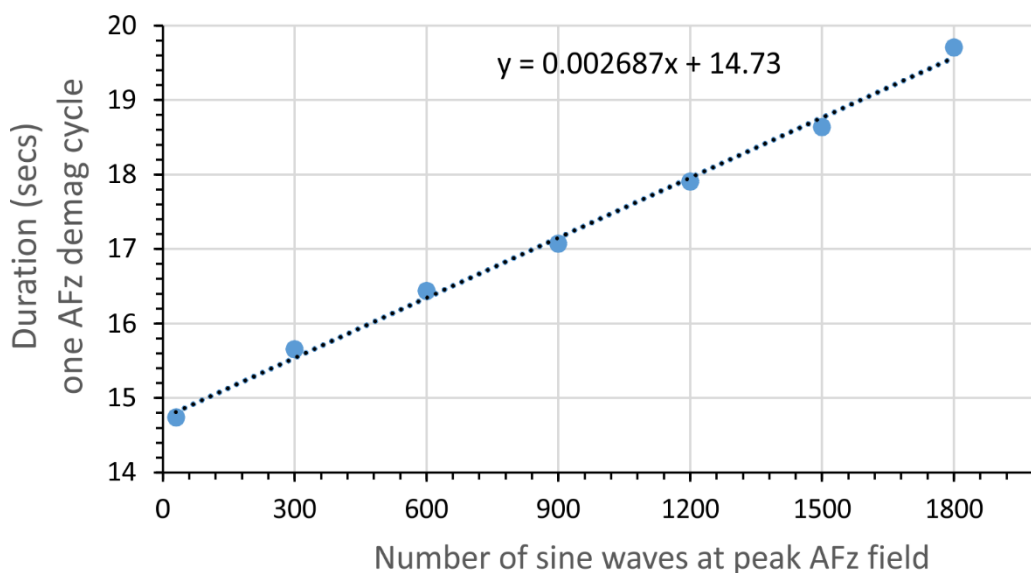


Fig. S21. The data for the test of the T_H and field frequency. The x-axis is the parameter D set in the RAPID software. The Y-axis is the average duration of one *AF demagnetization cycle* determined as above.

Supplementary References

- Hounslow, M.W., 1996. Ferrimagnetic Cr and Mn spinels in sediments: residual magnetic minerals after diagenetic dissolution. *Geophysical research letters*, **23**, 2823-2826.
- Hounslow, M.W. & Maher, B.A., 1996. Quantitative extraction and analysis of carriers of magnetization in sediments. *Geophysical Journal International*, **124**, 57-74.
- Hounslow, M.W. & Maher, B.A., 1999a. Laboratory procedures for quantitative extraction and analysis of magnetic minerals from sediments, in *Environmental magnetism, a practical guide*. pp. 139-164, eds. Walden, J., Oldfield, F., Smith, J. Quaternary Research Association, Technical Guide No. 6.
- Hounslow, M.W. & Maher, B.A., 1999b. Source of the climate signal recorded by magnetic susceptibility variations in Indian Ocean sediments. *Journal of Geophysical Research: Solid Earth*, **104**, 5047-5061.
- Hounslow, M.W. & Morton, A.C., 2004. Evaluation of sediment provenance using magnetic mineral inclusions in clastic silicates: comparison with heavy mineral analysis. *Sedimentary Geology*, **171**, 13-36.
- Hounslow, M.W., Maher, B.A. & Thistlewood, L., 1995. Magnetic mineralogy of sandstones from the Lunde Formation (late Triassic), northern North Sea, UK: origin of the palaeomagnetic signal. in *Application of palaeomagnetism to the oil industry*, pp. 119-147, eds. Turner, A. & Turner, P. *Geological Society, London, Special Publications*, **98**.
- Kopp, R.E. & Kirschvink, J.L., 2008. The identification and biogeochemical interpretation of fossil magnetotactic bacteria. *Earth-Science Reviews*, **86**, 42-61.
- Maher, B.A. & Hounslow, M.W., 1999. The significance of magnetotactic bacteria for the palaeomagnetic and rock magnetic record of Quaternary sediments and soils. In: Tarling, D.H & Turner, P. eds, *Palaeomagnetism and diagenesis in sediments*. *Geological Society, London, Special Publications*, **151**, 43-46.
- Maher, B.A., Thompson, R., Hounslow, M.W. 1999. Introduction. in: Maher, B.A. and Thompson, R. eds., 1999. *Quaternary climates, environments and magnetism*. Cambridge University Press.
- Martínez-Ruiz, F., Paytan, A., Gonzalez-Muñoz, M.T., Jroundi, F., Abad, M.D.M., Lam, P.J., Bishop, J.K.B., Horner, T.J., Morton, P.L. & Kastner, M., 2019. Barite formation in the ocean: Origin of amorphous and crystalline precipitates. *Chemical Geology*, **511**, 441-451.
- Montgomery, P., Hailwood, E.A., Gale, A.S. & Burnett, J.A., 1998. The magnetostratigraphy of Coniacian-Late Campanian chalk sequences in southern England. *Earth and Planetary Science Letters*, **156**, 209-224.
- Özdemir, Ö. & Dunlop, D.J., 2010. Hallmarks of magnetization in low-temperature remanence cycling of partially oxidized magnetite nanoparticles. *Journal of Geophysical Research: Solid Earth*, **115**, doi.org/10.1029/2009JB006756.
- Potter, D.K. & Stephenson, A., 1986. The detection of fine particles of magnetite using anhysteretic and rotational remanent magnetizations. *Geophysical Journal International*, **87**, 569-582.
- Potter, D.K., 2004. A comparison of anisotropy of magnetic remanence methods—a user's guide for application to palaeomagnetism and magnetic fabric studies. In: Martin-Hernandez, F.,

Luneburg, C. M., Aubourg, C. & Jackson, M. (eds) 2004. *Magnetic Fabric: Methods and Applications*. Geological Society, London, Special Publications, 238, pp.21-35.

Readman, P.W. & O'Reilly, W., 1972. Magnetic properties of oxidized (cation-deficient) titanomagnetites (Fe, Ti, x) Fe_3O_4 . *Journal of geomagnetism and geoelectricity*, **24**, 69-90.

Snowball, I.F., 1997. The detection of single-domain greigite (Fe_3S_4) using rotational remanent magnetization (RRM) and the effective gyro field (B_g): mineral magnetic and palaeomagnetic applications. *Geophysical Journal International*, **130**, 704-716.

Wilson, R.L. & Lomax, R., 1972. Magnetic remanence related to slow rotation of ferromagnetic material in alternating magnetic fields. *Geophysical Journal International*, **30**, 295-303

This sheet contains test samples against rps

Paper sample code	native sample code	0.05	0.1	0.15	0.2	0.3
df3	2h34.4	-32.9	-28.9		-63.8	-86.5
df5c	116.45	21.6	-36.9		-10.2	-5.5
df5d	172.32	-89.3	-170.6		-290.5	-299.7
df6	BL18.4	-11.9	-23.4		-38.2	-42.9
svd1	BO32	-51889.0	-86191.8		-151256.7	-174234.9
df1	BO37	-17.7	-35.5		-57.9	-60.7
svd2	BO58	-1204.6	-5213.7		-9380.1	-9771.8
cc2	CC9b-0m b	-0.1	-0.1		-0.2	-0.2
cc1	CCH5	-0.3	-0.5		-1.3	-1.3
df2	DH4-42	-10.6	-22.1		-36.4	-38.7
df4	HO22.3	-45.7	-14.8		-54.8	-96.4
lud	ME2	-4.3	-7.4		-11.2	-11.7
or2	ME6	-11.2	-16.4		-27.4	-29.4
or3	ME9	-3.9	-4.0		-11.3	-11.4
mr1	ME13	-16.7	-33.6		-53.1	-60.2
mr2	ME14	0.1	-0.3		-0.3	-0.3
mr5	ME17	-9.0	-17.6		-30.2	-35.4
df5	WI22.4	-12.5	-37.3		-50.3	-54.9
py1	ch1	-10.1	2.3	-18.9	-1.1	-17.2
py2	ch2	-130.6	-155.9	-234.2	-146.6	-93.6
py3	ch3	-574	-895	-801	-969	-578
py4	ch4	835	1193	2123	2185	3059
py5	ch5	3492	6576	6936	7857	9205
py6	ch6	259	1502	1405	2294	1637
py7	ch7	484	2826	4120	6160	5191
py8	ch8	469	73	74	-381	-87
py9	ch9	-277	1848	205	1498	1293
gr1	ch10	-15525	-15831	-40573	-25362	-37183
gr2	ch11	-3601	-5230	-9330	-8254	-11265
gr3	ch12	-5297	-6700	-13715	-10943	-15785
gr4	ch13	-5640	-7093	-14214	-11117	-15286

all values on sheet in $\times 10^{-10} \text{ Am}^2$ unless otherwise shown

RRM with rps $\times 10^{-10} \text{ Am}^2$						RRM-SD		
0.4	0.5	1	1.5	2	2.5	3 (measured)	rps=0.3	
-85.7	-80.1	-53.6	-41.6	-31.4	-26.0	-26.6	0.28	-5.5
-24.0	-27.1	-28.0	-1.0	4.2	8.4	-3.8	0.55	-0.3
-282.2	-265.0	-171.8	-128.8	-102.4	-88.3	-82.9	0.47	-16.1
-43.9	-43.5	-29.5	-18.1	-12.2	-9.3	-6.0	0.38	-2.7
-172509.8	-159263.8	-101299.5	-71459.5	-56530.2	-48626.3	-42242.7	98.38	-28.1
-65.1	-59.0	-42.7	-30.6	-24.0	-23.5	-18.4	0.11	-3.7
-8292.3	-7358.9	-1686.7	1095.8	2429.4	3334.5	3283.7	39.54	-3.5
-0.4	-0.3	-0.2	-0.2	-0.4	-0.2	0.2	0.02	-0.3
-1.3	-1.5	-1.3	-1.0	-0.9	-1.0	-1.0	1.38	-0.7
-37.2	-38.0	-27.0	-20.2	-13.6	-11.4	-10.4	0.29	-2.6
-103.6	-92.8	-62.3	-43.3	-37.2	-32.4	-27.4	0.28	-5.2
-10.6	-10.2	-7.2	-5.7	-5.3	-3.8	-3.4	0.03	-8.8
-25.9	-28.2	-22.5	-16.5	-11.9	-13.2	-9.5	2.21	-6.9
-14.8	-3.8	-3.3	-6.5	-0.7	-1.0	-0.6	2.21	-4.1
-59.6	-60.4	-48.1	-40.5	-36.8	-33.8	-31.3	0.51	-6.4
-0.1	-0.5	-0.2	0.1	-0.7	0.1	0.1	0.03	-2.3
-37.0	-37.8	-31.2	-27.7	-25.2	-24.6	-22.9	0.46	-9.7
-54.4	-51.3	-32.3	-22.1	-17.4	-14.8	-11.1	0.52	-2.9
1.4	0.0	18.9	26.3	0.5	24.0	-10.4	3.17	-6.2
-45.6	61.6	112.8	194.8	107.8	165.7	15.4	11	-3.1
-288	319	1016	1280	920	1080	-13	22	-2.3
2509	2430	1828	1882	1973	1996	-261	25	5.1
8460	9177	7218	5140	5713	3868	1116	26	6.0
1248	1172	815	372	911	-269	899	19	2.6
5819	6034	3759	3546	1790	1357	-843	26	5.2
35	33	397	472	287	107	-215	13	0.8
891	1458	1222	1027	58	155	513	22	1.9
-44286	-45663	-36401	-31151	-28948	-28115	-28940	87	-69.1
-12208	-12431	-9839	-8435	-7856	-7687	-7968	31	-67.0
-17377	-17695	-14106	-12195	-11486	-11174	-11707	54	-71.4
-17602	-18222	-13882	-11812	-10880	-10424	-10833	19	-78.1

selected Bg values (μT)								
rps=0.4	rps=0.5	rps=2.5	ARM _{TRANS}	0.05	0.1	0.15	0.2	0.3
-5.6	-5.7	-2.2		1526	1680		1616	1581
-1.4	-1.7	0.7	1766	1761	1910		1827	1784
-15.9	-15.8	-6.0	1661	1738	1971		1914	1865
-2.9	-3.1	-0.8	1501	1545	1683		1656	1599
-27.5	-26.1	-7.3	486038	494882	625387		618961	619066
-4.3	-4.1	-2.0	1322	1587	1736		1694	1639
-2.9	-2.7	1.2	254479	264175	284880		283822	282583
-0.6	-0.5	-0.4	66	68	70		69	67
-0.7	-0.9	-0.8	180	183	197		196	191
-2.6	-2.9	-1.0	1466	1494	1620		1582	1519
-5.8	-5.5	-2.3	1841	1825	2030		1918	1869
-8.1	-7.9	-2.9	113	119	133		133	132
-6.2	-6.9	-3.2	393	399	426		425	425
-5.3	-1.3	-0.4	238	262	281		281	280
-6.5	-6.9	-4.2	862	899	976		968	947
-1.0	-4.7	0.7	10.2	10.1	11.3		11.3	11.3
-9.7	-10.1	-6.9	360	359	390		392	364
-3.1	-3.0	-1.0	1777	1810	1992		1957	1894
-0.4	-0.9	9.6	145	49	188	195	207	197
-1.4	0.7	4.2	2084	1882	3108	3274	3409	3346
-0.9	1.4	4.4	14908	14960	19663	20083	20085	20700
4.1	4.1	3.1	50056	52781	59458	59842	59147	59730
5.5	6.1	2.4	136024	142020	150755	151122	150964	152641
1.8	2.1	0.2	56659	57111	62023	61763	61756	61408
5.0	5.2	2.2	107287	110476	114050	113893	118693	115346
0.1	0.5	0.3	26842	29235	28011	28752	28780	28629
1.3	1.5	1.1	93880	85039	94258	94270	88225	90815
-81.6	-93.3	-52.2	51689	42534	57224	57438	59321	53790
-73.7	-83.6	-45.2	12091	11598	17757	17499	18266	16813
-81.6	-91.0	-49.1	14858	12800	26034	22590	24985	22108
-93.9	-107.4	-53.0	9156	12315	23372	19721	22546	19575

ARM_{ROT}						ARM_Z		
x10⁻¹⁰ Am²						x10⁻¹⁰ am²	d.ARM_{40mT}	
0.4	0.5	1	1.5	2	2.5	3	(ratio)	
1520	1414	1333	1257	1122	1160		3024.1	0.419
1662	1557	1455	1361	1249	1207	1198	3846.2	0.374
1774	1682	1610	1536	1498	1470	1454	3348.4	0.508
1525	1424	1335	1249	1087	1155		3108.0	0.482
626352	610681	638798	655569		662514		650972	0.528
1530	1453	1358	1270	1224	1185	1158	3137.8	0.494
281520	275433	279307	281944	284334	286060	287589	225724	0.190
63	60	56	51		42		143.4	0.511
179	168	154	138	127	120	114	437.9	0.685
1436	1326	1237	1148		1084		3036.3	0.500
1786	1680	1586	1496	1442	1404	1377	3762.9	0.407
131	129	129	129	129	130	129	159.5	0.403
417	409	412	410	406	406	404	478.8	0.331
281	287	287	265	269	277	279	355.6	0.395
914	881	857	832	815	800	777	1303.8	0.473
10.9	10.3	10.3	10.6	10.8	11.8	9.8	12.8	0.353
382	373	366	363	359	358	356	563.1	0.428
1779	1692	1590	1499		1414		3629.9	0.468
211	194	196	222	230	226	233	170.3	0.523
3363	3263	3452	3636	3729	3772	3859	2268	0.578
20805	19721	21241	21469	21858	22215	21936	12990	0.366
60850	59988	60820	62417	62705	63531	65234	41170	0.125
152882	149646	152800	156757	155821	158719	158088	112910	0.083
62741	61623	62980	63923	64184	65262	64707	44355	0.081
115085	114646	116793	121597	121190	123719	123291	76663	0.100
28477	28361	28995	28802	28667	28925	29763	18986	0.027
92682	90458	93404	92601	93587	94862	95688	66607	0.036
54264	48918	51068	52465	53378	53865	54292	49035	0.824
16560	14863	16030	16498	16790	17020	17222	15445	0.809
21307	19437	21469	22005	22446	22753		21284	0.814
18746	16969	18508	19075	19333	19682		17261	0.849

MDF (mT)	mass (g)	SIRM $\times 10^{-8} \text{ Am}^2$	paper sample code	Selected mass specific values ($\times 10^{-7} \text{ A}$)			
				RRM		ARM _{ROT}	
				rps=0.5	rps=2.5	rps=0.5	rps=2.5
34.8	19.87	488.9	df3	-4.030	-1.307	71.1	58.4
32.1	20.72	474.5	df5c	-1.309	0.404	75.2	58.2
40.6	22.59	827.8	df5d	-11.73	-3.91	74.5	65.1
38.8	20.68	464	df6	-2.106	-0.450	68.9	55.8
41.8	26.97	822681	svd1	-5905	-1803	22643	24565
39.6	21.30	534.6	df1	-2.77	-1.10	68	56
16.3	26.10	152897	svd2	-282.0	127.8	10553	10960
40.6	27.26	7.7	cc2	-0.011	-0.006	2.20	1.56
50.5	22.51	35.7	cc1	-0.068	-0.043	7.45	5.32
40.0	31.58	442.7	df2	-1.202	-0.360	42.0	34.3
34.5	22.67	535.8	df4	-4.092	-1.430	74.1	61.9
33.5	0.02260	174.3	luc	-451.0	-169.5	5709	5760
27.4	0.02660	573.4	or2	-1061.9	-495.0	15358	15254
28.0	0.02760	205	or3	-138.17	-36.40	10389	10042
38.4	0.02010	836	mr1	-3005	-1679	43835	39824
26.6	0.00600	8.8	mr2	-81.17	14.54	1718	1958
34.9	0.00034	453	mr5	-110792	-72249	1093991	1048959
37.9	23.66	624.2	df5	-2.169	-0.625	71.5	59.8
41.2	0.22		py1	-0.11	109.18	882	1027
46.0	0.33		py2	186.7	502.1	9889	11431
32.9	0.49		py3	651	2204	40247	45336
17.7	0.40		py4	6075	4990	149971	158827
14.6	0.64		py5	14339	6044	233821	247999
13.4	7.57		py6	154.88	-35.59	8146	8627
11.1	7.43		py7	812.07	182.69	15430	16651
12.4	8.28		py8	3.97	12.91	3425	3493
11.3	5.88		py9	248.16	26.41	15397	16147
63.9	23.24		gr1	-1965	-1210	2105	2318
66.2	22.29		gr2	-557.7	-344.9	667	764
65.9	22.48		gr3	-787.1	-497.1	865	1012
67.1	21.42		gr4	-850.7	-486.7	792	919

m^2/Kg

ARMz

SIRM (1T)

152	2460
186	2290
148	3664
150	2244
24137	3050356
147	2510
8648	585812
5.26	28.2
19.45	159
96.1	1402
166	2363
7057	771239
18001	2155639
12885	742754
64867	4159204
2132	146667
1651177	132844575
153	2638
774	
6874	
26511	
102926	
176422	
5863	
10318	
2293	
11337	
2110	
693	
947	
806	

This sheet contains the RRM and GRMz demagnetisation data using method 2

all values on sheet in $\times 10^{-10} \text{ Am}^2$ unless otherwise shown

paper	native	mid point between +- RRM					
		RRM (rps=0.5)	RRM(rps=2.5)	NRM-zero (z=150 mt)		RRM- zero (Rz)	GRMzero (Gzz)
code	sample						
DF3C	2H_10.4	4.385	2.7265	-0.87	5.87	20.299	-35.962
DF3B	2H-14.4	1.586	-4.1285	-7.26	13.96	1.214	-30.981
DF5B	142.68	2.886	2.2455	-4.02	7.97	4.431	-16.132
DF6B	BL16.2	2.322	2.7	-9.27	5.17	15.855	-19.471
DF1B	BO39	7.1725	6.752	-11.96	16.74	-0.637	-14.084
SVD2	BO58	458	82	-19.80	986.7	1668.8	-491.0
CC1B	CCH16.9	0.662	0.675	-0.06	0.54	0.345	-0.343
DF4B	HO28b.4	6.703	4.862	-11.30	13.37	-10.990	-40.830
DF4C	HO29.3	0.0515	0.039	0.05	0.14	-0.283	0.103
MR1	ME13	-1.2075	0.498	-10.52	5.83	1.903	-22.322
MR5	ME17	6.8605	7.561	1.92	2.35	-5.637	3.277
PY5	CH5-Pyrr	583	875	1010	1719	3885	-790
PY7B	CH7B-phyll	741	934	152	2854	3064	6611
GR1	CH10-Greig	-2055	1765	679	985	-2260	2339

RRM0= initial RRM value before demag (from both + and - RRM measurement)

RRM from Rz' is RRM demag tail to initial value (alternative estimate of RRM at respective r_p)

Rz is the baseline zero for the RRM demag curve based on assessment of decay curves

Gzz is the baseline zero for the GRMz demag curve based on assessment of acquisition curves

estimates of 'zeros' from the raw data (not using the demag data)

for rps=0.5

RRMO	RRMO SD	GRMz Tail	RRM	New Est.				
		SD	(from Rz)	RRMO	AFO	AF10	AF20	AF30
-36.505	3.487	6.866	-49.078		-98.1557	-95.7477	-85.8857	-65.4457
-26.666	3.679	5.876	-29.414	-58.8273	-59.6873	-57.9673	-50.1373	-27.6923
-40.719	2.536	3.950	-44.694		-89.3875	-89.1625	-83.6975	-74.6165
-51.510	0.403	4.327	-59.654		-119.307	-116.298	-101.27	-84.595
-48.601	0.822	3.661	-48.819		-97.6372	-93.6162	-79.4692	-59.3852
-7754.5	696.4	384.8	-8117.4		-16235	-14816	-11731	-9460
-0.385	0.220	0.077	-0.574		-1.1475	-1.0525	-1.0775	-1.0645
-92.038	3.931	4.262	-89.538	-179.076	-178.44	-179.711	-167.272	-125.6
-0.036	0.089	0.039	0.291	0.5815	0.0935	0.5815	0.3795	0.1715
-60.223	1.315	3.143	-60.563		-121.127	-117.405	-102.62	-86.3968
-36.986	0.998	3.152	-34.560		-69.1193	-67.3813	-61.2143	-53.8533
7921	176	1471	6100	12200	11740	12607	12252	9793
8016	4724	1353	5519	11038	6336	7428	13901	11785
-46755	308	1165	-45782		-91563	-91534	-90719	-88174

the above a

better estimate
of starting value
sometimes

os)

ve

0.5 rps RRM-demag ($\times 10^{-10} \text{ Am}^2$) [range RRM0 to Rz]- this is 2x R0

AF40	AF50	AF60	AF70	AF80	AF90	AF100	AF110	AF120
-47.4747	-37.0697	-36.8407	-30.1267	-20.0937	8.480333	-2.21867	-6.26167	-29.1677
-26.5183	-18.1033	-21.1782	-22.8943	-29.2693	-7.37225	-18.6993	19.02275	-4.93725
-60.0945	-41.9515	-26.1855	-17.1565	-14.4075	-11.4615	-2.8405	-7.0525	2.1745
-62.351	-43.176	-27.33	-24.676	-7.285	-2.99	-0.002	-12.506	-0.352
-36.9252	-16.8682	-5.3962	-5.8532	-16.8402	4.3718	-5.0072	8.0118	-8.6202
-5633	-3824	-2872	-1964	78	-560	104	-473	1056
-1.3275	-1.7455	-0.6475	-0.7985	-0.5855	-0.4305	0.3075	-0.3075	-0.5355
-77.2364	-42.0454	-11.1404	-0.7734	-7.5674	-13.1454	6.6856	14.8006	-1.8594
0.0775	0.0425	0.1335	0.0155	-0.0155	0.2435	-0.1175	0.3205	0.2215
-61.8718	-57.0598	-33.9398	-23.4328	-22.3868	-15.6658	-14.5068	8.4542	-12.0608
-44.9033	-37.6503	-29.5213	-21.4123	-17.5833	-11.7313	-9.04433	-3.89333	-4.85133
8211	4309	5885	4299	3205	1048	-576	811	391
9924	7976	6829	5681	1720	3865	213	-4839	1010
-82008	-71193	-55105	-37333	-23332	-14576	-9077	-5380	-3295

are corrected to the base-line zero level (the Rz value)

			GRMz (from GRMzz)					
			mT					
			MDF RRM (rps=0.5)	New Est GRMz-0	AFO	AF10	AF20	AF30
AF130	AF140	AF150						
-12.0397	-30.6867	-20.9417	40.63	41.56	39.88	41.20	43.58	42.02
3.13275	0.05175	1.75275	33.58	29.71	29.01	29.49	30.62	31.45
-4.7045	-0.0735	2.6035	48.85	18.77	18.39	18.42	19.49	18.97
0.354	-12.73	-16.503	41.79	24.88	23.68	24.31	26.63	27.23
1.2438	-16.1912	-3.4732	34.59	27.70	27.36	28.04	25.33	25.11
-348	67	76	32.65	2376	2349.18	2401.92	1658.08	2629.22
-1.3215	-0.8615	-1.4945	75.09	1.62	1.63	1.67	1.55	1.32
-14.1514	-16.7654	-3.0754	38.12	49.43	48.88	49.98	49.29	46.62
-0.0015	0.2015	-0.0575	25.11	-0.16	-0.12	-0.21	-0.01	-0.20
2.6122	-4.8088	5.8032	44.56	21.54	21.13	21.95	21.68	20.10
1.074667	-2.04733	0.972667	53.49	9.97	9.66	9.82	10.42	6.81
-441	-402	452	52.23	1754	1739.21	1769.57	517.13	1747.89
-1357	654	-307	68.34	-9417	-11761.73	-7490.50	-8999.05	-8675.76
-2111	-525	525	65	-6832	-6762	-6716	-6802	-6946

the above are corrected to the base-line zero

better estimate
of starting value
sometimes

0.5 rps GRMz-demag (x10⁻¹⁰ Am²) [range GRMz0 to GRMzz)- this is (2x GRMZ)

AF40	AF50	AF60	AF70	AF80	AF90	AF100	AF110	AF120
42.10	35.24	18.77	15.71	-15.71	31.96	41.76	24.72	11.99
16.21	22.80	3.99	7.04	10.14	3.33	10.01	0.00	6.52
18.59	16.41	16.72	13.75	13.56	14.62	8.05	8.10	-0.37
20.87	20.81	23.04	24.80	8.66	5.66	0.00	11.56	5.43
26.34	27.57	26.85	20.07	20.22	12.04	-1.90	23.63	5.03
3112.70	479.97	1378.31	2793.13	712.07	864.47	829.18	-480.14	257.32
0.99	-0.11	0.11	0.19	0.21	0.48	-0.03	0.47	0.63
42.12	42.71	40.51	33.69	16.61	14.72	34.45	29.81	-4.38
-0.16	-0.23	-0.25	-0.26	-0.10	0.10	-0.18	-0.02	0.01
19.04	13.17	-3.08	15.36	12.28	15.15	9.09	5.16	-5.16
5.37	6.33	3.03	2.84	-1.75	3.52	8.57	5.62	1.29
-792.49	97.03	171.12	-268.15	871.87	157.59	2891.07	-1628.89	3141.09
-6026.42	-3377.08	-5139.23	-2763.41	2044.46	-6770.40	-2044.46	-6726.65	-9636.93
-6932	-6177	-4578	-2369	-887	-93	34	75	-298

level (the Gzz value)

			mT						
			MDF						
			GRMz	RRM- zero	GRMzero(RRM0(RRM0	RRM0	
AF130	AF140	AF150	(rps=0.5)	(Rz)	Gzz)	rps=2.5)	SD+SD	RRM0	(from Rz)
30.46	27.96	38.34	60.8	1.814	-3.1715	-13.3025	1.198737		-15.2455
17.56	10.29	-7.16	51.7	-7.7995	-20.501	-10.9005	4.105762		-9.45825
0.17	0.20	2.96	98.6	-4.6745	-6.1085	-18.1965	0.501902		-14.5878
12.61	12.96	-1.14	80.0	24.8925	-48.2545	-18.946	0.394286		-29.1788
1.82	-2.65	2.74	83.6	32.961	-66.408	-14.872	0.365338		-29.374
296.52	338.14	-411.84	85.6	2501	#N/A	2980	281		2097
0.84	0.02	0.54	41.1	0.834	-0.67633	-0.483	0.202192		-0.673
6.15	-1.77	14.21	76.6	5.536	9.4155	-43.565	1.376784		-25.3775
-0.24	0.03	-0.02	78.0	24.816	-24.732	-0.158	0.017839		-10.301
8.70	21.18	9.78	93.8	-27.4513	-16.668	-34.875	1.602971		-17.8233
8.15	3.22	0.46	51.8	-4.339	-3.293	-24.958	0.934328		-21.9045
1771.53	2211.91	2877.87	31.6	519	2100	2717	243		3788
-10937.37	-6070.81	-12080.48	52.8	1023	#N/A	3111	176		1776
-786	-482	-109	65	-2943	791	-28727	2747		-27139

for RPS=2.52.5 rps RRM-demag (x10⁻¹⁰ Am²) [range RRM0 to f

New Est

RRM-0	AFO	AF10	AF20	AF30	AF40	AF50	AF60	AF70
-30.6065	-30.491	-30.722	-26.971	-15.228	-5.454	-2.098	0	-5.469
	-18.9165	-17.6175	-12.8755	-4.8385	0.2035	-2.5505	-14.0775	-0.2035
-29.2075	-29.1755	-29.2395	-27.0755	-23.2455	-16.1475	-8.3675	-2.9515	0.1115
	-58.3575	-57.6705	-49.5645	-39.8125	-29.8075	-20.3035	-14.0555	-0.1495
-59.0815	-58.748	-59.415	-51.927	-40.685	-34.795	-29.353	-9.153	-10.935
	4195	4127	4991	4821	4254	3414	1004	1719
-1.367	-1.346	-1.388	-1.291	-1.229	-0.932	-1.23	-0.875	0.127
-51.396	-50.755	-52.037	-44.477	-31.177	4.044	-24.564	-24.039	-4.044
	-20.602	-19.45	-17.885	-12.766	-9.075	0	-7.789	-26.013
-36.5057	-35.6467	-37.3647	-34.4847	-17.7487	-10.1637	-4.09667	-12.2437	-0.27267
	-43.809	-42.347	-38.747	-35.314	-28.145	-23.155	-20.087	-18.805
	7282	7575	6988	8468	6726	6374	5707	2767
	5093	3553	6028	4158	7806	6128	2029	3173
	-54278	-54265	-53971	-52860	-50116	-44888	-36125	-25859

Rz)- this is 2x R0

mT

AF80	AF90	AF100	AF110	AF120	AF130	AF140	AF150	MDF RRM (Rps=2.5)
-9.544	-21.071						-14.777	29.12
-5.7305	-4.7065						11.5235	24.56
-3.3365	-0.1115						-5.9045	41.77
0.1495	-19.5435						16.1175	40.82
0	-21.872						-21.584	46.96
248	0						-2115	62
-0.127	-0.646						-1.326	55.74
-14.986	-41.357						-20.067	53.89
-26.801	-20.702						-16.095	35.53
0.647333	-0.37467						-10.4677	38.29
-10.973	-7.616						7.616	55.91
4153	4632	739	1457	1751	-1050	-102	1151	66
1566	4051	-494	2787	-4987	-1726	-328	2054	54
-16983	-10740	-5987	-3454	-1687	-919	241	677	69

GRMz
(from
GRMzz)

2.5 rps GRMz-demag (x10⁻¹⁰ Am²) [range GR

New Est

GRMz-0	AF0	AF10	AF20	AF30	AF40	AF50	AF60	
		10.70	9.52	9.77	10.91	12.99	5.98	8.65
17.25	17.16	17.35	16.68	20.61	16.50	14.56	0.00	
8.13	8.06	8.21	8.04	7.53	8.18	7.86	8.83	
49.87	49.23	50.51	48.37	49.03	49.87	47.29	34.80	
76.36	75.96	76.76	73.22	75.64	70.64	63.98	55.37	
1.55	1.57	1.53	1.54	1.45	1.26	0.83	-0.18	
-41.83	-41.60	-42.05	-34.96	-26.15	-23.14	3.37	-3.37	
	20.28	19.02	17.80	12.77	9.34	0.00	7.87	
12.26	11.01	13.50	12.80	9.36	11.18	4.16	5.31	
16.69	16.65	16.73	15.92	14.16	13.97	10.18	8.61	
-3169	-3011	-3328	-1807	-3474	-3727	-3120	-1177	
2507	2507	2507	2509	2495	2476	2494	2631	

(Mz0 to GRMzz)- this is (2x GRMZ)

AF70	AF80	AF90	AF100	AF110	AF120	AF130	AF140	AF150
3.11	-0.60	4.86						0.5965
6.35	10.96	16.46						32.567
7.63	5.35	2.92	-2.9225					-2.9225
20.11	29.63	-3.09						3.0925
41.24	29.08	18.18						-18.183
0.11	0.07	0.65						0.262333
-19.88	-10.55	-10.91						-42.4965
26.20	27.21	20.63						16.053
15.78	15.67	0.00						25.091
7.51	7.78	-0.59						0.594
-95	-2984	-1490	286	-2372	-3280	553	-966	413
2033	1385	848	951	940	237	35	80	-115

mT MDF GRMz (rps=2.5)	rps=2.5		from GRMz					
	(x10-10 Am ²)	RRM (not from Rz)	ARMrot	GRMz	Bg (uT)	BgZ (uT)	RRM (not from Rz)	ARMrot
	GRMz Tail SD+SD	0.5rps	0.5rps	0.5rps	0.5rps	0.5rps	2.5rps	2.5rps
61.89	2.49	-36.51	969.38	-20.78	-3.766	-2.143	-13.30	795.1
51.75	4.23	-26.67	901.76	-14.85	-2.957	-1.647	-10.90	739.6
84.77	1.12	-40.72	653.39	-9.38	-6.232	-1.436	-18.20	535.9
70.60	3.24	-51.51	1317.09	-12.44	-3.911	-0.944	-18.95	1080.2
72.48	8.22	-48.60	1369.53	-13.85	-3.549	-1.011	-14.87	1123.3
	820.10	-7754.46	275433.00	-1187.77	-2.815	-0.431	2980.49	286059.9
48.18	0.27	-0.39	39.69	-0.81	-0.970	-2.035	-0.48	28.2
38.58	8.23	-92.04	1629.49	-24.72	-5.648	-1.517	-43.57	1336.5
35.95	0.15	-0.04	591.42	0.08	-0.006	0.014	-0.16	485.1
56.00	3.55	-60.22	881.09	-10.77	-6.835	-1.222	-34.88	800.5
68.81	2.15	-36.99	373.05	-4.98	-9.914	-1.336	-24.96	357.7
59.22	518.81	7921	149646	-877	5.293	-0.586	2716.6	158719.5
		8016	180718	4709	4.436	2.605	3111.3	189457.0
82.45	774.65	-46755	48918	3416	-95.577	6.983	-28727.1	53865.2

from
GRMz

GRMz	Bg (uT)	BgZ (uT)	error in Bg values (uT)				error in BgZ values (uT)	ARMaxial	error in ' val
			rps=0.5		rps=2.5		(x10-10 Am2)		
2.5rps	2.5rps	2.5rps	rps=0.5	rps=0.5	rps=0.5	rps=2.5		1	
-5.348	-1.673	-0.673	0.360	0.151	0.708	0.314	2222	0.31	
-8.580	-1.474	-1.160	0.408	0.555	0.652	0.571	2185	0.27	
-4.028	-3.396	-0.752	0.388	0.094	0.604	0.209	1476	0.27	
-24.614	-1.754	-2.279	0.031	0.036	0.329	0.300	2856	0.15	
-37.978	-1.324	-3.381	0.060	0.033	0.267	0.732	2894	0.13	
-439.166	1.042	-0.154	0.253	0.098	0.140	0.287	225724	0.17	
-0.775	-1.711	-2.745	0.555	0.716	0.195	0.939	95	0.08	
41.828	-3.260	3.130	0.241	0.103	0.262	0.616	3821	0.11	
-10.140	-0.033	-2.090	0.015	0.004	0.007	0.031	970	0.00	
-6.128	-4.357	-0.765	0.149	0.200	0.357	0.443	1304	0.24	
-8.343	-6.977	-2.332	0.268	0.261	0.845	0.601	563	0.56	
1584.7	1.712	0.998	0.118	0.153	0.983	0.327	112910	1.30	
	1.642		2.614	0.093	0.749	0.000	118557	1.14	
-1253.7	-53.331	-2.328	0.629	5.100	2.381	1.438	49035	2.38	

estimated from variability

%GRMz	MDF (mT)	native	paper
	5 ARMz	sample	code
0.11	39.8	2H_10.4	df3c
0.19	39.6	2H-14.4	df3b
0.08	39.0	142.68	df5b
0.11	37.9	BL16.2	df6b
0.28	39.4	BO39	df1b
0.36	16.3	BO58	svd2
0.28	40.5	CCH16.9	cc1b
0.22	35.0	HO28b.4	df4b
0.02	36.5	HO29.3	df4c
0.27	38.4	ME13	mr1
0.38	34.9	ME17	mr5
0.46	14.6	CH5-Pyrr	py5
		8.1 CH7B-phyll	py7b
1.58	64	CH10-Greig	gr1

This sheet contains additional data measured at 2.5ps only

paper			RRM0		method-1		
sample	native sample codes		$\times 10^{-7}$ Am ² /Kg	$\times 10^{-7}$ Am ² /Kg	(mT)	$\times 10^{-7}$ Am ² /Kg	
codes	sample		RRM0	RRM0 SD	MDF RRM	RRM ₁₀₀	
	Chalk	CC9b 0m-a	-0.006	0.003	56	-0.015	
cc2	CC9B 0m -b		-0.006	0.004	58	-0.010	
	Chalk	CC9b 9.2m	-0.002	0.006	46	0.000	
	Chalk	CC9B 20.1m	-0.002	0.001	33	-0.002	
	Chalk	CC9b 93.1 m	-0.001	0.003	26	-0.005	
	Chalk	CCH1	-0.078	0.152	66	-0.114	
cc1	Chalk	CCH5	-0.043	0.034	72	-0.051	
	Chalk	CCH6	-0.023	0.024	66	-0.033	
	Chalk	CCH10	-0.059	0.030	56	-0.062	
cc1b	Chalk	CCH16.9	-0.011	0.013	55	-0.015	
	Chalk	CCH23.5A	-0.012	0.011	62	-0.021	
	Chalk	CCH29.3	-0.011	0.010	43	-0.013	
	Chalk	CCH44.4	-0.020	0.037	55	-0.030	
	Chalk	CCH46.4	-0.038	0.015	53	-0.035	
	Chalk	CCH47.9	-0.013	0.007	62	-0.025	
LUA	ME1	a36b (1) <38 {lots of hae	-56.51	11.49	32	-55.29	
LUC	ME2	a45a(1)<38	-169.51	6.64	35	-150.15	
LUC2	ME3	a45a 38-63 weak	1.71	4.63	65	-3.05	
KUC3	ME4	a45a 63-250 weak	-8.73	6.98	64	-0.09	
OR1	ME5	L35	-118.92	8.56	33	-98.75	
OR2	ME6	L36	-494.98	15.58	39	-573.53	
OR4	ME7	L58	-97.75	20.33	27	-100.87	
OR5	ME8	L59	-137.87	12.89	33	-236.06	
OR3	ME9	L42	-36.40	56.55	47	-195.31	
OR6	ME12	L69-70(1	-21.61	6.07	41	-19.11	
MR1	ME13	L23-24 (1)	-1679.32	52.67	40	-1642.49	
MR2	ME14	L20 (1)	14.54	25.00	35	-387.75	
MR3	ME15	L10-11 (1)	-153.54	27.54	58	-136.71	
MR4	ME16	709a/a (2)- E _{MPT}	-6029.50	300.00	21	-4630.00	
MR5	ME17	709c-3h-3 (2) E _{MPT}	-72249.27	1457.48	61	-77780.06	
MR6	ME18	709c/b (2) E _{MPT}	-1866.57	497.07	80	-1982.40	
	e.svalbard		114	-0.99	0.03	55	-1.30
	e.svalbard		116.45	0.40	0.01	63	-1.06
	e.svalbard		121.8	-0.55	0.05	60	-0.36
df5b	e.svalbard		142.68	-1.01	0.01	49	-1.02
	e.svalbard		145.36	-1.02	0.01	53	-1.07
	e.svalbard	154.35#		-0.84	0.02	38	-1.00
	e.svalbard		172.32	-3.91	0.07	48	-4.45
	e.svalbard		173.88	-1.93	0.05	46	-2.26
	e.svalbard		182.82	-0.35	0.01	53	-0.47
	e.svalbard		187.67	-0.07	0.02	58	-0.16

	e.svalbard	BL1.3	-0.69	0.00	58	-0.86
	e.svalbard	BL2.3	-0.69	0.01	40	-0.72
	e.svalbard	BL5.3	-1.08	0.10	43	-1.13
	e.svalbard	BL7.4	-0.30	0.02	49	-0.42
	e.svalbard	BL8.3	-0.67	0.02	39	-0.67
	e.svalbard	BL12.3	-0.83	0.04	34	-0.81
df6b	e.svalbard	BL16.2	-0.90	0.01	51	-0.99
	e.svalbard	BL17.2	-0.68	0.03	38	-0.63
df6	e.svalbard	BL18.4	-0.45	0.09	81	-0.68
	e.svalbard	BL20.3	-0.77	0.07	47	-1.14
	e.svalbard	BL21.4	-0.60	0.02	51	-0.68
	e.svalbard	BL27.4	-0.57	0.00	54	-0.59
	e.svalbard	BL24.4	-0.31	0.04	39	-0.29
	e.svalbard	BL25.4	-0.77	0.02	65	-0.93
	e.svalbard	BL26.4	-0.62	0.18	36	-0.97
	e.svalbard	bl3.4	-0.55	0.04	32	-0.56
	cent. Spitsbergen	DH4-111	-0.25	0.02	52	-0.43
	cent. Spitsbergen	DH4-148	-0.19	0.01	37	-0.21
	cent. Spitsbergen	DH4-152	-0.15	0.01	36	-0.29
	cent. Spitsbergen	DH4-18	-0.09	0.04	42	-0.21
	cent. Spitsbergen	DH4-35	-0.12	0.02	42	-0.14
df2	cent. Spitsbergen	DH4-42	-0.36	0.01	44	-0.45
	cent. Spitsbergen	DH4-53	-0.25	0.08	63	0.10
	cent. Spitsbergen	DH4-80	-0.36	0.01	59	-0.33
	cent. Spitsbergen	DH4-82	-0.28	0.04	34	-0.42
	cent. Spitsbergen	DH4-94	-0.23	0.01	55	-0.28
	cent. Spitsbergen	bo19	-0.27	0.09	34	-0.18
	cent. Spitsbergen	bo36	-1.18	0.02	44	-1.42
df1	cent. Spitsbergen	bo37	-1.10	0.04	47	-1.07
df1b	cent. Spitsbergen	bo39	-0.59	0.06	58	-0.74
	cent. Spitsbergen	bo41	-0.67	0.05	72	-0.72
	cent. Spitsbergen	bo45	-0.72	0.01	41	-0.83
	cent. Spitsbergen	bo47	-0.14	0.02	49	-0.12
	cent. Spitsbergen	bo48	-0.24	0.05	27	-0.24
	cent. Spitsbergen	bo54	-0.63	0.02	40	-0.76
	cent. Spitsbergen	bo56	-0.20	0.01	69	-0.21
	cent. Spitsbergen	bo57	-0.38	0.02	30	-0.72
	e.svalbard	WI3.3	-0.63	0.03	33	-1.08
	e.svalbard	WI4.2	-0.06	0.01	33	-0.07
	e.svalbard	WI6.4	-0.07	0.01	15	-0.08
	e.svalbard	WI12.2	-0.82	0.13	40	-0.95
	e.svalbard	WI14.3	0.00	0.00	12	-0.01
df5	e.svalbard	WI22.4	-0.63	0.01	62	-0.80
	e.svalbard	WI24.2	-0.41	0.04	50	-0.40
	Hopen	ho1.4	-0.57	0.02	55	-0.78
	Hopen	ho2.3	-0.73	0.00	53	-0.80
	Hopen	ho4.3	-0.56	0.03	44	-0.75
	Hopen	ho5.5	-2.34	0.05	69	-2.86
	Hopen	ho14.5	-0.56	0.10	72	-0.53
	Hopen	HO16.4	-0.47	0.01	67	-0.56

	Hopen	HO21.3	-0.06	0.01	61	-0.07
df4	Hopen	ho22.3	-1.43	0.04	50	-1.40
	Hopen	ho26.4	-0.55	0.05	66	-0.61
	Hopen	ho27.5	-1.94	0.06	41	-2.19
df4b	Hopen	ho28b.4	-1.84	0.00	40	-1.99
df4c	Hopen	ho29.3	-0.57	0.06	37	-0.71
	Hopen	ho35.4	-0.36	0.06	54	-0.51
	Hopen	ho31.2	-0.43	0.01	60	-0.56
	Hopen	2h-3.4	-0.87	0.10	36	-0.91
	Hopen	2h-12.4	-0.59	0.05	65	-0.75
	Hopen	2h-26.3	-0.60	0.00	46	-0.74
	Hopen	2H 1.5	-0.47	0.04	38	-0.29
	Hopen	2H 5.3	-0.69	0.03	32	-0.59
	Hopen	2H 6.4	-0.45	0.01	40	-0.50
df3c	Hopen	2H 10.4	-0.75	0.00	32	-0.62
df3b	Hopen	2H 14.4	-0.47	0.01	33	-0.40
	Hopen	2H 16.4	-0.59	0.08	34	-0.63
	Hopen	2H 17.4	-0.52	0.03	43	-0.49
	Hopen	2H 20.5	-0.76	0.17	40	-0.79
	Hopen	2H 21.4	-0.59	0.03	70	-0.53
	Hopen	2H 28.4	-0.71	0.02	33	-0.46
	Hopen	2H 39.4	-1.13	0.01	45	-0.87
	Hopen	2H 32.3	-0.95	0.15	46	-0.88
df3	Hopen	2H 34.4	-1.31	0.06	45	-1.15
Svalbard dolerite samples						
		WI18.3	372.68	3.26	62	298.249
svd2		bo58	127.76	8.66	58	75.570
svd1		bo32	-1802.98	28.75	40	-2041.017
		bo17	-1136.87	1.30	28	

RRM₁₀₀ = RRM determined from the two ARM_{ROT} determination (i.e. with I
RRM0= RRM value from both + and - spin measurements
RRM0 SD includes the measurement SD and the SD from the two RRM0 m
MDF RRM= using the method 1 (for the RRM demag, but contaminated wi
Bg (+-error)= in some cases rather pessimistic inference of the uncertainty
GRMz here is determined as the difference between the demagnetisation
GRMz-SD is the uncertainty in determining the demagnetisation tail

Ones not labelled in paper-sample-code column are those unlabelled shown in Fig. 13a,b,c

GRMz

	$x10^{-7}$	$x10^{-7}$		$x10^{-7}$	$x10^{-7}$	$x10^{-7}$	$x10^{-7}$	
	Am^2/Kg	Am^2/Kg	(uT)	(uT)	Am^2/Kg	Am^2/Kg	Am^2/Kg	Am^2/Kg
GRMZ	GRMZ (SD)	Bg	Bg (+-	ARM _{rot}	ARM _{trans}	ARM _z	ARM _{Rot}	SD
			error)					
-0.0319	0.0043	-0.61	0.05	0.99	1.420	3.285	0.018	
-0.0088	0.0019	-0.41	0.22	1.56	2.405	5.260	0.006	
-0.0401	0.0050	-0.25	0.92	0.67	1.003	2.085	0.009	
0.0128	0.0012	-0.55	0.28	0.29	0.374	0.803	0.000	
0.0041	0.0037	-0.20	1.14	0.19	0.255	0.590	0.008	
-0.2370	0.0523	-0.96	0.40	8.15	11.789	27.811	0.248	
-0.0218	0.0116	-0.79	0.06	5.46	7.977	19.454	0.047	
-0.0813	0.0140	-0.70	0.03	3.35	4.747	11.643	0.051	
-0.1435	0.0208	-0.80	0.08	7.33	11.410	25.509	0.064	
-0.0408	0.0068	-0.87	0.74	1.20	2.041	4.045	0.013	
0.0428	0.0114	-0.47	0.03	2.63	3.911	9.267	0.042	
-0.0276	0.0061	-0.59	0.25	1.86	2.994	5.892	0.012	
-0.1085	0.0115	-0.72	0.19	2.80	3.905	10.089	0.032	
-0.0608	0.0171	-0.94	0.07	4.03	6.348	15.048	0.117	
-0.0210	0.0108	-1.04	0.05	1.11	1.463	4.424	0.020	
-41.817	19.963	-4.36	0.89	1297	1059	1352	60	
-1.947	14.330	-3.00	0.11	5656	5018	7057	104	
5.245	0.968	1.14	3.07	150.71	156.2	272.3	1.607	
5.148	0.713	-14.77	11.82	59.09	74.7	130.0	5.643	
-64.693	15.143	-3.16	0.23	3763	3617	4695	107	
-39.305	69.701	-3.20	0.10	15466	14776	18001	214	
-58.043	61.078	-1.26	0.26	7752	7295	9268	144	
-104.639	7.071	-1.25	0.12	11015	10705	14742	183	
-258.270	102.723	-0.36	0.57	9999	8616	12885	398	
-16.393	6.220	-1.89	0.11	1141	1155	1701	50	
192.779	257.584	-4.23	0.13	39726	42864	64867	416	
62.042	5.645	0.66	0.30	2203	1706	2132	73	
89.964	14.683	-4.72	0.85	3251	3188	4531	117	
-1048.5	462.6	-3.90	0.02	154501	168829	215423	903	
-20570.4	8033.2	-6.74	0.14	1071163	1055145	1651177	25075	
-2823.3	483.2	-0.94	0.25	198584	192525	222607	4221	
-0.443	0.147	-1.64	0.03	60.40	102.58	249.83	0.096	
-1.683	0.526	0.67	0.34	60.11	85.25	185.63	0.096	
-0.415	0.175	-2.14	0.17	25.82	35.46	80.66	0.059	
-0.070	0.144	-3.29	0.03	30.71	40.75	84.58	0.069	
-0.280	0.152	-3.07	0.03	33.34	43.52	90.76	0.067	
0.044	0.023	-2.60	0.06	32.37	43.32	90.00	0.062	
0.649	0.154	-6.13	0.11	63.80	73.55	148.22	0.107	
0.051	0.103	-4.31	0.12	44.69	55.58	110.97	0.073	
-0.094	0.029	-1.76	0.05	19.95	27.68	59.97	0.053	
-0.159	0.015	-0.60	0.18	12.04	17.10	37.56	0.055	

-1.679	0.181	-1.39	0.00	49.22	63.52	129.44	0.075
-0.529	0.029	-1.36	0.02	51.09	66.53	135.84	0.080
-1.653	0.395	-1.72	0.14	62.45	74.48	140.88	0.067
-0.561	0.026	-1.35	0.06	22.33	29.02	58.50	0.045
-0.482	0.191	-1.69	0.05	39.42	52.57	107.38	0.067
-0.532	0.279	-1.46	0.06	56.56	71.11	143.80	0.088
-1.170	0.101	-1.76	0.02	51.03	65.50	134.93	0.089
-0.406	0.195	-1.56	0.06	43.45	56.25	113.88	0.041
-0.922	0.109	-0.81	0.16	55.85	72.58	150.29	0.046
-1.083	0.117	-1.36	0.13	56.43	75.04	158.77	0.089
-1.266	0.182	-1.22	0.04	48.97	65.63	138.28	0.068
-1.213	0.171	-1.10	0.00	51.71	68.48	143.09	0.076
-0.279	0.052	-1.16	0.15	26.59	35.45	72.22	0.044
-1.079	0.254	-1.39	0.04	55.39	73.13	150.54	0.078
-0.842	0.200	-0.97	0.28	63.86	85.59	175.95	0.097
-0.186	0.093	-1.16	0.07	47.88		135.00	0.273
-0.312	0.177	-0.84	0.04	29.83	40.15	89.20	0.029
-0.227	0.057	-0.71	0.01	26.86	36.51	78.96	0.051
-0.185	0.024	-0.56	0.02	27.27	37.35	79.40	0.041
-0.275	0.044	-0.72	0.29	11.96	15.93	34.12	0.036
-0.459	0.004	-0.45	0.06	25.98	34.90	74.19	0.030
-0.640	0.048	-1.05	0.00	34.33	46.41	96.15	0.050
-2.013	0.135	-0.67	0.18	37.29	47.05	88.02	0.039
-1.074	0.032	-1.09	0.03	33.04	44.39	92.15	0.031
-0.212	0.036	-0.89	0.11	30.95	41.75	88.51	0.034
-0.494	0.108	-1.11	0.06	20.78	27.97	61.20	0.024
-0.228	0.028	-0.91	0.28	29.33	38.50	82.52	0.694
-1.058	0.362	-1.62	0.02	72.86	89.10	173.53	1.128
-1.407	0.182	-1.93	0.06	57.14	73.47	147.32	0.428
-2.026	0.425	-1.17	0.11	50.71	65.77	130.67	0.329
-1.393	0.179	-1.33	0.10	50.27	66.16	138.50	0.754
-0.536	0.101	-1.27	0.00	56.29	71.69	145.14	0.247
1.353	0.039	-0.36	0.06	38.91	54.23	132.13	0.527
-0.375	0.319	-1.03	0.22	22.93	29.31	60.12	0.150
-0.670	0.171	-1.20	0.03	52.78	65.46	129.90	0.634
0.481	0.015	-0.85	0.06	23.45	32.17	69.37	0.491
-0.337	0.234	-0.92	0.05	41.75	54.87	114.99	0.718
-0.308	0.175	-1.10	0.05	56.94	74.21	153.29	0.115
-0.016	0.018	-0.85	0.07	6.85	9.18	19.98	0.017
-0.036	0.018	-0.84	0.08	7.92	10.14	21.61	0.019
-1.100	0.016	-1.21	0.18	67.25	79.95	149.58	0.125
-0.028	0.003						
-1.617	0.075	-1.05	0.01	59.77	75.10	153.42	0.061
-0.542	0.097	-0.85	0.07	48.43	65.14	137.55	0.042
-1.330	0.305	-1.13	0.03	51.03	70.52	152.46	0.737
-0.808	0.127	-1.39	0.00	52.56	70.18	148.21	1.073
-0.399	0.219	-0.91	0.05	61.63	84.68	179.05	0.318
-6.606	0.433	-0.78	0.01	300.14	466.08	1193.71	3.980
-0.829	0.237	-1.26	0.21	44.71	57.87	115.05	0.585
-1.195	0.705	-0.98	0.01	47.83	59.43	116.81	1.515

-0.103	0.007	-1.25	0.07	4.62	6.08	12.85	0.091
-1.098	0.335	-2.27	0.06	62.88	81.22	165.98	0.830
-0.525	0.073	-1.59	0.15	34.41	44.02	88.72	1.174
-1.284	0.251	-3.20	0.07	60.65	67.96	117.62	0.941
-0.818	0.014	-3.22	0.00	57.07	78.25	163.14	0.104
-0.637	0.255	-2.57	0.23	22.35	24.87	44.71	0.741
-0.477	0.489	-1.49	0.22	24.28	29.77	60.66	0.909
-0.836	0.094	-1.26	0.01	33.98	45.57	95.01	0.048
-0.693	0.021	-1.71	0.19	50.62	67.27	134.27	0.281
-0.884	0.362	-1.17	0.10	50.61	67.35	136.88	0.562
-0.649	0.199	-1.25	0.00	47.90	62.57	126.09	0.520
-0.320	0.186	-0.92	0.08	50.62		140.37	0.682
-0.412	0.091	-1.22	0.05	56.61		156.06	0.626
-0.129	0.106	-1.48	0.03	30.80		88.36	0.051
-0.272	0.006	-1.45	0.00	51.63		144.27	0.638
-0.294	0.116	-1.12	0.01	41.76		123.39	0.601
-0.211	0.051	-1.07	0.14	54.85		153.09	1.113
-0.805	0.132	-1.22	0.07	42.23		114.49	0.320
-0.527	0.022	-1.42	0.31	53.59		146.88	1.068
-1.358	0.052	-1.16	0.06	50.69		134.49	0.911
-0.002	0.114	-1.57	0.04	45.54		132.42	0.710
-0.632	0.043	-2.03	0.01	55.69		144.22	1.377
-0.209	0.113	-3.02	0.46	31.63		74.57	0.701
-0.289	0.008	-2.24	0.09	58.39		152.19	0.902
-20.581	61.174	1.53	0.01	24293.44	20535	24769.6	24.710
-16.826	2.880	1.16	0.08	10994.83	9750	8648.4	151.279
224.221	181.583	-7.34	0.11	24564.85	18021	24136.9	906.777
2.640	13.934	-8.37	0.00		11168		11.166

DC field field on) (not used in paper, since noisy)

measurements

with the GRMz)

γ from the difference between the two RRM0 measurements

tail, and the zero level of the RRM0 value- I.e average of the two RRM moments from the +rps and -rj

ARMz	ARMz	ARM _{ROT} / ARMz	sample type
MDF			
ARMz	d.ARM _{40mT}		
34.4	0.41	0.30	Chalk
40.6	0.51	0.30	Chalk
35.5	0.41	0.32	Chalk
27.8	0.28	0.36	Chalk
26.0	0.27	0.32	Chalk
43.2	0.56	0.29	Chalk
50.5	0.69	0.28	Chalk
47.9	0.65	0.29	Chalk
42.0	0.54	0.29	Chalk
40.5	0.51	0.30	Chalk
42.5	0.55	0.28	Chalk
38.3	0.46	0.32	Chalk
46.4	0.62	0.28	Chalk
46.0	0.63	0.27	Chalk
48.4	0.65	0.25	Chalk
30.6	0.39	0.96	extract
33.5	0.40	0.80	extract
37.1	0.47	0.55	extract
33.7	0.45	0.45	extract
29.9	0.38	0.80	extract
27.4	0.33	0.86	extract
28.0	0.36	0.84	extract
31.3	0.39	0.75	extract
28.0	0.40	0.78	extract
33.8	0.43	0.67	extract
38.4	0.47	0.61	extract
26.6	0.35	1.03	extract
30.8	0.38	0.72	extract
28.3	0.33	0.72	extract
34.9	0.43	0.65	extract
26.3	0.33	0.89	extract
33.2	0.39	0.24	De Geerdalen fm
32.1	0.37	0.32	De Geerdalen fm
38.3	0.47	0.32	De Geerdalen fm
39.0	0.48	0.36	De Geerdalen fm
38.8	0.48	0.37	De Geerdalen fm
38.4	0.47	0.36	De Geerdalen fm
40.6	0.51	0.43	De Geerdalen fm
38.3	0.47	0.40	De Geerdalen fm
37.6	0.46	0.33	De Geerdalen fm
37.5	0.46	0.32	De Geerdalen fm

38.9	0.48	0.38 De Geerdalen fm
38.7	0.48	0.38 De Geerdalen fm
36.2	0.44	0.44 De Geerdalen fm
38.3	0.47	0.38 De Geerdalen fm
37.8	0.47	0.37 De Geerdalen fm
37.9	0.47	0.39 De Geerdalen fm
37.9	0.47	0.38 De Geerdalen fm
37.9	0.47	0.38 De Geerdalen fm
38.8	0.48	0.37 De Geerdalen fm
38.7	0.48	0.36 De Geerdalen fm
38.6	0.48	0.35 De Geerdalen fm
38.8	0.48	0.36 De Geerdalen fm
38.5	0.48	0.37 De Geerdalen fm
38.8	0.48	0.37 De Geerdalen fm
38.2	0.47	0.36 De Geerdalen fm
39.0	0.48	0.35 De Geerdalen fm
40.1	0.50	0.33 De Geerdalen fm
40.1	0.50	0.34 De Geerdalen fm
39.9	0.50	0.34 De Geerdalen fm
41.2	0.52	0.35 De Geerdalen fm
40.7	0.51	0.35 De Geerdalen fm
40.0	0.50	0.36 De Geerdalen fm
45.4	0.57	0.42 De Geerdalen fm
39.3	0.49	0.36 De Geerdalen fm
39.5	0.49	0.35 De Geerdalen fm
38.7	0.48	0.34 De Geerdalen fm
39.4	0.49	0.36 De Geerdalen fm
39.3	0.49	0.42 De Geerdalen fm
39.6	0.49	0.39 De Geerdalen fm
39.4	0.49	0.39 De Geerdalen fm
40.0	0.50	0.36 De Geerdalen fm
40.0	0.50	0.39 De Geerdalen fm
28.7	0.34	0.29 De Geerdalen fm
39.2	0.49	0.38 De Geerdalen fm
39.5	0.49	0.41 De Geerdalen fm
38.8	0.48	0.34 De Geerdalen fm
37.7	0.47	0.36 De Geerdalen fm
37.3	0.46	0.37 De Geerdalen fm
36.9	0.45	0.34 De Geerdalen fm
37.1	0.45	0.37 De Geerdalen fm
39.9	0.50	0.45 De Geerdalen fm De Geerdalen fm
37.9	0.47	0.39 De Geerdalen fm
32.6	0.40	0.35 De Geerdalen fm
38.4	0.47	0.33 De Geerdalen fm
39.2	0.49	0.35 De Geerdalen fm
39.0	0.48	0.34 De Geerdalen fm
36.0	0.43	0.25 De Geerdalen fm
38.0	0.47	0.39 De Geerdalen fm
38.6	0.48	0.41 De Geerdalen fm

34.5	0.41	0.36 De Geerdalen fm
34.5	0.41	0.38 De Geerdalen fm
36.1	0.44	0.39 De Geerdalen fm
32.9	0.40	0.52 De Geerdalen fm
35.0	0.41	0.35 De Geerdalen fm
36.5	0.45	0.50 De Geerdalen fm
38.3	0.47	0.40 De Geerdalen fm
37.9	0.47	0.36 De Geerdalen fm
39.0	0.48	0.38 De Geerdalen fm
38.7	0.48	0.37 De Geerdalen fm
37.5	0.46	0.38 De Geerdalen fm
39.1	0.49	0.36 De Geerdalen fm
38.5	0.48	0.36 De Geerdalen fm
37.3	0.45	0.35 De Geerdalen fm
39.8	0.50	0.36 De Geerdalen fm
39.6	0.49	0.34 De Geerdalen fm
38.7	0.48	0.36 De Geerdalen fm
38.3	0.47	0.37 De Geerdalen fm
39.0	0.48	0.36 De Geerdalen fm
37.1	0.46	0.38 De Geerdalen fm
39.2	0.49	0.34 De Geerdalen fm
35.8	0.43	0.39 De Geerdalen fm
38.4	0.48	0.42 De Geerdalen fm
34.8	0.42	0.38 De Geerdalen fm
23.0	0.24	0.98 e.svalbard
16.3	0.19	1.27 central svalbard
41.8	0.53	1.02 central svalbard central svalbard

ps spins

RRM and ARM_{ROT} acquisition with AF field and rotation rate

Paper sample code	AF field	native code						RRM
				0.3	0.4	0.5	0.7	1
PY5	40 mT	3000	CH5	3070.4	2784.6	2838.6	1352.3	2513.7
PY5	60 mt	3000	CH5	6945.3	5626.3	5145.5	4793.8	3875.5
PY5	80 mT	3000	CH5	8065.1	7681.7	6364.2	4785.5	5071.3
DF5b	40	30	142.68	-8.0	-8.4	-8.7	-7.4	-5.5
DF5b	60	30		-22.4	-23.4	-23.0	-20.2	-16.1
	80							
	100							
PY5	40	30	CH5	2451.2	1715.3	2079.0	2153.0	1353.9
PY5	60	30		3962.6	4002.9	4601.7	3375.4	3296.8
PY5	80	30		6178.6	6250.4	6772.3	5952.4	5075.2
PY5	100	30		9205.1	8460.1	9177.0	8197.5	7218.1
GR1	40	30	CH10	-575.8	-618.6	-719.7	-795.9	-714.9
GR1	60	30		-5235.1	-5959.2	-6844.0	-7453.8	-6641.7
GR1	80	30		-19741.2	-21934.2	-23414.5	-23724.3	-21412.0
GR1	100	30		-37182.9	-44285.8	-45663.5	-41032.4	-36401.4
MR1	40	30	ME13	-16.0	-16.1	-18.3	-16.3	-14.6
MR1	60	30		-36.2	-36.4	-36.2	-34.2	-28.7
MR1	80	30		-50.6	-52.6	-52.7	-47.1	-42.7
MR1	100	30		-60.2	-59.6	-60.4	-54.3	-48.1
MR5	40	30	ME17	-8.6	-7.9	-8.2	-8.3	-6.6
MR5	60	30		-15.3	-15.8	-15.7	-15.4	-13.0
MR5	80	30		-24.9	-25.3	-24.6	-24.4	-21.7
MR5	100	30		-35.4	-37.0	-37.8	-34.5	-31.2
DF1b	40	30	BO39	-18.9725	-20.31	-19.7425	-15.82	-10.337
DF1b	60	30	BO39	-37.1445	-38.0985	-35.9835	-29.9455	-19.331

All in $\times 10^{-10} \text{ Am}^2$

1.5	2	2.5	3	0.6	0.8	1	1.4
384.0	1667.5	481.5	1030.1	137384.9	139572.1	141633.6	143399.1
3889.6	2953.7	3131.0	2145.6	142734.1	145567.6	147189.1	148313.8
4513.7	4200.7	3215.4	2967.2	146483.5	147737.5	148490.1	150158.0
-4.4	-4.2	-3.9	-3.6	369.6	392.5	413.7	393.6
-12.6	-10.9	-10.1	-10.1	541.1	554.6	539.5	520.8
1260.3	927.3	1268.8	662.8	122280.4	130751.4	133784.0	135249.1
3551.5	1727.0	2165.8	2298.7	134585.6	140302.8	141298.6	143897.3
4055.4	3976.8	4115.0	3319.6	140248.6	142901.3	145012.6	146176.6
5139.5	5713.3	3867.9	1116.2	152641.0	152882.2	149645.6	151222.6
-618.3	-553.9	-520.6	-690.7	7459.6	9088.2	9826.5	10329.0
-5532.0	-4972.2	-4746.6	-4612.6	15863.9	20423.7	22579.4	24194.4
-18132.7	-16514.5	-15859.2					
-31151.0	-28948.2	-28114.6	-28939.9	53789.5	54264.0	48918.4	49993.4
-11.3	-9.4	-9.6	-8.8	465.8	514.9	531.2	541.7
-23.6	-20.6	-18.7	-18.0	673.1	711.9	716.7	713.9
-35.6	-30.9	-29.3	-27.1	822.0	831.1	826.5	813.9
-40.5	-36.8	-33.8	-31.3	947.3	914.3	881.1	869.3
-5.3	-4.9	-4.6	-3.4	230.0	247.9	253.9	257.3
-10.2	-9.9	-8.9	-7.4	306.2	317.5	321.0	323.0
-18.2	-16.2	-15.7	-15.0	394.7	355.9	379.3	354.5
-27.7	-25.2	-24.6	-22.9	364.3	381.8	373.1	369.6
-7.913	-6.642	-4.716	-5.023	-143.7935	711.9905	775.0585	769.2535
-13.605	-10.2335	-7.7025	-7.341	-123.334	1061.423	1090.9045	1063.455

ARM Rot

2	3	4	5	6
143636.3	145109.4	145962.1	146819.6	147463.3
150500.0	152481.3	151264.5	152163.1	153409.9
150453.3	154012.9	153962.3	154534.3	155799.4
391.0	381.5	379.1	377.4	376.7
520.0	501.6			
136767.2	138745.8	138400.9	141032.3	141292.6
144355.9	146634.4	148635.4	148788.9	150216.7
148653.3	149897.2	151760.4	152060.4	153710.0
152799.6	156757.1	155820.5	158719.5	158087.7
10644.9	10913.1	11101.5	11247.1	11371.8
25325.2	26080.0	26622.6	27058.7	27552.8
51068.5	52465.4	53378.1	53865.2	54291.9
544.7	544.1	547.7	551.5	547.9
712.8	708.1	693.5	701.3	703.3
809.2	790.6	783.8	777.4	771.7
857.5	831.5	815.0	800.5	776.7
259.9	260.0	258.7	263.1	265.1
322.0	320.0	321.3	320.9	320.6
354.5	350.2	341.1	348.1	348.0
366.1	363.3	359.2	357.7	355.5
758.9325	764.717	754.075	729.1625	746.2755
1020.4485	1027.741	987.3925	932.4865	948.0235

with changes in hold times (cycles)

All data here in $\times 10^{-10} \text{ Am}^2$

All bar 1 at 100 mT AF

cycles	Native sample label	paper sample code	0.05	0.1	0.15	0.2
30	me13	MR1	-16.7	-33.6		-53.1
300	ME13	MR1	-25.1	-39.3	-50.8	-57.2
3000	ME13	MR1	-33.1	-46.5	-53.4	-58.9
30	ch5	PY5	3492.1	6575.6	6935.9	7856.7
300	CH5	PY5	4573.5	7176.9	9176.6	8984.1
300	CH5	PY5	4573.5	7176.9	9176.6	8984.1
3000	CH5	PY5	7307.8	7609.0	9819.7	8405.0
3000	ch5 (80mT) PY5					
30	ch10	GR1	-15524.7	-15830.7	-40572.8	-25361.7
300	CH10	GR1	-21642.7	-26102.7	-43381.3	-45799.7
300	CH10	GR1	-23131.9	-23051.8	-46976.3	-44893.1
3000	CH10	GR1	-27345.2	-45615.0	-40651.4	-53494.8
30 top	BO58	SVD2	-1204.6	-5213.7		-9380.1
300 top	B058	SVD2	-1950.9	-7153.4	-7933.7	-8565.7
300 top	BO58	SVD2	-1748.4	-7190.4	-7336.2	-8763.4
300 side	BO58	SVD2	8898.9	-16134.9	1126.2	-2497.9
300 side	BO58	SVD2	5300.5	-15299.0	456.8	-5137.3

RRM

0.3	0.4	0.5	0.75	1	1.5	2	2.5
-60.2	-59.6	-60.4		-48.1	-40.5	-36.8	-33.8
-62.5	-64.3	-61.3	-55.6	-50.9	-41.6	-37.8	-34.1
-63.0	-63.8	-61.6	-55.8	-50.7	-43.2	-37.9	-35.5
9205.1	8460.1	9177.0		7218.1	5139.5	5713.3	3867.9
10049.1	9311.5	8125.6	8561.0	6090.2	4676.1	4891.8	4238.8
9163.5	8072.6	7752.0	7338.0	6988.0	5374.4	4286.0	4689.5
8064.9	7681.5	6364.1	4785.4	5071.2	4513.6	4200.5	3215.3
-37182.9	-44285.8	-45663.5		-36401.4	-31151.0	-28948.2	-28114.6
-52477.8	-50383.3	-47742.9	-42327.0	-37929.6	-32984.1	-30968.5	-30381.9
-55691.9	-49974.8	-46525.8	-42424.3	-37871.1	-33014.0	-31012.4	-30411.9
-54932.7	-52739.8	-50592.4	-43909.2	-39579.7	-35181.5	-33546.1	-33235.4
-9771.8	-8292.3	-7358.9		-1686.7	1095.8	2429.4	3334.5
-8754.2	-8203.6	-6761.8	-3487.3	-1294.4	1823.2	2443.7	2752.9
-8828.2	-8121.7	-6484.0	-3802.0	-1420.2	1331.9	1503.9	
-2192.0	-6555.1	-2577.0	-436.7	2240.2	4060.5	4175.5	4971.3
-2634.3	-6093.3	-4378.6	-1408.1	827.1	3365.5	4293.4	4761.7

RRM 0.3-3 SD		RRM ₁₀₀						
		0.05	0.1	0.15	0.2	0.3	0.4	0.5
3		0.05	0.1	0.15	0.2	0.3	0.4	0.5
-31.3	0.5	-31.4	-35.5		-54.5	-59.5	-57.3	-65.6
-32.0	6.2	-44.3	-48.9	-49.6	-56.8	-65.7	-64.9	-63.3
-33.6	5.9	-36.2	-47.7	-54.5	-59.2	-65.5	-64.5	-64.1
1116.2	25.8	1767.6	6923.2	7400.0	8505.7	8446.6	8671.4	8538.0
3357.4	11.8	3107.7	7500.4	8044.5	10070.0	8595.0	9567.8	9177.6
	13.1	3107.7	7500.4	8044.5	10070.0			
3835.3	12.6	6761.4	7495.0	8607.2	10073.7	9456.7	8918.6	9371.6
2967.1								
-28939.9	43.7	-16557.0	-16095.1	-41970.0	-25186.2	-37640.3	-43798.4	-47490.8
-30423.2	44.9	-25455.8	-23410.4	-47449.3	-44965.2	-55838.7	-49979.4	-46631.8
-33564.1	51.7	-28842.6	-44688.6	-41478.2	-52649.0	-54316.5	-52985.1	-50943.3
3283.7	39.5	-4329.7	-6335.3		-10328.4	-10512.5	-8008.7	-8101.2
	763.2							
	757.1							
4455.0	674.5	-10063.7	1216.9	-6709.1	-6825.8	-5696.0	-3873.1	-3496.6
4082.3	28.0	-7782.5	-1367.9	-7562.4	-6411.9	-7828.9	-3596.5	-3923.3

						ARMrot 0.3-3 SD
0.75	1	1.5	2	2.5	3	
	-49.4		-39.0	-32.2	-12.8	2.0353
-54.3	-49.6	-40.4	-36.0	-37.1	-34.0	6.088158
-58.1	-51.3	-42.7	-20.6	-34.0	-32.8	6.251632
	6163.3	4980.3	4126.4	5249.6	3577.3	99.37173
6945.9	6805.3	5005.6	3959.4	4054.7	3753.1	101.5261
6968.3	5804.4	6304.8	4218.1	4511.6	4928.8	78.97192
	-36831.6	-31511.9	-29131.5	-28189.4	-27901.8	1922.965
-42577.2	-37958.2	-33081.9	-31120.1	-30480.9	-30380.7	1854.872
-43476.1	-39553.8	-35179.0	-33544.8	-33255.4	-33409.1	2393.536
	-1836.2		2233.4	2957.0	2859.9	1100.037
-311.9	1431.6	2915.1	4578.0	4582.4	5144.7	6606.112
-2536.7	1105.7	2359.7	3915.7	4093.4	5069.5	5619.254

ARMrot

	0.05	0.1	0.15	0.2	0.3	0.4	0.5	0.75	1
	899.1	975.9		968.3	947.3	914.3	881.1		857.5
	920.2	980.7	962.1	952.7	909.6	885.2	869.3	832.7	836.3
	998.1	989.9	977.7	963.7	913.1	891.7	871.6	842.3	839.6
142020.2	150754.6	151122.3	150963.9	152641.0	152882.2	149645.6			152799.6
142470.3	143985.2	146268.9	146610.5	143465.6	146053.3	146761.6	147084.1		148881.7
142470.3	143985.2	146268.9	146610.5						
147791.7	147787.2	148520.6	149903.6	149319.8	149685.5	148735.2	151630.3		150776.8
42533.6	57224.2	57437.7	59321.1	53789.5	54264.0	48918.4			51068.5
34179.6	60361.3	60488.8	44658.6	54298.3	59764.9	54028.3	54942.6		55940.9
65278.4	48075.6	63523.7	53235.4	56012.2	57228.0	58076.5	57989.5		58748.3
264174.6	284879.9		283821.6	282582.5	281519.5	275433.0			279306.8
267710.6	271803.7	261543.3	275903.2	262210.9	263415.0	262722.4	262043.0		262809.2
254000.8	276805.5	284521.4	267314.7	273718.3	270056.5	268581.9	267212.2		269058.1

1.5	2	2.5	3
831.5	815.0	800.5	776.7
808.7	792.0	783.9	776.2
814.3	777.9	788.3	780.0
156757.1	155820.5	158719.5	158087.7
150915.4	150589.8	153001.9	153116.4
153043.0	153515.1	155828.9	155089.5
52465.4	53378.1	53865.2	54291.9
56134.0	56468.6	56679.5	56994.4
58826.3	58982.3	59143.1	59199.2
281944.2	284333.9	286059.9	287588.5
264756.5	266441.0	268692.8	270628.5
268943.7	272091.0	274662.2	274989.4

Example rmg files for running the RRM procedures on the RAPID

Note the gauss values may need changing according to your labs field calibrations, and in Lancaster, R

File for RRM and ARM_{Rot} (100 uT DC) versus spin rates from 0.6 to 6 rps (i.e. 0.3- 3 real rps)

```

Level,Bias Field (G),Spin Speed (rps),Hold Time (s),Mz (emu),Std. Dev. Z,Mz/Vol,Moment Susceptibility (
UAFX1, 1190 , 0 , 0 , 0 , 0 , 0 , 0 , 0 , 0 , 0 , 0 , 0
UAFX2, 1190 , 0 , 0 , 0 , 0 , 0 , 0 , 0 , 0 , 0 , 0 , 0
UAFZ1, 1496 , 0 , 0 , 0 , 0 , 0 , 0 , 0 , 0 , 0 , 0 , 0
NRM, 0 , 0 , 0 , 0 , 1.00000000000001E-09 , 1.00000000000001E-09 , 1.00000000000001E-09 , 0 , 1.000
RRM, 1082 , 0 , -0.6 , 0 , 1.00000000000001E-09 , 1.00000000000001E-09 , 1.00000000000001E-09 , 0 ,
RRM, 1082 , 0 , 0.6 , 0 , 1.00000000000001E-09 , 1.00000000000001E-09 , 1.00000000000001E-09 , 0 ,
RRM, 1082 , 0 , -0.8 , 0 , 1.00000000000001E-09 , 1.00000000000001E-09 , 1.00000000000001E-09 , 0 ,
RRM, 1082 , 0 , 0.8 , 0 , 1.00000000000001E-09 , 1.00000000000001E-09 , 1.00000000000001E-09 , 0 ,
RRM, 1082 , 0 , -1 , 0 , 1.00000000000001E-09 , 1.00000000000001E-09 , 1.00000000000001E-09 , 0 ,
RRM, 1082 , 0 , 1 , 0 , 1.00000000000001E-09 , 1.00000000000001E-09 , 1.00000000000001E-09 , 0 ,
RRM, 1082 , 0 , -1.5 , 0 , 1.00000000000001E-09 , 1.00000000000001E-09 , 1.00000000000001E-09 , 0 ,
RRM, 1082 , 0 , 1.5 , 0 , 1.00000000000001E-09 , 1.00000000000001E-09 , 1.00000000000001E-09 , 0 ,
RRM, 1082 , 0 , -2 , 0 , 1.00000000000001E-09 , 1.00000000000001E-09 , 1.00000000000001E-09 , 0 ,
RRM, 1082 , 0 , 2 , 0 , 1.00000000000001E-09 , 1.00000000000001E-09 , 1.00000000000001E-09 , 0 ,
RRM, 1082 , 0 , -3 , 0 , 1.00000000000001E-09 , 1.00000000000001E-09 , 1.00000000000001E-09 , 0 ,
RRM, 1082 , 0 , 3 , 0 , 1.00000000000001E-09 , 1.00000000000001E-09 , 1.00000000000001E-09 , 0 ,
RRM, 1082 , 0 , -4 , 0 , 1.00000000000001E-09 , 1.00000000000001E-09 , 1.00000000000001E-09 , 0 ,
RRM, 1082 , 0 , 4 , 0 , 1.00000000000001E-09 , 1.00000000000001E-09 , 1.00000000000001E-09 , 0 ,
RRM, 1082 , 0 , -5 , 0 , 1.00000000000001E-09 , 1.00000000000001E-09 , 1.00000000000001E-09 , 0 ,
RRM, 1082 , 0 , 5 , 0 , 1.00000000000001E-09 , 1.00000000000001E-09 , 1.00000000000001E-09 , 0 ,
RRM, 1082 , 0 , -6 , 0 , 1.00000000000001E-09 , 1.00000000000001E-09 , 1.00000000000001E-09 , 0 ,
RRM, 1082 , 0 , 6 , 0 , 1.00000000000001E-09 , 1.00000000000001E-09 , 1.00000000000001E-09 , 0 ,
UAFZ1, 1496 , 0 , 0 , 0 , 0 , 0 , 0 , 0 , 0 , 0 , 0 , 0
NRM, 0 , 0 , 0 , 0 , 1.00000000000001E-09 , 1.00000000000001E-09 , 1.00000000000001E-09 , 0 , 1.000
RRM, 1082 , 1.1 , -0.6 , 0 , 1.00000000000001E-09 , 1.00000000000001E-09 , 1.00000000000001E-09 , 0 ,
RRM, 1082 , 1.1 , 0.6 , 0 , 1.00000000000001E-09 , 1.00000000000001E-09 , 1.00000000000001E-09 , 0 ,
RRM, 1082 , 1.1 , -0.8 , 0 , 1.00000000000001E-09 , 1.00000000000001E-09 , 1.00000000000001E-09 , 0 ,
RRM, 1082 , 1.1 , 0.8 , 0 , 1.00000000000001E-09 , 1.00000000000001E-09 , 1.00000000000001E-09 , 0 ,
RRM, 1082 , 1.1 , -1 , 0 , 1.00000000000001E-09 , 1.00000000000001E-09 , 1.00000000000001E-09 , 0 ,
RRM, 1082 , 1.1 , 1 , 0 , 1.00000000000001E-09 , 1.00000000000001E-09 , 1.00000000000001E-09 , 0 ,
RRM, 1082 , 1.1 , -1.5 , 0 , 1.00000000000001E-09 , 1.00000000000001E-09 , 1.00000000000001E-09 , 0 ,
RRM, 1082 , 1.1 , 1.5 , 0 , 1.00000000000001E-09 , 1.00000000000001E-09 , 1.00000000000001E-09 , 0 ,
RRM, 1082 , 1.1 , -2 , 0 , 1.00000000000001E-09 , 1.00000000000001E-09 , 1.00000000000001E-09 , 0 ,
RRM, 1082 , 1.1 , 2 , 0 , 1.00000000000001E-09 , 1.00000000000001E-09 , 1.00000000000001E-09 , 0 ,
RRM, 1082 , 1.1 , -3 , 0 , 1.00000000000001E-09 , 1.00000000000001E-09 , 1.00000000000001E-09 , 0 ,
RRM, 1082 , 1.1 , 3 , 0 , 1.00000000000001E-09 , 1.00000000000001E-09 , 1.00000000000001E-09 , 0 ,
RRM, 1082 , 1.1 , -4 , 0 , 1.00000000000001E-09 , 1.00000000000001E-09 , 1.00000000000001E-09 , 0 ,
RRM, 1082 , 1.1 , 4 , 0 , 1.00000000000001E-09 , 1.00000000000001E-09 , 1.00000000000001E-09 , 0 ,
RRM, 1082 , 1.1 , -5 , 0 , 1.00000000000001E-09 , 1.00000000000001E-09 , 1.00000000000001E-09 , 0 ,
RRM, 1082 , 1.1 , 5 , 0 , 1.00000000000001E-09 , 1.00000000000001E-09 , 1.00000000000001E-09 , 0 ,
RRM, 1082 , 1.1 , -6 , 0 , 1.00000000000001E-09 , 1.00000000000001E-09 , 1.00000000000001E-09 , 0 ,
RRM, 1082 , 1.1 , 6 , 0 , 1.00000000000001E-09 , 1.00000000000001E-09 , 1.00000000000001E-09 , 0 ,
UAFZ1, 1496 , 0 , 0 , 0 , 0 , 0 , 0 , 0 , 0 , 0 , 0 , 0
NRM, 0 , 0 , 0 , 0 , 1.00000000000001E-09 , 1.00000000000001E-09 , 1.00000000000001E-09 , 0 , 1.000

```

Nb. Your RAPID software may require a small tweak to perform UAF demag step without a measureme

ent as here (hence the NRM step to do the zero-measurement)

File for RRM and RRM demagnetisation (10mT steps) at 1 and 5 (0.

Level,Bias Field (G),Spin Speed (rps),Hold Time (s),Mz (emu),Std. Dev.
 UAFX1, 1190 , 0 , 0 , 0 , 0 , 0 , 0 , 0 , 0 , 0 , 0 , 0 , 0
 UAFX2, 1190 , 0 , 0 , 0 , 0 , 0 , 0 , 0 , 0 , 0 , 0 , 0 , 0
 UAFZ1, 1496 , 0 , 0 , 0 , 0 , 0 , 0 , 0 , 0 , 0 , 0 , 0 , 0
 NRM, 0 , 0 , 0 , 0 , 1.000000000000001E-09 , 1.000000000000001E-09 ,
 RRM, 1082 , 0 , -1 , 0 , 1.000000000000001E-09 , 1.000000000000001E-
 RRM, 1082 , 0 , 1 , 0 , 1.000000000000001E-09 , 1.000000000000001E-0
 AFz, 107 , 0 , 0 , 0 , 1.000000000000001E-09 , 1.000000000000001E-09 ,
 AFz, 224 , 0 , 0 , 0 , 1.000000000000001E-09 , 1.000000000000001E-09 ,
 AFz, 295 , 0 , 0 , 0 , 1.000000000000001E-09 , 1.000000000000001E-09 ,
 AFz, 396 , 0 , 0 , 0 , 1.000000000000001E-09 , 1.000000000000001E-09 ,
 AFz, 491 , 0 , 0 , 0 , 1.000000000000001E-09 , 1.000000000000001E-09 ,
 AFz, 602 , 0 , 0 , 0 , 1.000000000000001E-09 , 1.000000000000001E-09 ,
 AFz, 702 , 0 , 0 , 0 , 1.000000000000001E-09 , 1.000000000000001E-09 ,
 AFz, 802 , 0 , 0 , 0 , 1.000000000000001E-09 , 1.000000000000001E-09 ,
 AFz, 899 , 0 , 0 , 0 , 1.000000000000001E-09 , 1.000000000000001E-09 ,
 AFz, 998 , 0 , 0 , 0 , 1.000000000000001E-09 , 1.000000000000001E-09 ,
 AFz, 1097 , 0 , 0 , 0 , 1.000000000000001E-09 , 1.000000000000001E-09
 AFz, 1201 , 0 , 0 , 0 , 1.000000000000001E-09 , 1.000000000000001E-09
 AFz, 1299 , 0 , 0 , 0 , 1.000000000000001E-09 , 1.000000000000001E-09
 AFz, 1399 , 0 , 0 , 0 , 1.000000000000001E-09 , 1.000000000000001E-09
 AFz, 1496 , 0 , 0 , 0 , 1.000000000000001E-09 , 1.000000000000001E-09
 RRM, 1082 , 0 , -1 , 0 , 1.000000000000001E-09 , 1.000000000000001E-
 AFz, 107 , 0 , 0 , 0 , 1.000000000000001E-09 , 1.000000000000001E-09 ,
 AFz, 224 , 0 , 0 , 0 , 1.000000000000001E-09 , 1.000000000000001E-09 ,
 AFz, 295 , 0 , 0 , 0 , 1.000000000000001E-09 , 1.000000000000001E-09 ,
 AFz, 396 , 0 , 0 , 0 , 1.000000000000001E-09 , 1.000000000000001E-09 ,
 AFz, 491 , 0 , 0 , 0 , 1.000000000000001E-09 , 1.000000000000001E-09 ,
 AFz, 602 , 0 , 0 , 0 , 1.000000000000001E-09 , 1.000000000000001E-09 ,
 AFz, 702 , 0 , 0 , 0 , 1.000000000000001E-09 , 1.000000000000001E-09 ,
 AFz, 802 , 0 , 0 , 0 , 1.000000000000001E-09 , 1.000000000000001E-09 ,
 AFz, 899 , 0 , 0 , 0 , 1.000000000000001E-09 , 1.000000000000001E-09 ,
 AFz, 998 , 0 , 0 , 0 , 1.000000000000001E-09 , 1.000000000000001E-09 ,
 AFz, 1097 , 0 , 0 , 0 , 1.000000000000001E-09 , 1.000000000000001E-09
 AFz, 1201 , 0 , 0 , 0 , 1.000000000000001E-09 , 1.000000000000001E-09
 AFz, 1299 , 0 , 0 , 0 , 1.000000000000001E-09 , 1.000000000000001E-09
 AFz, 1399 , 0 , 0 , 0 , 1.000000000000001E-09 , 1.000000000000001E-09
 AFz, 1496 , 0 , 0 , 0 , 1.000000000000001E-09 , 1.000000000000001E-09
 UAFZ1, 1496 , 0 , 0 , 0 , 0 , 0 , 0 , 0 , 0 , 0 , 0 , 0 , 0
 NRM, 0 , 0 , 0 , 0 , 1.000000000000001E-09 , 1.000000000000001E-09 ,
 RRM, 1082 , 0 , -5 , 0 , 1.000000000000001E-09 , 1.000000000000001E-
 RRM, 1082 , 0 , 5 , 0 , 1.000000000000001E-09 , 1.000000000000001E-0
 AFz, 107 , 0 , 0 , 0 , 1.000000000000001E-09 , 1.000000000000001E-09 ,
 AFz, 224 , 0 , 0 , 0 , 1.000000000000001E-09 , 1.000000000000001E-09 ,
 AFz, 295 , 0 , 0 , 0 , 1.000000000000001E-09 , 1.000000000000001E-09 ,
 AFz, 396 , 0 , 0 , 0 , 1.000000000000001E-09 , 1.000000000000001E-09 ,

AFz, 491 , 0 ,0 , 0 , 1.000000000000001E-09 , 1.000000000000001E-09 ,
AFz, 602 , 0 ,0 , 0 , 1.000000000000001E-09 , 1.000000000000001E-09 ,
AFz, 702 , 0 ,0 , 0 , 1.000000000000001E-09 , 1.000000000000001E-09 ,
AFz, 802 , 0 ,0 , 0 , 1.000000000000001E-09 , 1.000000000000001E-09 ,
AFz, 899 , 0 ,0 , 0 , 1.000000000000001E-09 , 1.000000000000001E-09 ,
AFz, 998 , 0 ,0 , 0 , 1.000000000000001E-09 , 1.000000000000001E-09 ,
AFz, 1097 , 0 ,0 , 0 , 1.000000000000001E-09 , 1.000000000000001E-09 ,
AFz, 1201 , 0 ,0 , 0 , 1.000000000000001E-09 , 1.000000000000001E-09 ,
AFz, 1299 , 0 ,0 , 0 , 1.000000000000001E-09 , 1.000000000000001E-09 ,
AFz, 1399 , 0 ,0 , 0 , 1.000000000000001E-09 , 1.000000000000001E-09 ,
AFz, 1496 , 0 ,0 , 0 , 1.000000000000001E-09 , 1.000000000000001E-09 ,
RRM, 1082 , 0 , -5 , 0 , 1.000000000000001E-09 , 1.000000000000001E-09 ,
AFz, 107 , 0 ,0 , 0 , 1.000000000000001E-09 , 1.000000000000001E-09 ,
AFz, 224 , 0 ,0 , 0 , 1.000000000000001E-09 , 1.000000000000001E-09 ,
AFz, 295 , 0 ,0 , 0 , 1.000000000000001E-09 , 1.000000000000001E-09 ,
AFz, 396 , 0 ,0 , 0 , 1.000000000000001E-09 , 1.000000000000001E-09 ,
AFz, 491 , 0 ,0 , 0 , 1.000000000000001E-09 , 1.000000000000001E-09 ,
AFz, 602 , 0 ,0 , 0 , 1.000000000000001E-09 , 1.000000000000001E-09 ,
AFz, 702 , 0 ,0 , 0 , 1.000000000000001E-09 , 1.000000000000001E-09 ,
AFz, 802 , 0 ,0 , 0 , 1.000000000000001E-09 , 1.000000000000001E-09 ,
AFz, 899 , 0 ,0 , 0 , 1.000000000000001E-09 , 1.000000000000001E-09 ,
AFz, 998 , 0 ,0 , 0 , 1.000000000000001E-09 , 1.000000000000001E-09 ,
AFz, 1097 , 0 ,0 , 0 , 1.000000000000001E-09 , 1.000000000000001E-09 ,
AFz, 1201 , 0 ,0 , 0 , 1.000000000000001E-09 , 1.000000000000001E-09 ,
AFz, 1299 , 0 ,0 , 0 , 1.000000000000001E-09 , 1.000000000000001E-09 ,
AFz, 1399 , 0 ,0 , 0 , 1.000000000000001E-09 , 1.000000000000001E-09 ,
AFz, 1496 , 0 ,0 , 0 , 1.000000000000001E-09 , 1.000000000000001E-09

᠑ , 1.000000000000001E-09
᠑ , 1.000000000000001E-09
᠑ , 1.000000000000001E-09
᠑ , 1.000000000000001E-09
᠑ , 1.000000000000001E-09
᠑ , 1.000000000000001E-09
᠑9 , 1.000000000000001E-09
᠑9 , 1.000000000000001E-09
᠑9 , 1.000000000000001E-09
᠑9 , 1.000000000000001E-09
᠑9 , 1.000000000000001E-09
᠑9 , 1.000000000000001E-09
E-09 , 1.000000000000001E-09
᠑ , 1.000000000000001E-09
᠑ , 1.000000000000001E-09
᠑ , 1.000000000000001E-09
᠑ , 1.000000000000001E-09
᠑ , 1.000000000000001E-09
᠑ , 1.000000000000001E-09
᠑ , 1.000000000000001E-09
᠑ , 1.000000000000001E-09
᠑ , 1.000000000000001E-09
᠑ , 1.000000000000001E-09
᠑9 , 1.000000000000001E-09
᠑9 , 1.000000000000001E-09
᠑9 , 1.000000000000001E-09
᠑9 , 1.000000000000001E-09
᠑9 , 1.000000000000001E-09

00 mT AF) demagnetisation (at 10 mT steps, C) at 1 and 5 rps (0.5 and 2.5 real rps) with repeats for bet

ε (s),Mz (emu),Std. Dev. Z,Mz/Vol,Moment Susceptibility (emu/Oe),Mx (emu),Std. Dev. X,My (emu),Std.

00000000000001E-09 , 1.00000000000001E-09 , 0 , 1.00000000000001E-09 , 1.00000000000001E-09 , 1
 9) , 1.00000000000001E-09 , 1.00000000000001E-09 , 0 , 1.00000000000001E-09 , 1.00000000000001E-0
 9 , 1.00000000000001E-09 , 1.00000000000001E-09 , 0 , 1.00000000000001E-09 , 1.00000000000001E-09
 9) , 1.00000000000001E-09 , 1.00000000000001E-09 , 0 , 1.00000000000001E-09 , 1.00000000000001E-0
 9 , 1.00000000000001E-09 , 1.00000000000001E-09 , 0 , 1.00000000000001E-09 , 1.00000000000001E-09
 9) , 1.00000000000001E-09 , 1.00000000000001E-09 , 0 , 1.00000000000001E-09 , 1.00000000000001E-0
 9 , 1.00000000000001E-09 , 1.00000000000001E-09 , 0 , 1.00000000000001E-09 , 1.00000000000001E-09
 9) , 1.00000000000001E-09 , 1.00000000000001E-09 , 0 , 1.00000000000001E-09 , 1.00000000000001E-0
 9 , 1.00000000000001E-09 , 1.00000000000001E-09 , 0 , 1.00000000000001E-09 , 1.00000000000001E-09

00000000000001E-09 , 1.00000000000001E-09 , 0 , 1.00000000000001E-09 , 1.00000000000001E-09 , 1
 9) , 1.00000000000001E-09 , 1.00000000000001E-09 , 0 , 1.00000000000001E-09 , 1.00000000000001E-
 9 , 1.00000000000001E-09 , 1.00000000000001E-09 , 0 , 1.00000000000001E-09 , 1.00000000000001E-
 9) , 1.00000000000001E-09 , 1.00000000000001E-09 , 0 , 1.00000000000001E-09 , 1.00000000000001E-
 9 , 1.00000000000001E-09 , 1.00000000000001E-09 , 0 , 1.00000000000001E-09 , 1.00000000000001E-
 9) , 1.00000000000001E-09 , 1.00000000000001E-09 , 0 , 1.00000000000001E-09 , 1.00000000000001E-

00000000000001E-09 , 1.00000000000001E-09 , 0 , 1.00000000000001E-09 , 1.00000000000001E-09 , 1
 9) , 1.00000000000001E-09 , 1.00000000000001E-09 , 0 , 1.00000000000001E-09 , 1.00000000000001E-0
 .00000000000001E-09 , 1.00000000000001E-09 , 0 , 1.00000000000001E-09 , 1.00000000000001E-09 , :
 .00000000000001E-09 , 1.00000000000001E-09 , 0 , 1.00000000000001E-09 , 1.00000000000001E-09 , :
 .00000000000001E-09 , 1.00000000000001E-09 , 0 , 1.00000000000001E-09 , 1.00000000000001E-09 , :
 .00000000000001E-09 , 1.00000000000001E-09 , 0 , 1.00000000000001E-09 , 1.00000000000001E-09 , :
 .00000000000001E-09 , 1.00000000000001E-09 , 0 , 1.00000000000001E-09 , 1.00000000000001E-09 , :
 .00000000000001E-09 , 1.00000000000001E-09 , 0 , 1.00000000000001E-09 , 1.00000000000001E-09 , :
 .00000000000001E-09 , 1.00000000000001E-09 , 0 , 1.00000000000001E-09 , 1.00000000000001E-09 , :
 .00000000000001E-09 , 1.00000000000001E-09 , 0 , 1.00000000000001E-09 , 1.00000000000001E-09 , :
 .00000000000001E-09 , 1.00000000000001E-09 , 0 , 1.00000000000001E-09 , 1.00000000000001E-09 , :

00000000000001E-09 , 1.00000000000001E-09 , 0 , 1.00000000000001E-09 , 1.00000000000001E-09 , 1

Header RRM values

Dev. Y

1.00000000000001E-09 , 1.00000000000001E-09
 09 , 1.00000000000001E-09 , 1.00000000000001E-09
 9 , 1.00000000000001E-09 , 1.00000000000001E-09
 09 , 1.00000000000001E-09 , 1.00000000000001E-09
 9 , 1.00000000000001E-09 , 1.00000000000001E-09
 09 , 1.00000000000001E-09 , 1.00000000000001E-09
 9 , 1.00000000000001E-09 , 1.00000000000001E-09
 09 , 1.00000000000001E-09 , 1.00000000000001E-09
 9 , 1.00000000000001E-09 , 1.00000000000001E-09

1.00000000000001E-09 , 1.00000000000001E-09
 09 , 1.00000000000001E-09 , 1.00000000000001E-09
 09 , 1.00000000000001E-09 , 1.00000000000001E-09
 09 , 1.00000000000001E-09 , 1.00000000000001E-09
 09 , 1.00000000000001E-09 , 1.00000000000001E-09

1.00000000000001E-09 , 1.00000000000001E-09
 09 , 1.00000000000001E-09 , 1.00000000000001E-09
 1.00000000000001E-09 , 1.00000000000001E-09
 1.00000000000001E-09 , 1.00000000000001E-09
 1.00000000000001E-09 , 1.00000000000001E-09
 1.00000000000001E-09 , 1.00000000000001E-09
 1.00000000000001E-09 , 1.00000000000001E-09
 1.00000000000001E-09 , 1.00000000000001E-09
 1.00000000000001E-09 , 1.00000000000001E-09

1.00000000000001E-09 , 1.00000000000001E-09

File for RRM

Level,Bias F

UAFX1, 119
 UAFX2, 119
 UAFZ1, 149
 NRM, 0 , 0 ,
 RRM, 436 ,
 RRM, 436 ,
 RRM, 436 ,
 RRM, 436 ,
 RRM, 436 ,
 RRM, 436 ,
 RRM, 1082
 RRM, 1082
 RRM, 1082
 RRM, 1082
 RRM, 1082
 RRM, 1082
 RRM, 1082
 RRM, 1082
 RRM, 1082
 RRM, 1082
 UAFZ1, 149
 NRM, 0 , 0 ,
 RRM, 1082
 RRM, 1082
 UAFZ1, 396
 NRM, 0 , 0 ,
 RRM, 1082
 RRM, 1082
 UAFZ1, 396
 NRM, 0 , 0 ,
 ARM, 998 ,
 UAFZ1, 396
 NRM, 0 , 0 ,
 UAFX1, 119
 UAFX2, 119
 UAFZ1, 149
 NRM, 0 , 0 ,
 UAFZ1, 149
 NRM, 0 , 0 ,

VI, ARM_{rot}, and ARM_z using optimum settings (cycles hold= 312 on RAPID)- using sub-set to get key bi-

Field (G),Spin Speed (rps),Hold Time (s),Mz (emu),Std. Dev. Z,Mz/Vol,Moment Susceptibility (emu/Oe),M

0,0,0,0,0,0,0,0,0,0,0,0,0,0,0,0,0,0

0,0,0,0,0,0,0,0,0,0,0,0,0,0,0,0,0,0

6,0,0,0,0,0,0,0,0,0,0,0,0,0,0,0,0,0

,0,0,1.000000000000001E-09,1.000000000000001E-09,1.000000000000001E-09,0,1.000000000000

0,-0.524,0,1.000000000000001E-09,1.000000000000001E-09,1.000000000000001E-09,0,1.000000

0,0.524,0,1.000000000000001E-09,1.000000000000001E-09,1.000000000000001E-09,0,1.000000

0,-0.524,0,1.000000000000001E-09,1.000000000000001E-09,1.000000000000001E-09,0,1.000000

0,0.524,0,1.000000000000001E-09,1.000000000000001E-09,1.000000000000001E-09,0,1.000000

0,-0.524,0,1.000000000000001E-09,1.000000000000001E-09,1.000000000000001E-09,0,1.000000

0,0.524,0,1.000000000000001E-09,1.000000000000001E-09,1.000000000000001E-09,0,1.000000

,0,-0.524,0,1.000000000000001E-09,1.000000000000001E-09,1.000000000000001E-09,0,1.000000

0,0.524,0,1.000000000000001E-09,1.000000000000001E-09,1.000000000000001E-09,0,1.000000

,0,-0.524,0,1.000000000000001E-09,1.000000000000001E-09,1.000000000000001E-09,0,1.000000

0,0.524,0,1.000000000000001E-09,1.000000000000001E-09,1.000000000000001E-09,0,1.000000

,0,-0.524,0,1.000000000000001E-09,1.000000000000001E-09,1.000000000000001E-09,0,1.000000

0,0.524,0,1.000000000000001E-09,1.000000000000001E-09,1.000000000000001E-09,0,1.000000

,0,-5,0,1.000000000000001E-09,1.000000000000001E-09,1.000000000000001E-09,0,1.00000000

0,5,0,1.000000000000001E-09,1.000000000000001E-09,1.000000000000001E-09,0,1.00000000

,0,-5,0,1.000000000000001E-09,1.000000000000001E-09,1.000000000000001E-09,0,1.00000000

0,5,0,1.000000000000001E-09,1.000000000000001E-09,1.000000000000001E-09,0,1.00000000

,0,-5,0,1.000000000000001E-09,1.000000000000001E-09,1.000000000000001E-09,0,1.00000000

0,5,0,1.000000000000001E-09,1.000000000000001E-09,1.000000000000001E-09,0,1.00000000

6,0,0,0,0,0,0,0,0,0,0,0,0,0,0,0,0,0

,0,0,1.000000000000001E-09,1.000000000000001E-09,1.000000000000001E-09,0,1.000000000000

,1.1,-0.524,0,1.000000000000001E-09,1.000000000000001E-09,1.000000000000001E-09,0,1.0000

,1.1,-0.524,0,1.000000000000001E-09,1.000000000000001E-09,1.000000000000001E-09,0,1.0000

5,0,0,0,0,0,0,0,0,0,0,0,0,0,0,0,0,0

,0,0,1.000000000000001E-09,1.000000000000001E-09,1.000000000000001E-09,0,1.000000000000

,1.1,-5,0,1.000000000000001E-09,1.000000000000001E-09,1.000000000000001E-09,0,1.000000

,1.1,-5,0,1.000000000000001E-09,1.000000000000001E-09,1.000000000000001E-09,0,1.000000

5,0,0,0,0,0,0,0,0,0,0,0,0,0,0,0,0,0

,0,0,1.000000000000001E-09,1.000000000000001E-09,1.000000000000001E-09,0,1.000000000000

1.1,0,0,1.000000000000001E-09,1.000000000000001E-09,1.000000000000001E-09,0,1.00000000

5,0,0,0,0,0,0,0,0,0,0,0,0,0,0,0,0,0

,0,0,1.000000000000001E-09,1.000000000000001E-09,1.000000000000001E-09,0,1.000000000000

0,0,0,0,0,0,0,0,0,0,0,0,0,0,0,0,0,0

0,0,1.000000000000001E-09,1.000000000000001E-09,1.000000000000001E-09,0,1.000000000000

6,0,0,0,0,0,0,0,0,0,0,0,0,0,0,0,0,0

,0,0,1.000000000000001E-09,1.000000000000001E-09,1.000000000000001E-09,0,1.000000000000

6,0,0,0,0,0,0,0,0,0,0,0,0,0,0,0,0,0

,0,0,1.000000000000001E-09,1.000000000000001E-09,1.000000000000001E-09,0,1.000000000000

